

On Interacting Particles in 1D and 2D

Joshua DM Hellier



Doctor of Philosophy
The University of Edinburgh
February 2019

Abstract

Diffusion processes are pretty ubiquitous across the natural world, so it is important to try to understand them. A system in which diffusion is being driven by concentration differences between boundary reservoirs is a simple example of a nonequilibrium statistical mechanics system. In this thesis, we study a model that has been hanging around the literature in one form or another for a long time: the Sticky Particle Model, or SPM. This is a very basic one-parameter exclusion model, in which particles move away from adjacent particles with a different rate to their normal free movement. We use a variety of techniques to analyse induced flow in this model, including a simple analytic mean-field theory, Monte Carlo calculations, and direct numerical analysis of the transition rate operator that specifies small versions of the system. During these investigations, we have discovered what we argue is a nonequilibrium phase transition between flow regimes at high and low values of our stickiness parameter; much of our work has gone into attempts to understand the nature of this apparent transition.

Declaration

I declare that this thesis was composed by myself, that the work contained herein is my own except where explicitly stated otherwise in the text, and that this work has not been submitted for any other degree or professional qualification except as specified.

Parts of this work have been published in [21].

(Joshua DM Hellier, February 2019)

Acknowledgements

I would like to thank Giulio de Magistris, Alexander Slowman, Tom Ives, James Gratrex, Chay Patterson, Pattanasak Teeratchanan, Yarden Brody, Andreas Hermann, Miguel Martinez-Canales, Eugene Gregoryanz, Martin Evans, Richard Blythe, Bartek Waclaw and anyone else I may have missed out for their helpful input during this research project. I also thank the ECDF team here at Edinburgh who have provided a great deal of material support and technical expertise to this project via their ongoing upkeep of the computing infrastructure I made use of (primarily `Eddie3`); similarly, I must give many thanks to EPSRC for providing the funding which has made this project possible in the first place.

In addition, I am very grateful to my parents and friends for their support during what has been a rather difficult time. Most of all I would like to thank my supervisor, Graeme Ackland, who has contributed a lot of his time and effort to produce the work you see before you today.

Contents

Abstract	i
Declaration	iii
Acknowledgements	v
Contents	vii
List of Figures	xi
List of Tables	xv
1 Introduction	1
1.1 Derivation and Motivation of the Sticky Particle Model	1
1.1.1 The Motion of Small Atoms in Crystal Lattices	1
1.1.2 Reduction to 1D, Simplifications, and Model Definition	2
1.1.3 The Sticky Particle Model	5
1.2 Properties of the Sticky Particle Model	7
1.2.1 Homogeneity	7
1.2.2 Symmetry	7
1.2.3 Locality.....	7
1.2.4 Detailed Balance	8

1.3	Relationship to Existing Models	9
1.3.1	The Ising Model	9
1.3.2	SEP/ASEP/TASEP	10
1.3.3	The KLS Model	10
1.4	Research Outline.....	11
2	Analytical Results about the SPM	13
2.1	Solving Problems in Nonequilibrium Statistical Mechanics.....	13
2.1.1	Equilibrium Statistical Mechanics.....	14
2.1.2	Nonequilibrium Statistical Mechanics.....	15
2.1.3	Where does the SPM stand?	17
2.2	Similarities between the SPM and Established Models in 1D.....	18
2.2.1	Relationship with the Ising Model	18
2.2.2	Correlation Functions	19
2.2.3	Calculation of the Partition Function of the SPM on a Closed Ring.....	20
2.3	Using the Mean-Field Approximation on the SPM.....	24
2.3.1	Lattice MFT Derivation	24
2.3.2	Continuum Limit MFT Derivation.....	26
2.3.3	Negative Diffusion Coefficients.....	28
2.3.4	Continuum Limit MFT Solutions	30
2.3.5	Implications of Continuum MFT Breakdown.....	37
2.4	The SPM in Higher Dimensions.....	37
2.4.1	Symmetry + Locality + Detailed Balance = Unique 1- Parameter SPM	38

2.4.2	MFT of the n -Dimensional SPM	43
2.5	Conclusions About the SPM MFT	47
3	Transition Rate Matrix Analysis	51
3.1	The Transition Rate Operator for the SPM.....	51
3.1.1	A Small Worked Example: Closed System	53
3.2	Forming the TRM for Systems with Dirichlet Boundary Conditions	55
3.2.1	Dirichlet Boundary Conditions.....	55
3.2.2	Another Worked Example: Open System	56
3.2.3	Construction of the TRM in Sparse Format	59
3.3	The Eigenspectrum of the TRM	61
3.3.1	The Computation of the TRM Eigenspectrum.....	61
3.3.2	The Structure of the TRM Eigenspectrum.....	61
3.3.3	Current and Density in the Steady State.....	72
3.4	Time-Dependent Properties of Small SPM Systems.....	78
3.4.1	The Relaxation Time for the SPM.....	79
3.4.2	Time-Evolution of States.....	81
3.5	Conclusions	81
4	Monte-Carlo Simulations of the SPM	85
4.1	Numerical Simulations of Continuous-Time Markov Processes	85
4.1.1	Purpose of Monte-Carlo Methods	85
4.1.2	Evenly-Spaced Timesteps	86
4.1.3	The N-Fold Way, or Gillespie Algorithm	88

4.2	Implementation of Monte Carlo Methods.....	90
4.2.1	Our Implementation of a Metropolis-Hastings Algorithm with Evenly-Space Timesteps	90
4.2.2	KMCLib.....	90
4.2.3	Managing KMCLib Calculations in Parallel	94
4.3	1D Calculation Results.....	95
4.3.1	Flow Patterns	96
4.3.2	Scans Through λ with Constant Boundary Densities.....	100
4.3.3	Varying λ and Boundary Density Difference Together	114
4.3.4	Varying the Boundary Densities with Constant λ	117
4.3.5	Diffusion Coefficient	117
4.4	2D Calculation Results.....	122
4.4.1	Aspect Ratio Considerations	122
4.4.2	Varying λ with Constant Boundary Conditions.....	123
4.5	Conclusions	128
5	Conclusions	129
A	Code Locations	131
A.1	1d Ising Correlation Functions	131
A.2	n -Dimensional Continuum-Limit MFT	131

List of Figures

(1.1)	An impression of the kind of background potential experienced by a particle moving against a periodic lattice in 1D.	3
(1.2)	The kind of interaction potential that might exist between two nearby particles.	4
(1.3)	The sum of the background and interaction potentials.	4
(1.4)	The transition rates in the Sticky Particle Model.	6
(2.1)	Plots of the equal-time particle density correlation function on a ring.	19
(2.2)	The free energy density of the SPM on a closed ring, as a function of density and λ	22
(2.3)	The chemical potential of the SPM on a closed ring, as a function of density and λ	23
(2.4)	Some plots of the variation of the MFT diffusion coefficient with density, for some selected λ	27
(2.5)	A contour plot of the variation of the MFT diffusion coefficient with density and stickiness.	28
(2.6)	The variation in the current at fixed λ with respect to the boundary densities.	32
(2.7)	The variation of flow rate with respect to λ in the MFT, with fixed boundary densities.	33
(2.8)	The dependence of the critical value of λ required for backward diffusion on the boundary conditions.	34
(2.9)	The variation of the system-wide average density with respect to λ in the MFT, with fixed boundary densities.	35
(2.10)	The possible transitions which may occur in a symmetric local 2-dimensional hopping model.	39

(2.11)	Figure demonstrating that a local system obeying detailed balance and symmetry cannot have interesting local configuration-dependent dynamics.	40
(2.12)	Figure demonstrating that particle motion out of a hyperplane with m adjacent particles away from an empty space occurs with rate λ^m	42
(2.13)	Figure demonstrating that particle motion out of a hyperplane with m adjacent particles away from an empty space occurs with rate λ^m	42
(2.14)	The variation of the density of maximal/minimal flow with λ	46
(2.15)	2D SPM MFT current flow due to boundaries, for a selection of λ	48
(2.16)	2D SPM MFT current flow as a function of λ , with fixed boundaries..	49
(3.1)	The variation of configuration probabilities with λ for a small open system.	58
(3.2)	The variation of the eigenspectrum of the TRM with λ for a small open system.	59
(3.3)	The TRM eigenspectrum for a system with $L = 5$, $b = 1000$	64
(3.4)	The lower part of the TRM eigenspectrum for a system with $L = \{5, 10\}$, $b = \{100, 1000\}$	66
(3.5)	A graph of the scaling of the number of slow modes with system size.	68
(3.6)	The upper TRM eigenspectrum for a system with $L = \{5, 10\}$, $b = \{100, 1000\}$	70
(3.7)	The “full” TRM eigenspectrum for a system with $L = 8$, $b = 1000$	71
(3.8)	The variation of the density profile with λ for a system of size $L = 12$ and boundaries ($\rho_0 = 0.6$, $\rho_L = 0.4$).	73
(3.9)	The variation of the current (measured flowing from high density boundary to low) with λ for a system of size $L = 10$ and boundaries ($\rho_0 = 0.6$, $\rho_L = 0.4$).	75
(3.10)	The variation of the diffusion coefficient of a system of size $L = 10$ with respect to λ and ρ	77
(3.11)	The variation of the order parameter χ for a system of size $L = 10$ with respect to λ and ρ	79
(3.12)	The dependence of the relaxation time on λ for three sets of boundary conditions.	80
(3.13)	The time-evolution of uniform distributions to equilibrium.	82

(4.1)	Illustration of the method for choosing successor states in the n-fold way.	90
(4.2)	The flow pattern of sticky particles in 1D.	98
(4.3)	The flow pattern of repulsive particles in 1D.	101
(4.4)	The current flowing through systems as we vary λ with constant boundaries, 1D	103
(4.5)	As Fig. 4.4 but over a much wider range of λ -values..	104
(4.6)	Comparison of the variation of the mean current with λ for different system sizes.	105
(4.7)	Calculations of the dependence of current upon λ , repeated with different system sizes.	107
(4.8)	Higher moments of the current, in 1D	108
(4.9)	The variation of the variance of the density of the SPM system with λ for different boundary conditions, in 1D.	110
(4.10)	The variation of the overall mean density of the SPM system with λ for different boundary conditions, in 1D.	111
(4.11)	Time-averaged density profiles for systems with fixed boundary densities, over a range of λ	113
(4.12)	The mean block size and its standard error..	115
(4.13)	Results obtained by fixing the average of the boundary densities and varying their difference and λ	116
(4.14)	Mean currents observed when varying the boundary densities, fixing λ , for different λ	118
(4.15)	Mean densities observed when varying the boundary densities, fixing λ , for different λ	119
(4.16)	The variation of the KMC-calculated diffusion coefficient with ρ and λ	120
(4.17)	The variation of the KMC-calculated diffusion coefficient with ρ and λ ; alternate plots..	121
(4.18)	The variation of the current in a 2D SPM system with λ , for a variety of different system sizes and aspect ratios.	124
(4.19)	The variation of the overall density in a 2D SPM system with λ	126

List of Tables

Chapter 1

Introduction

During the course of my PhD investigations, I have primarily focussed on the phenomenology of a model of interacting stochastic particle motion through lattices, called the **Sticky Particle Model** (SPM). In this chapter we motivate and define this model, and then explore some of its more basic properties and association with existing models in the literature.

1.1 Derivation and Motivation of the Sticky Particle Model

1.1.1 The Motion of Small Atoms in Crystal Lattices

Consider a material composed of a regular crystalline lattice of a single type of atom. Most pure metals are like this in at least part of their solid phase. For example, under standard conditions Iron is such a material, and will typically try and assume a body-centred cubic (bcc) structure [1], whilst Titanium tends to form a hexagonal close-packed (hcp) structure [44].

It is often possible for impurities to enter such a crystalline material. In many situations, these invading atoms are smaller than those of which the bulk material is composed [12, 54]. Such small impurity atoms can reside in the interstitial spaces between the crystal atoms, and they will sometimes move between adjacent interstitial sites. This motion is stochastic in nature, as it depends upon the

impurity possessing sufficient momentum to squeeze between the lattice atoms and travel to the next site, or those atoms perhaps moving apart a little to allow easier passage; both of these processes are dominated by thermal effects at finite temperature, and the end result is that the impurity atom will tend to hop from one interstitial site into an adjacent one essentially at random, with some rate $\tau_0^{-1}\text{s}^{-1}$. Such rates can be determined either by actual experiments (e.g. tracer diffusion [42, 61]) or by theoretical means (e.g. molecular dynamics [28, 62]).

A single such impurity atom will obviously perform some kind of random walk though the system, and those kinds of mathematics have been treated previously. In this work, we really want to consider what effects these particles have upon each other as they hop around, via their interactions; thus, we think it best that we perform simplifications in order to strip out any nonessential details, so that we can focus on effects caused by interaction. Therefore we won't be calculating any transition rates for real systems.

1.1.2 Reduction to 1D, Simplifications, and Model Definition

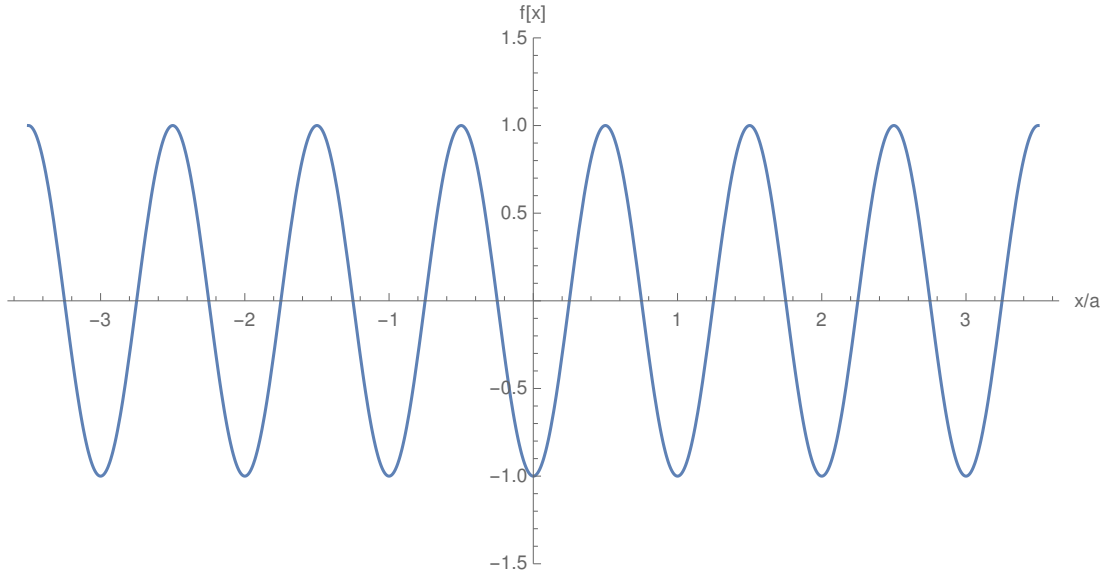
A crystal in physical reality is typically 3-dimensional¹. However, a lot of the time these 3D crystals can be quite anisotropic. For example, in an hcp crystal lattice, the complementary lattice of octahedral interstitial sites form a simple hexagonal structure, consisting of stacked planes of hexagonal lattices [38]. Thus, it is not too difficult to envision a situation in which the hopping rate is much faster between planes than within them, or vice-versa. In the first situation, if there were sufficient discrepancy between the interplanar and intraplanar hopping rates we would essentially have a series of decoupled 1 or 2-dimensional systems.

We should also remember that it is often much easier to use analytical techniques in one dimension than in higher dimensions, and that the performance of numerical techniques often scales unfavourably with dimension. Therefore, we have chosen to concentrate on the 1D case for the time being, and will then return to the issue of higher dimensions in Sec. 2.4.

A particle hopping back and forth in 1D would experience a periodic potential energy arising from the background lattice, perhaps like the one displayed in Fig. 1.1. In terms of its potential energy due to other particles like itself, it might experience a hard core repulsion with an intermediate-range attraction/repulsion,

¹or possibly 2-dimensional, but those are odd cases [2]

Figure 1.1 A simple example of the kind of background potential experienced by a particle moving against a periodic lattice in 1D. Here the potential is represented by $f(x)$, where a is the lattice spacing.



such as the Lennard-Jones potential [4] shown in Fig. 1.2. Thus, the total potential energy landscape from the particle’s perspective might look something like Fig. 1.3. There are a few things to note here in terms of such a particle moving with the influence of fluctuating forces:

1. Particles should be expected to spend the vast majority of their time in the minima of the externally-induced potential. This essentially creates a lattice of distinct slots within which a particle is highly likely to be at any given time. Thus it is reasonable to speak of particles occupying these “slots” and occasionally transitioning between them.
2. There is a large potential barrier opposing attempts by particles to get close together. Therefore, it is unlikely that multiple particles would be able to squeeze into the same slot, and so the assumption that each slot can contain at most one particle is a reasonable one.
3. If the transition rates between adjacent slots behave in an Arrhenius-like manner [3, 37], i.e.

$$\tau_0^{-1} \propto e^{\frac{\Delta U}{k_B T}}, \quad (1.1)$$

with $k_B T$ being the characteristic thermal energy, then the rate of transition is dominated by ΔU , the size of the “energy barrier” which our particle

Figure 1.2 The kind of interaction potential that might exist between two nearby particles, $g(x)$. Here we have used a Lennard-Jones potential [4], with parameters chosen so that the interaction scale is comparable to the lattice spacing a . The particle generating this potential is located at the origin.

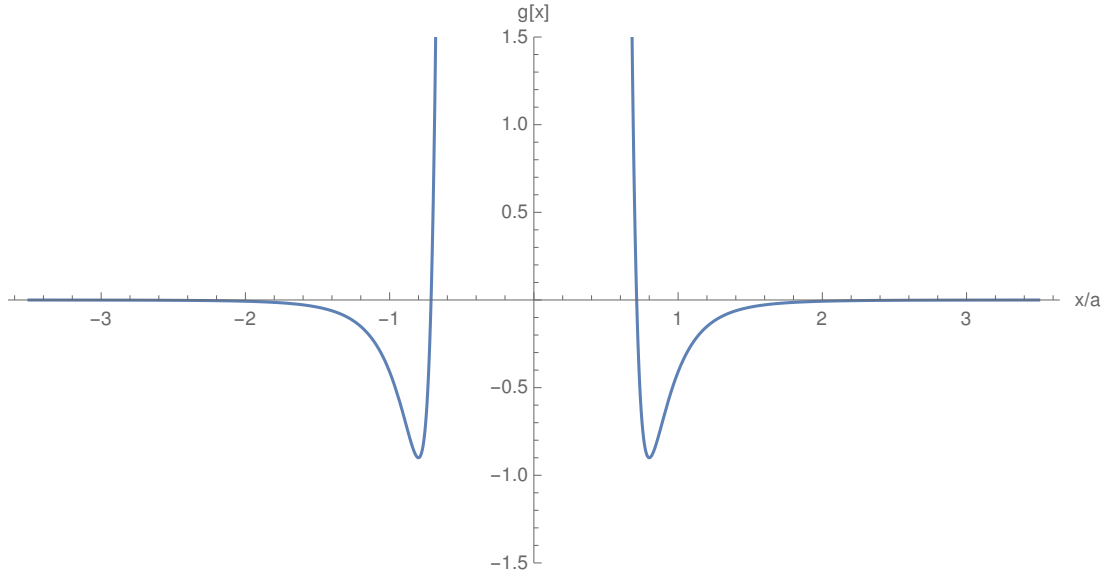
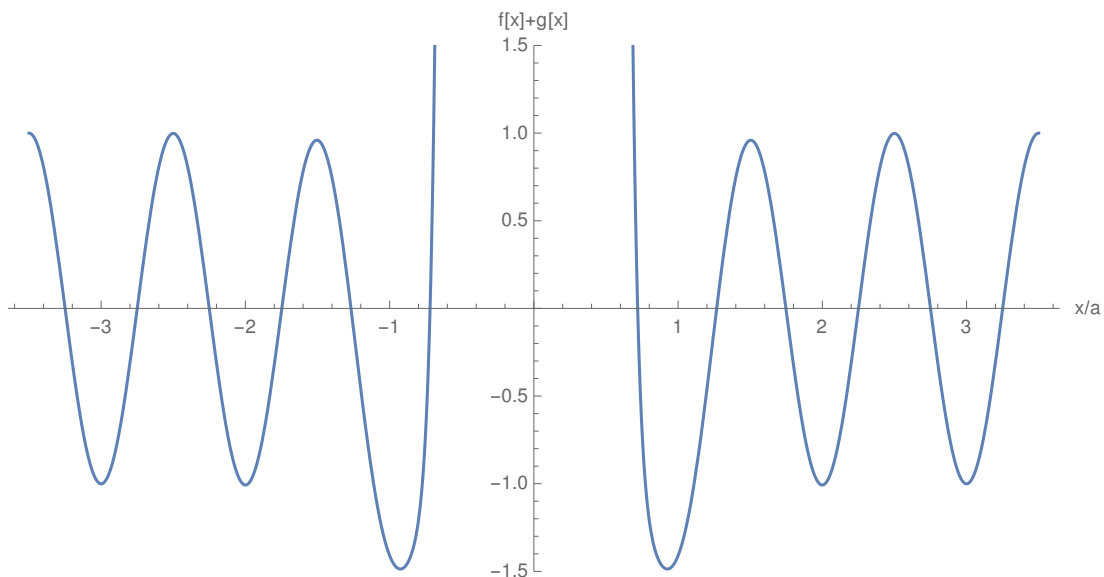


Figure 1.3 The sum of the background and interaction potentials, the interaction being generated by a particle at the origin. Notice that the minimum closest to the origin has been greatly deepened, disproportionately to the lowering of the peak between it and the next-nearest neighbour.



must cross in order to escape from its slot and move to the next one. If we have a relatively short-ranged intermediate component to the interparticle potential, we can see from Fig. 1.3 that the dominant effect is on the depth of the potential well in which an adjacent particle sits, followed by the height of the barrier the adjacent particle must cross in order to move away. As these quantities are altered by different amounts on account of their different distances away from the particle at the origin, we might expect that **the dominant affect of the presence of the original particle is to alter the rate at which an adjacent particle will move away from it**. Of course, the depths and barrier heights of other slots further away would also in general be affected, but if the interparticle interaction potential decays very rapidly over the length of a lattice spacing these next-neighbour effects will be very small compared to the nearest-neighbour effect.

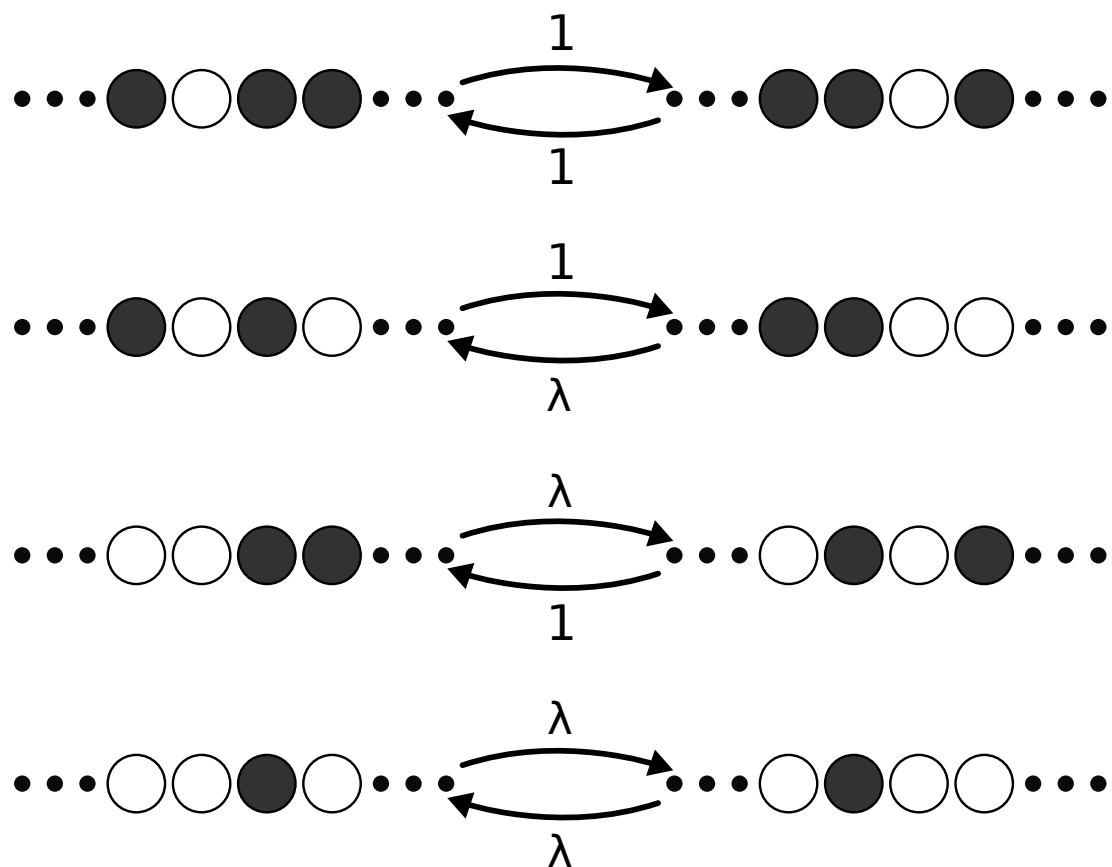
4. The particle and background lattice is also assumed to thermalize after the hop. There should be no time-correlated "double hop" events or "two particle" simultaneous hops.

1.1.3 The Sticky Particle Model

Combining these ideas, we would do well to investigate models that exhibit exclusion (i.e. no more than one particle per slot), and in which particles hop away from adjacent particles differently to when they are on their own. Therefore, we propose a continuous-time Markov process with transition rates as indicated in Fig. 1.4, which we call the Sticky Particle Model (SPM). A simple verbal description of the model is as follows: particles move randomly into empty adjacent sites with rate τ_0^{-1} , unless they are already adjacent to a particle, in which case they jump away from that adjacent particle with rate $\lambda\tau_0^{-1}$. We have factored out τ_0 because it is the ratio of these two rates, λ , that is most important to the phenomenology of this model; rescaling τ_0 is equivalent to rescaling time, which is in some sense trivial, whereas varying λ should yield models with different behaviours.

Of course, this model is the epitome of a "toy model", and with good reason. The complexity of the analysis of physical models generally scales quite unfavourably with the number of parameters; this model has the benefit of having only one meaningful parameter, which should make it much easier for us to explore model behaviour when we use numerical methods.

Figure 1.4 The transition rates in the Sticky Particle Model. Here white circles are particles, and black circles are vacancies. Dots indicate connections to the rest of the system; the configuration of the particles and vacancies there is irrelevant to the transition here due to the interaction's short range. Arrows with accompanying quantities indicate possible transitions and their rates, here divided by the base rate τ_0^{-1} .



1.2 Properties of the Sticky Particle Model

Here we list a few properties that the SPM possesses. Note that these properties, although simple, are often not shared by other models, and in some sense they mark the SPM out by its having all of them.

1.2.1 Homogeneity

The same transition rules apply to any particle in an SPM system regardless of spatial location. We will break true homogeneity later on when we consider adding boundary conditions, but even then we still have homogeneous dynamics in the bulk.

1.2.2 Symmetry

One of the more simple aspects of the SPM is its obvious mirror symmetry: that is, the system dynamics are unchanged by a mirror symmetry transformation. This differentiates it from ASEP-like models [16]; we will say more about those in Sec. 1.3.2. We will refer to this property as *symmetry*.

1.2.3 Locality

The SPM has the property that a particle's transition rates are determined solely by its immediate environment, in the sense that it can only hop into a space which is empty, and its rate of doing so then only depends upon what is behind it. By taking account of what is behind it, the model is differentiated from SEP; by not accounting for anything further afield, it is not the same as a more transparently energy-based model might be (although we will see that this model does have an energy interpretation in Sec. 1.2.4). We will henceforth refer to this property as *locality*.

1.2.4 Detailed Balance

The SPM possesses the properties of homogeneity, symmetry and locality essentially by design. Indeed, it is the only exclusion model in 1D which possesses all of these properties ²: a particle can only move into an empty space (exclusion), and so then by locality we need only concern ourselves with its immediate neighbours to determine the hopping rate; then there are only two options, depending upon what is in the slot the particle is hopping away from, meaning that there are two possible rates, one for each occupation of that neighbour. But by symmetry and homogeneity, these two rates must apply at every site, and equally in both directions; thus, adopting all these properties gives us no choice but the SPM.

These rates also imply an additional property. Recall the definition of **detailed balance** [14]: that there exists a probability distribution P over configurations $\xi \in \Xi$ such that $\forall \xi_1, \xi_2 \in \Xi$,

$$P(\xi_1) \cdot \sigma(\xi_1 \rightarrow \xi_2) = P(\xi_2) \cdot \sigma(\xi_2 \rightarrow \xi_1). \quad (1.2)$$

Here, Ξ is the space of all possible configurations for the SPM, and $\sigma(a \rightarrow b)$ is the transition rate from state a to state b . In our case a transition means performing one of the operations shown in Fig. 1.4. There, we list all of the motions that can occur, with all possible local environments: the central two slots must contain exactly one particle and one vacancy in order for a transition to be possible, and there are two ways to do this; then there are the two remaining slots at the sides, which can have any of the two occupations each, so there are 8 meaningfully different transitions in total.

Consider a probability distribution of the form $P(\xi) \propto \lambda^{-n}$, where n is the total number of particle-particle adjacencies in the system. In the outer two diagrams of Fig. 1.4, the forward and backward transition rates are identical, as are the number of particle-particle adjacencies; thus Eq. (1.2) is trivially satisfied using the proposed distribution P . In the middle two diagrams, we see that reducing the number of adjacencies by one occurs with rate λ , whilst increasing that number by one happens with rate 1. Thus, in the language of Eq. (1.2),

$$\lambda P_0 \cdot 1 = P_0 \cdot \lambda, \quad (1.3)$$

²SEP also obeys these properties, but it is of course simply the $\lambda = 1$ case of the SPM.

where P_0 is a normalisation constant for the probability distribution. We see therefore that the SPM transition rates satisfy the detailed balance condition with distribution P ; we can interpret the detailed-balance energy as being located in the “bond” between two adjacent particles. In hindsight, that the model obeys detailed balance is perhaps not so surprising; however, it is not immediately obvious from the transition rates alone.

An alert reader will have noticed that we still haven’t discussed the domain on which the process takes place very much. In our detailed balance proof we used only the SPM bulk rates, so that this result only applies to SPM systems defined on an infinite domain or on a finite ring. If one introduces boundaries, and defines additional rates to define their behaviour, one will typically end up breaking detailed balance.

1.3 Relationship to Existing Models

Of course, the SPM is not exactly “new”: it is very similar to several models already discussed in the literature. Here we will discuss the more prominent of these, with emphasis on why the SPM is different or how we are going to analyse it differently to them.

1.3.1 The Ising Model

The SPM is equivalent to a constrained version of the classical Ising model [24, 36, 53] in 1D; we can map SPM occupations $\rho_i \in 0, 1$ on to Ising spins $\sigma_i \in -1, 1$ via the transformation

$$\sigma_i = 2\rho_i - 1. \tag{1.4}$$

The constraint is that the magnetisation is locally conserved, i.e. we can only swap the spins of adjacent sites during the dynamics. If we are careful with our definitions of the SPM transition rates, the SPM is a equivalent to a method for numerically simulating the Ising model known as Kawasaki dynamics, which has been in the literature for a long time [15, 18, 27]. Kawasaki dynamics was originally intended as a stochastic Markov process designed to replicate the Ising model in equilibrium, albeit with a constraint on the magnetisation, which makes more sense when the dynamics are interpreted as a model of a two-species alloy.

We have more to say about the correspondence with the Ising model in Sec. 2.2.1.

In theory, one can calculate equilibrium properties of the SPM by using this equivalence to the constrained Ising model; in order to do this, one may attempt to implement the constraint by varying the applied magnetic field in such a way that the system ends up with the correct magnetisation, and then working out desired quantities from there using the Ising partition function [5]. However, we found that this results in extremely convoluted algebra, and it is actually easier to build a new partition for the SPM from scratch, as we have done in Sec. 2.2.3.

1.3.2 SEP/ASEP/TASEP

The SPM also resembles the SEP/ASEP/TASEP family of models [7, 11, 16, 39], as it is an exclusion process. However, we have not found this resemblance to be particularly helpful, as these models do not contain the nearest-neighbour interactions between particles that the SPM does. Thus, we do not believe that we are able to solve the SPM using a similar matrix product solution to TASEP. Furthermore, ASEP and TASEP are manifestly asymmetric in their bulk dynamics, whereas the SPM is not.

1.3.3 The KLS Model

The Katz-Lebowitz-Spohn (KLS) model [26, 63] was originally designed to model the behaviour of ions moving stochastically under the influence of an external potential. The SPM is in fact a specific symmetric case of the 1-dimensional KLS model. Whilst the KLS model exhibits plenty of interesting behaviour (in particular, the formation of stripes during flow in higher dimensions), most of the research done into it has involved using asymmetric versions of the model to drive flow. The stationary distribution for the symmetric version on a ring is given in [26], whilst the version with open boundaries which we study here has received far less attention.

1.4 Research Outline

Our investigation into the SPM has focussed primarily upon its flow characteristics when driven by concentration gradients imposed by boundary conditions. This does not seem to have been something which has been investigated much before; as we have hinted in Sec. 1.3, most research into flow in many-body systems uses internal dynamics to drive the flow instead of the boundaries. Therefore, we are essentially working from scratch with this model. To present our results, we are using the following structure:

- We use primarily analytic methods in Ch. 2. These include the evaluation of the partition function for the SPM on a closed ring (Sec. 2.2.3), the development of the mean-field theory of the SPM (Sec. 2.3) and its generalisation to higher dimensions (Sec. 2.4).
- In Ch. 3 we introduce a method for using sparse numerical linear algebra to exactly solve the steady state distribution for small 1D SPM systems. We also show how this method can be used to compute some time-dependent quantities in Sec. 3.4.
- In Ch. 4 we discuss the use of Monte-Carlo methods to calculate the properties of the SPM in somewhat larger 1D and 2D systems. In particular we focus on the Kinetic Monte-Carlo algorithm (KMC) in Sec. 4.1.3, and calculate the bulk of our results using it.
- We summarise our main conclusions in Ch. 5.

Chapter 2

Analytical Results about the SPM

We now have a model, the SPM, which should represent the kind of behaviour in which we are interested. In this chapter, we will attempt to derive analytic results about how particles flow in the model. Initially, this was all done with the aim of producing an approximation to the behaviour in the hydrodynamic limit and thus informing us about phenomena such as surface layer formation; however, as you will see the analytic predictions suggest that the flows could be quite interesting in their own right.

2.1 Solving Problems in Nonequilibrium Statistical Mechanics

Models in nonequilibrium statistical mechanics which contain nontrivial interactions between components often produce interesting behaviour, hence the wide interest in these models. However, they usually prove to be difficult to “solve” in any concrete sense. In this section, I will give a brief overview of solution methods in equilibrium statistical mechanics, why nonequilibrium statistical mechanics problems tend to be harder to solve, and how this affects the way we approach the SPM.

2.1.1 Equilibrium Statistical Mechanics

Equilibrium statistical mechanics is a bread-and-butter part of undergraduate physics, and there are a great many texts on the subject [31, 48]. When we speak of “solving” an equilibrium statistical mechanics system, the gold standard is to be able to calculate relationships between the statistics of large-scale quantities as a function of the system constraints or their conjugates. This allows one to classify the system’s behaviour by making equations of state and identifying phase transitions, situations where at least some large-scale quantity statistics vary with respect to each other in a discontinuous manner. As you will see, the SPM itself is isomorphic to an equilibrium statistical mechanics model so long as we do not drive the system using boundary conditions (e.g. particle reservoirs with different concentrations). Once we introduce such driving forces, however, we find that we can no longer use equilibrium analysis, and things get a bit more difficult.

Exact Solutions

A quantity of key interest in equilibrium statistical mechanics is the partition function [40], usually denoted by Z . Say we have a closed classical mechanical system maintained at constant temperature T by a heat bath, so only energy can enter and leave the system (the canonical ensemble). Let its state space be Ξ , and denote an individual microstate (specific configuration of the system) by ξ . Such a system is defined by a Hamiltonian $H : \Xi \rightarrow \mathbb{R}$. The canonical partition function for this system is defined to be

$$Z(\beta) = \int_{\Xi} d\xi e^{-\beta H(\xi)}, \quad (2.1)$$

with $\beta T = 1$, where the integrand on the right hand side is the familiar Boltzmann weighting. This quantity is extremely useful, because it and its derivatives are directly related to the statistics of large-scale quantities. For example, the ensemble-averaged total energy $\langle E \rangle$ satisfies

$$\langle E \rangle = -\frac{\partial \log Z}{\partial \beta} \quad (2.2)$$

If one is able to obtain an expression for the canonical partition function by analytic means, you can calculate essentially any statistical moment of any large-scale quantity (**state variable**) you desire, and thus the system is “solved” in

the sense used above.

Approximate Methods for Analysing Equilibrium Statistical Mechanics Systems

Of course, the situation in which one can simply evaluate the partition function exactly is extremely rare in equilibrium statistical mechanics, at least in the large-scale limit (the one of principal interest, as it is required for most interesting phenomena such as phase transitions). More often, one might approximate the partition function itself, perhaps by converting the required integral (Eq. (2.1)) into an asymptotic series in one of the thermodynamic variables; this is essentially what one does when analysing a system in terms of instanton transitions [17].

Another approach is to deal directly with the state variables we are interested in themselves, and try to find approximate relationships between them in order to classify their interdependence (an **equation of state**). Equilibrium mean-field theory (**MFT**) [23] is exactly such a method. In MFT, we introduce the means of thermodynamic quantities of interest as independent variables, and then make the assumption that they have no nontrivial correlations. In practical terms, this means that for thermodynamic variables x and y , we assume that

$$\langle xy \rangle = \langle x \rangle \langle y \rangle. \quad (2.3)$$

This is of course quite an assumption to make, although it is often the case that it is true to low order in some asymptotic expansion. Typically, MFT tends to work well in higher dimensions and more weakly correlated systems. In the case of the Ising Model (the Weiss Molecular Field [57]), it incorrectly predicts a phase transition in 1D, but for 2D and above it is at least qualitatively correct.

Finally, one can attempt to sample directly from the space of microstates numerically via Monte Carlo methods, and in doing so build up information about state variables that way. We will say more about this in Ch. 4.

2.1.2 Nonequilibrium Statistical Mechanics

Nonequilibrium statistical mechanics differs from equilibrium statistical mechanics in the sense that it is “out of equilibrium”. The actual meaning of this

is that there are nontrivial currents (be they of energy, matter, or otherwise) flowing through the system. Note that it is perfectly possible for a nonequilibrium statistical mechanical system to be out of equilibrium but still in a steady state, in the sense that the system’s microstate can be constantly changing but still maintaining a fixed time-averaged ensemble distribution, allowing currents to flow.

In general, nonequilibrium statistical mechanics problems tend to be quite a lot harder to get a handle on than equilibrium statistical mechanics problems. The principal reason for this is the issue of time-dependence. In true equilibrium, where there is no flow and therefore no overall motion, there is no passage of time, which effectively reduces the number of variables under consideration. This, coupled with the second law of thermodynamics, means that whatever state we are in must be an allowed state with maximal entropy; in this case, entropy ends up acting a little bit like a Lyapunov function [47], which we can use to find candidate final states.

This is of no help to us at all out of equilibrium: asking a question such as “how much current flows across a given concentration gradient?” inherently involves time, and so we can’t just make a maximal-entropy argument to get the answer. There are occasions in the literature where a principle of “maximal entropy production” [13, 41] is invoked in order to close sets of equations, but as far as we have seen there is not yet a proof of why such a thing should in general be true.

Exact Solutions

Some problems in nonequilibrium statistical mechanics are known which have exact solutions. These include the Ising model in 1 and 2 dimensions [9], as well as a class of problems which can be solved in steady state by matrix products or Bethe ansatz [55]. These are the subject of much interest at the moment, not least because one can often use isomorphisms between systems which are known to be integrable in order to discover new integrable systems [50]. Unfortunately, building up such an exact solution to a specific problem from scratch does not seem to be possible in every case, so it remains to be seen how useful these methods really are for tackling problems of actual physical interest.

Approximations

As with equilibrium statistical mechanics, there are a bunch of approximate methods which can be invoked to probe system behaviour, some of which we have used in our research. Instead of solving the full system as an integrable system, there are approaches in which instantons are used to “patch together” local solutions to try to get a grasp of the whole picture [60]. One can, as always, simply simulate a system by numerical means and try to derive useful statistics from the output. In order to do this more efficiently, one can possibly use results from Large Deviation Theory (LDT [56]) in order to boost the strength of the tails of the distributions and so capture the essence of some useful large deviation function. However, again this doesn’t seem to be something that can be done completely generically.

Of course, mean-field theory is still an option, although now that time dependence has been added it tends to produce a set of coupled ODEs for the mean variables under consideration [29]. It is also in principle possible to study small-scale systems essentially exactly by numerical analysis of the relevant **Transition Rate Matrix** (TRM). Of course, this has the disadvantage that it is only a small finite system, so some of the phenomena observed in it will differ from larger versions of the same system. We perform this kind of analysis in Ch. 3.

2.1.3 Where does the SPM stand?

The issue of how to analyse the SPM leaves us in a slightly awkward position. It is almost as simple as the Symmetric Exclusion Process; however, the extra interaction in the SPM makes it quite different, as it is in fact longer-ranged. Thus, it is a bit difficult to see immediately how to modify a SEP matrix-product steady state in order to solve the SPM. In a similar vein, it might in fact be possible to solve the SPM exactly using the thermodynamic Bethe ansatz [55], but we have neither the expertise nor the time to properly investigate that possibility.

Instead, we have gone for a somewhat more pedestrian, traditional approach. In the rest of this chapter, we will discuss the relationships enjoyed by the SPM and some well-known models, and will then perform mean-field analysis, in the hope of obtaining some at least qualitative results about how the SPM behaves. In Ch. 3, we will then consider some semianalytic solutions to the SPM in finite systems in 1D via TRM analysis. Finally, in Ch. 4, we will compare the TRM

and MFT results to numerical simulations performed using Monte-Carlo (MC) methods. We have also performed MC calculations and have MFT results for the 2-dimensional situation.

2.2 Similarities between the SPM and Established Models in 1D

In the previous section we have discussed the various approaches one might use when attempting to derive properties of a nonequilibrium statistical mechanical system. We will now try to put these ideas into practice on the SPM. We already mentioned some of the relationships between the SPM and some established models in Sec. 1.3; here we will be a little more formal in terms of our use of these models.

2.2.1 Relationship with the Ising Model

If we implement the rules of the SPM on a periodic domain, we no longer have to deal with boundary conditions. In this special circumstance, we can find an isomorphism between this model and the Ising model with fixed magnetisation. One does this by associating the Ising spins $\sigma_i \in \{-1, 1\}$ with $\rho_i \in \{0, 1\}$ via

$$\rho_i = \frac{1}{2} (1 + \sigma_i). \quad (2.4)$$

Recalling our proof that the SPM obeys detailed balance, we saw that the equilibrium probability of finding the SPM in a state containing N particle-particle adjacencies is proportional to λ^{-N} . If our Ising Hamiltonian is defined via

$$H = \frac{1}{2} \sum_{i=1}^L J \sigma_i \sigma_{i+1} \pmod{L}, \quad (2.5)$$

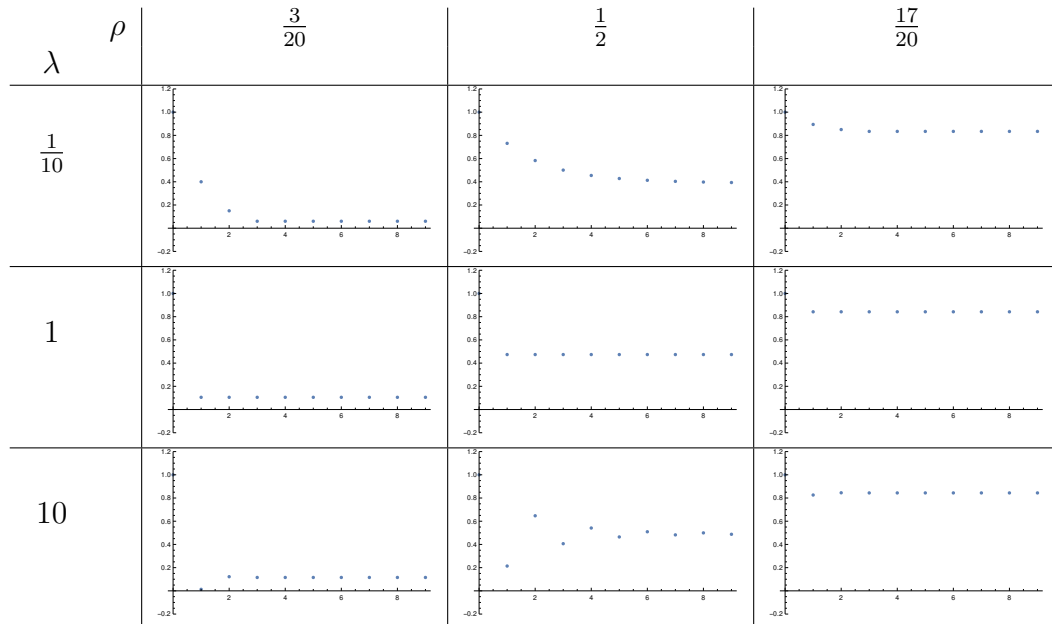
the probability of finding ourselves in a state with N paired spins is $e^{-\beta N J}$, with $\beta T = 1$. The comparison with the SPM is now obvious: we set $\log \lambda = \beta J$. Thus λ in the SPM has a one-to-one mapping to the ratio of the binding energy to the temperature in the Ising model.

2.2.2 Correlation Functions

For relatively small systems, given a system size L and a number of particles N , we can analytically compute the pairwise correlation function $C(l) = \langle \rho_i \rho_{i+l} \rangle$, or “the probability that site $i + l$ is occupied given that i is” (the system is clearly homogeneous in i , so its value is irrelevant). A Python code which performs this calculations is discussed in Sec. A.1.

This is quite a nice result, as we can use simple recursion to perform a calculation which would otherwise be quite difficult to code. Unfortunately the time complexity of the calculation grows exponentially in and L , so the largest L I can reasonably run for is 20. In the table below I have plotted the occupation probability of sites shifted from the origin (normalised so that the correlation with no shift is 1) for a selection of λ and particle densities.

Figure 2.1 Some particle-particle correlation functions for the SPM on a small closed ring, with the density fixed by the choice of how many particles to insert at the start. The system in this case has 20 lattice sites. This was calculated using computer-assisted algebra and the various density and stickiness combinations should give an overall impression as to their structure.



Clearly, as l becomes large, the correlation function tends to the density (note that the way we have defined the correlation function does not subtract this background probability; hence why many definitions do). Very small λ -values cause particles to tend to cluster together, whilst large λ values cause particles

and vacancies to tend to alternate. In theory we could use the equivalence with the Ising model to compute correlation lengths as a function of ρ and λ by using the magnetic field in the original Ising model as a Lagrange multiplier in order to fix the total magnetisation (corresponding to particle number in the SPM). However, due to the fact that we cannot accurately compute correlation functions to any decent accuracy using our numerics (see Ch. 4), we concluded that it was not worth the time to perform the calculation as we would have nothing to compare it to.

2.2.3 Calculation of the Partition Function of the SPM on a Closed Ring

Using the duality between the SPM in a closed system and the Ising Model, we can observe that the probability weighting of any configuration is proportional to λ^{-k} , where k is the number of particle-particle adjacencies in the SPM. This raises the question: if we know the weightings, can we calculate the partition function, and therefore other quantities such as the free energy or chemical potential, for the SPM on a closed ring with particle density ρ ?

In order to attempt this, we must first make two observations from the field of combinatorics:

- The number of possible ways to select, without ordering or replacement, M objects from N is

$$\binom{N}{M} = \frac{N!}{M!(N-M)!}. \quad (2.6)$$

- The number of ways to insert M unlabelled balls into N boxes is

$$\binom{N+M-1}{M-1} = \frac{(N+M-1)!}{N!(M-1)!}. \quad (2.7)$$

Now let us consider an alternative way to look at our SPM system. Instead of considering particles and vacancies moving around on a lattice of size L , let us instead consider a ring containing N boxes, into which we wish to distribute $L-N$ balls. These balls are allowed to jointly occupy boxes; this corresponds to the SPM on a ring with L slots containing N particles. The occupation numbers of the boxes represent the distances between consecutive particles in the old system.

Say we wish to distribute the balls so that only M of the boxes contain any at all; then the above two combinatorial results suggest that there are $\frac{N!}{M!(N-M)!}$ ways to choose which M boxes, into which we insert one ball each, leaving $\frac{(L-N-1)!}{(L-N)!(M-1)!}$ ways to insert the remainder. Thus, the overall number of possible ways to distribute the balls so that only M boxes contain any at all is

$$C_M = \frac{N!(L-N-1)!}{M!(N-M)!(L-N)!(M-1)!}. \quad (2.8)$$

This corresponds to the situation when there are $(N-M)$ particle-particle adjacencies in the SPM. By analogy with the Ising model, the equilibrium weighting of a configuration in which only M of the boxes are nonempty is $\lambda^{-(N-M)}$; therefore, the partition function $Z_L(\lambda, N)$ for an SPM system of size L is

$$Z_L(\lambda, N) = \sum_{M=1}^{M=\min\{N-1, L-N\}} \left[\frac{N!(L-N-1)!}{M!(N-M)!(L-N)!(M-1)!} \lambda^{-(N-M)} \right]. \quad (2.9)$$

For statistical mechanics, we are primarily interested in the situation where the system size is very large. Therefore, let us define $\rho, m \in (0, 1)$ so that $N = \rho L$ and $M = mL$, and invoke the Stirling approximation $\log x! \sim x \log x$ for large x . Regarding L as a large constant, and keeping only leading order behaviour in L , we find that

$$Z_L(\lambda, \rho) \sim \int_0^{\min\{\rho, 1-\rho\}} dm \exp L [-2m \log m + (1-\rho) \log(1-\rho) + \rho \log \rho - (1-\rho-m) \log(1-\rho-m) - (\rho-m) \log(\rho-m) - (\rho-m) \log \lambda]. \quad (2.10)$$

This integral looks quite intractable, but recall that in the limit $L \rightarrow \infty$ we can evaluate it asymptotically using Laplace's Method. This requires finding the location of extrema of the exponentiated term as a function of m ; these occur when

$$\lambda(1-m-\rho)(\rho-m) = m^2. \quad (2.11)$$

One of the solutions occurs in $(0, \min\{\rho, 1-\rho\})$, at

$$m_+ = \frac{-\lambda + \sqrt{\lambda^2 + 4\lambda(1-\lambda)\rho(1-\rho)}}{2(1-\lambda)}, \quad (2.12)$$

and a little analysis reveals that it is indeed a maximum, as required for the use

of Laplace's Method. Therefore, we find that

$$\sqrt[L]{Z_L(\lambda, \rho)} \sim \sqrt{2\pi} \frac{(1-\rho)^{1-\rho} \rho^\rho}{m_+^{2m_+} (\rho - m_+)^{\rho-m_+} (1 - m_+ - \rho)^{1-m_+-\rho}} (1 + \mathcal{O}(L^{-1})), \quad (2.13)$$

where the term relating to the curvature of the integrand around the critical point (which would usually be present when using the Laplace Method) vanishes under the action of the L^{th} root for large L . From here one can use computer algebra to obtain the free energy density $F(\rho, \lambda) = -\frac{\log Z_L}{L}$ (Fig. 2.2) and chemical potential $\mu(\rho, \lambda) = \frac{\partial F}{\partial \rho}$ (Fig. 2.3) of the SPM system.

Figure 2.2 *The variation of the SPM free energy density on a large closed ring as a function of particle density and stickiness parameter λ . The patches on the line $\lambda = 1$ are due to the way that m_+ is calculated; although a little analysis reveals that it is in fact a well-behaved removable singularity, numerical errors cause the plotting numerics to behave badly in places.*

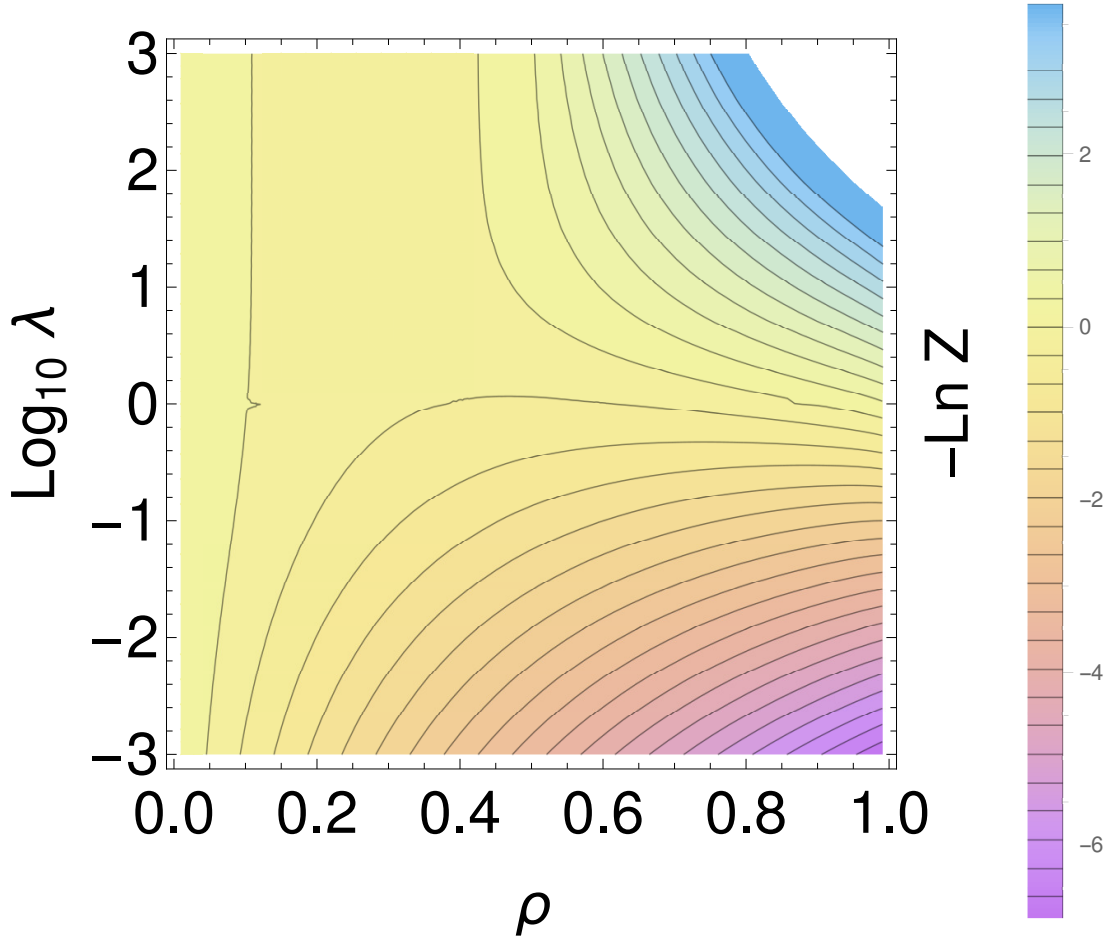
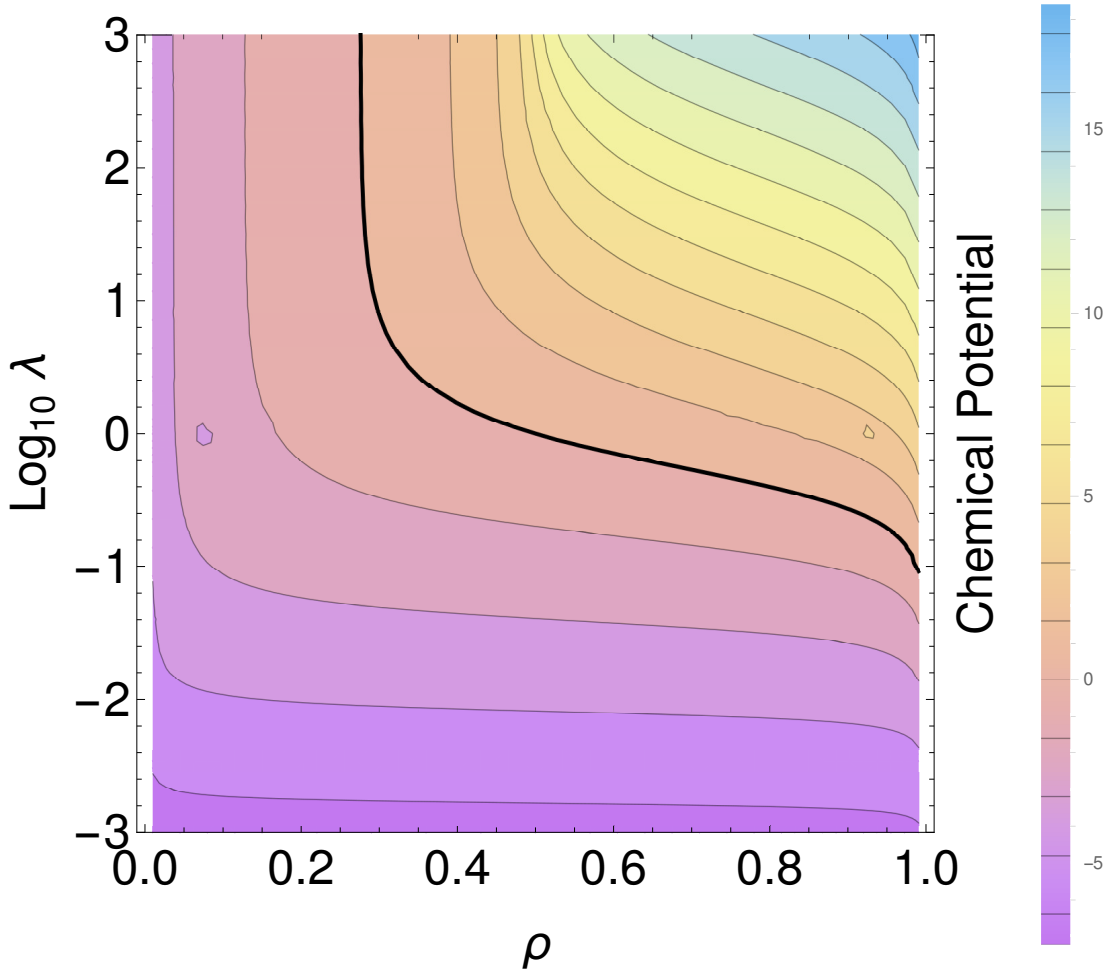


Figure 2.3 The variation of the SPM chemical potential on a large closed ring as a function of particle density and stickiness parameter λ . Again, we see some bad behaviour at $\lambda = 1$, for the same reasons as before. The curve $\mu(\rho, \lambda) = 0$ is highlighted by a thick black contour.



Of course, in thermodynamic equilibrium a system generally attempts to lower its total free energy to the lowest value allowed by the constraints. If we hold λ constant whilst allowing ρ to vary, this corresponds to the curve $\mu(\rho, \lambda) = 0$, which one can follow on Fig. 2.3; Fig. 2.2 confirms that this is indeed a minimum. Thus we should expect that a very large system connected to a particle reservoir would tend towards having a total density such that $\mu = 0$, regardless of the particle density in the reservoir, as the particle density in the system would only be pinned to that of the reservoir near to the boundary. By this logic, at large λ we would see systems tend towards a density of $\rho \sim \frac{1}{3}$, whereas for small λ the system would tend to fill. Of course, if we were to hook a system up to two different boundaries and cause a current to flow, as we have done many times in

the course of this project, that might change things, as now the system would be in a nonequilibrium steady state as opposed to a thermodynamic equilibrium, and those are not quite the same beast.

2.3 Using the Mean-Field Approximation on the SPM

For the reasons discussed in Sec. 2.1.3, we do not possess an analytic solution for the SPM on a nonperiodic bounded domain. Such a solution might exist, but we will proceed on the assumption that the model is not analytically solvable. Therefore, it would be useful to at least possess approximate analytic solutions, as this can help us by giving us something to test our numerics against, and point us in the direction of interesting behaviours which might occur. We will start by deriving the MFT on a lattice, and will then take the continuum limit (as the lattice spacing tends to zero relative to our scale of interest), as that should predict the dominant behaviour on the macroscopic scale.

2.3.1 Lattice MFT Derivation

As usual, in an MFT approximation, we will say that the equal-time probability of the $(i + 1)^{\text{th}}$ site being occupied is independent of the probability that the i^{th} site is occupied. More formally, let us denote the mean occupation of the i^{th} site at time t by $\rho_i(t)$. When we invoke the mean-field approximation, we say that the mean occupations of sites at equal times are independent; thus, the probability that site $j \neq i$ is occupied given that site i is occupied is $\rho_j(t)$. We can use this to calculate the rate at which $\rho_i(t)$ increases and decreases, and so obtain a system of coupled ODEs for $\rho_i(t)$.

Let us first consider the situation where the i^{th} site is unoccupied. The probability of this being the case is $(1 - \rho_i(t))$. A particle could move from site $(i - 1)$ or site $(i + 1)$, but only if those sites are currently occupied. Assuming that site $(i - 1)$ is occupied (occurring with probability ρ_{i-1} in MFT), the rate at which it would jump to site i would depend on the occupation of site $(i - 2)$, as it would be 1 if it were unoccupied and λ if it was occupied. Phrasing this in MFT terms, and suppressing t -dependence for brevity, the rate at which $\rho_i(t)$ is increased by

particles coming from the left is

$$\tau_0^{-1} (1 - \rho_i) \rho_{i-1} [(1 - \rho_{i-2}) \cdot 1 + \rho_{i-2} \cdot \lambda]. \quad (2.14)$$

By symmetry, the income of particles from the right is

$$\tau_0^{-1} (1 - \rho_i) \rho_{i+1} [(1 - \rho_{i+2}) \cdot 1 + \rho_{i+2} \cdot \lambda]. \quad (2.15)$$

Using similar logic, but shifting things around slightly, the rate at which particles leave site i to go to site $i + 1$ is

$$\tau_0^{-1} (1 - \rho_{i+1}) \rho_i [(1 - \rho_{i-1}) \cdot 1 + \rho_{i-1} \cdot \lambda], \quad (2.16)$$

and similarly

$$\tau_0^{-1} (1 - \rho_{i-1}) \rho_i [(1 - \rho_{i+1}) \cdot 1 + \rho_{i+1} \cdot \lambda] \quad (2.17)$$

is the rate at which particles leave i to go to $i - 1$.

At this point we introduce the quantity $\zeta = 1 - \lambda$, for neatness. The total rate at which particles enter site i is

$$\tau_0^{-1} (1 - \rho_i) [(1 - \zeta \rho_{i-2}) \rho_{i-1} + (1 - \zeta \rho_{i+2}) \rho_{i+1}] \quad (2.18)$$

whilst they leave at rate

$$\tau_0^{-1} \rho_i [(1 - \zeta \rho_{i+1}) (1 - \rho_{i-1}) + (1 - \zeta \rho_{i-1}) (1 - \rho_{i+1})] \quad (2.19)$$

Combining the rates of arriving and leaving, we obtain our main result:

$$\begin{aligned} \tau_0 \frac{\partial \rho_i}{\partial t} &= (1 - \rho_i) [(1 - \zeta \rho_{i-2}) \rho_{i-1} + (1 - \zeta \rho_{i+2}) \rho_{i+1}] \\ &\quad - \rho_i [2\zeta \rho_{i-1} \rho_{i+1} - (3 - \zeta) (\rho_{i-1} + \rho_{i+1}) + 2]. \end{aligned} \quad (2.20)$$

This is a nice result, and in theory we could stop right here and we could make a computational scheme for solving this as a sequence. However, there are a few issues. For one thing, $\rho_i(t)$ isn't the mean of a quantity whose variance is being suppressed by the law of large numbers, as is desired when using the MFT approximation. Thus, it is merely a rough sketch of what might happen, as variances and correlations between sites aren't suppressed. On the other hand, it simply relates the occupations of nearby sites, whereas we would find a description of the bulk flow to be much more useful. Therefore, we may as well take the

continuum limit to see how flow depends on concentration gradient and local density.

2.3.2 Continuum Limit MFT Derivation

To take the continuum limit, let's promote $\rho_i(t)$ to $\rho(x, t)$ so that

$$\rho_{i+m}(t) \rightarrow \rho(x + am, t). \quad (2.21)$$

Now we can Taylor expand for $\rho_{i+m}(t)$, as

$$\rho(x + am, t) = \rho(x, t) + ma \frac{\partial \rho(x, t)}{\partial x} + \frac{1}{2} m^2 a^2 \frac{\partial^2 \rho(x, t)}{\partial x^2} + \mathcal{O}(a^3). \quad (2.22)$$

Preferably with the aid of a computational algebra package (such as Wolfram Mathematica), one may directly substitute Taylor expansions for the required ρ_j into Eq. (2.20), continuing to truncate at $\mathcal{O}(a^3)$. Doing so, and collecting terms, we find that

$$\tau_0 \frac{\partial \rho}{\partial t} = a^2 \left[1 - \zeta \rho (4 - 3\rho) \frac{\partial^2 \rho}{\partial x^2} \right] + 2a^2 \zeta (3\rho - 2) \left(\frac{\partial \rho}{\partial x} \right)^2 + \mathcal{O}(a^4), \quad (2.23)$$

which may be factorised into the more convenient form

$$\frac{\partial \rho}{\partial t} = \frac{a^2}{\tau_0} \frac{\partial}{\partial x} \left\{ [1 - \zeta \rho (4 - 3\rho)] \frac{\partial \rho}{\partial x} \right\}, \quad (2.24)$$

which is a continuity equation

$$\frac{\partial \rho}{\partial t} = \frac{\partial J}{\partial x} \quad (2.25)$$

with current

$$J = -\frac{a^2}{\tau_0} [1 - \zeta \rho (4 - 3\rho)] \frac{\partial \rho}{\partial x}. \quad (2.26)$$

Considering Fick's Law

$$J = -D \frac{\partial \rho}{\partial x}, \quad (2.27)$$

we see that our diffusion coefficient is

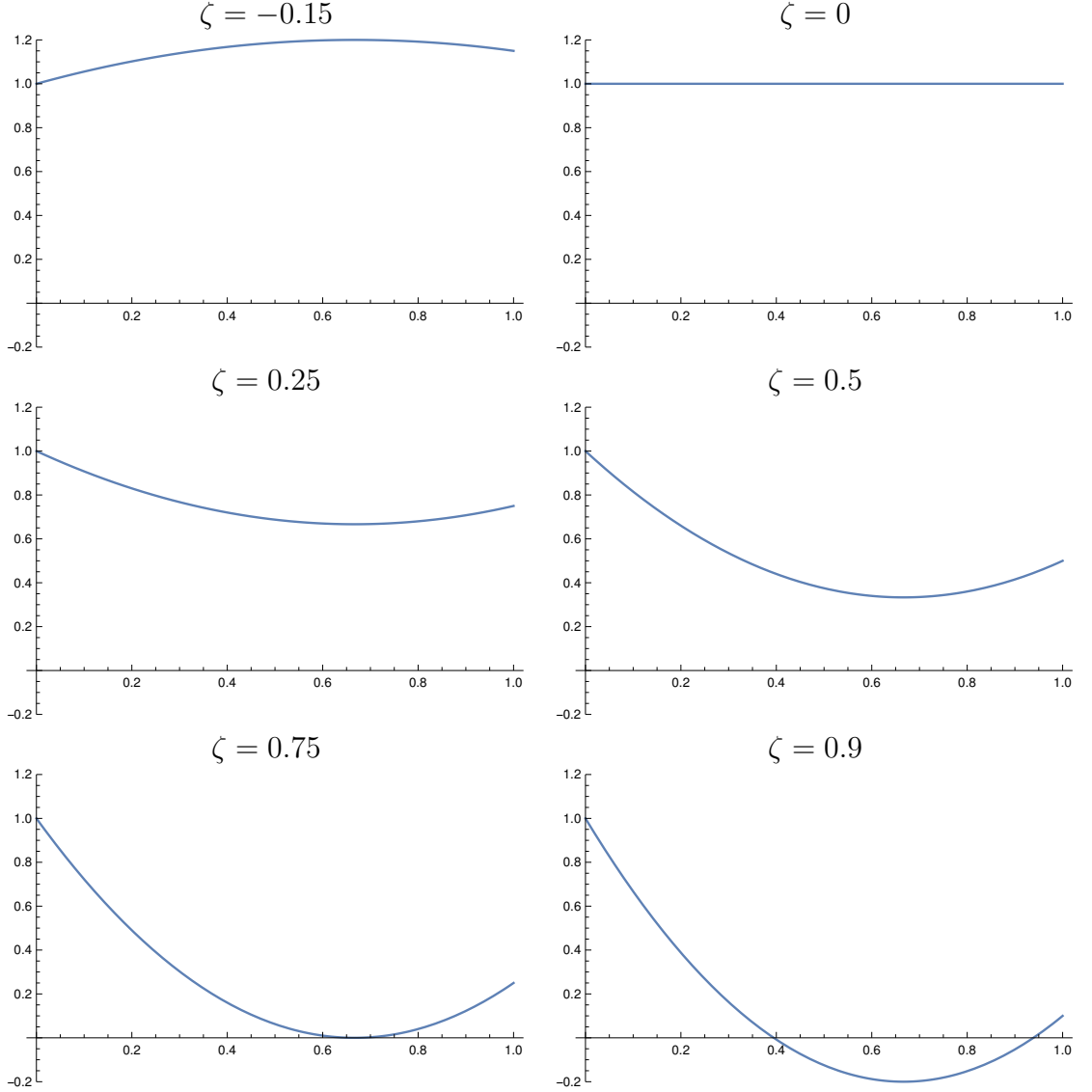
$$D = \frac{a^2}{\tau_0} [1 - \zeta \rho (4 - 3\rho)]. \quad (2.28)$$

Setting $\zeta \rightarrow 0$ (i.e. $\lambda = 1$), we see that $D \rightarrow \frac{a^2}{\tau_0}$, which is consistent with what

we would expect for SEP.

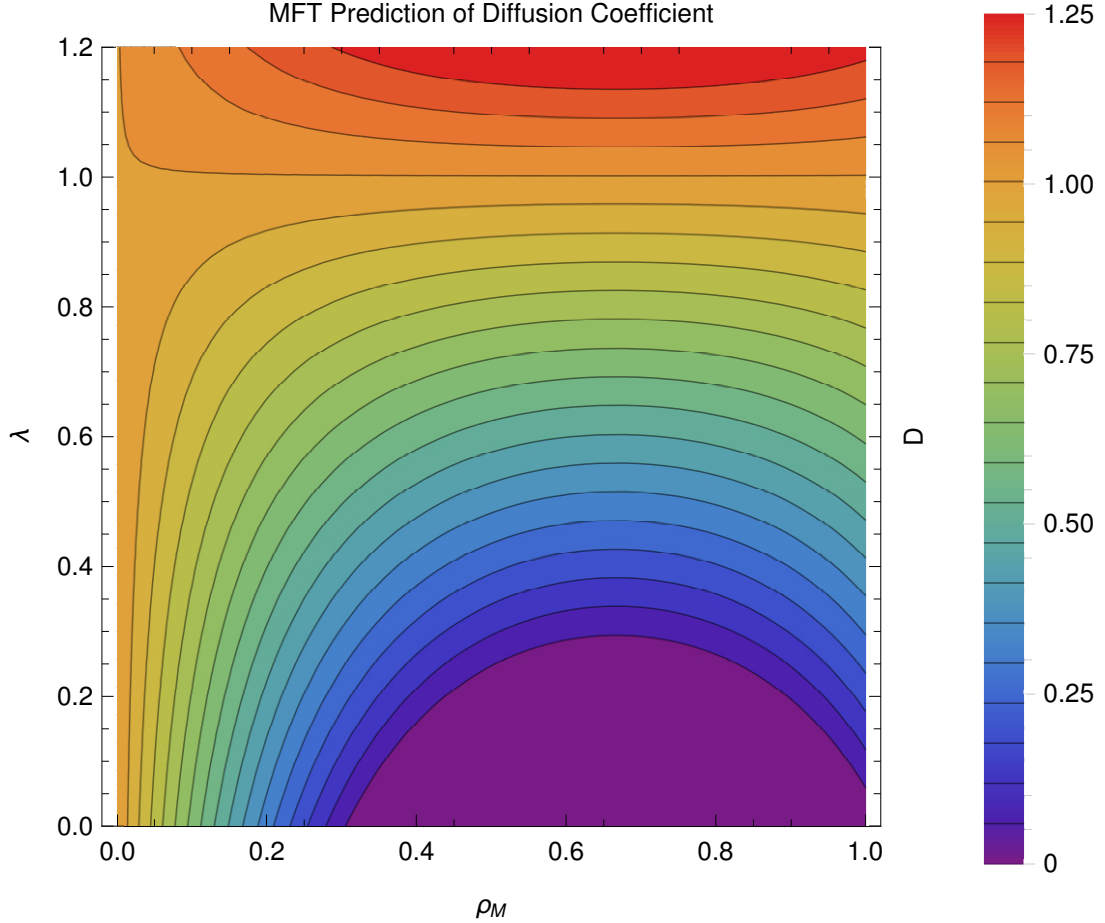
Clearly, the diffusion coefficient varies quadratically with ρ . This is easiest to see via a few graphs, as shown in Fig. 2.4. Note that $D \rightarrow \frac{a^2}{\tau_0}$ as $\rho \rightarrow 0$ and $D \rightarrow \frac{a^2}{\tau_0} \lambda$ as $\rho \rightarrow 1$, so for $\zeta < 0$ ($\lambda > 1$) D is guaranteed to be positive for $\rho \in [0, 1]$ as the diffusion coefficient is an inverted parabola so far as its variation in ρ is concerned.

Figure 2.4 Plots of the variation of $\frac{\tau_0 D}{a^2}$ (y-axis) with respect to ρ (x-axis), evaluated with various values of ζ (indicated above plots).



Note that D has a symmetry in ρ around $\rho = \frac{2}{3}$, in the sense that D is unchanged under $\rho \mapsto \frac{4}{3} - \rho$. Why this symmetry is present in the MFT is a little unclear as $\rho \mapsto 1 - \rho$ would be a much more obvious choice; however, as you will see in

Figure 2.5 A contour plot of the variation of $\frac{\tau_0 D}{\alpha^2}$ as a function of ρ and λ . The region with negative diffusion (which is really critically slow or zero diffusion due to our stability argument in 2.3.3) has been highlighted in purple. Note how as we descend in λ with $\lambda < \frac{1}{4}$, this region grows from a single point at $\rho = \frac{2}{3}$ to fill most physically realistic density values.



the numerical simulations, it does seem to be quite relevant, particularly in the high- λ limit.

2.3.3 Negative Diffusion Coefficients

A quick inspection of the dependence of the diffusion coefficient D upon ζ reveals that it is possible for strange things to happen in this MFT. For a given value of ζ , D is quadratic in ρ ; a natural question to ask is whether D is always positive, and if not, what the physical implications of this would be.

An easy way to do this is by analysing the roots of D . Writing it as a standard

quadratic,

$$D = \frac{a^2}{\tau_0} [3\zeta\rho^2 - 4\zeta\rho + 1] \quad (2.29)$$

which has discriminant $4\zeta\frac{a^4}{\tau_0^2} [4\zeta - 3]$. For a real quadratic, the discriminant changes sign when the solutions switch between being real and complex, which in our case is the difference between having real solutions and not having real solutions. Assuming that $\zeta > 0$ (as we know D is positive for $\rho \in [0, 1]$ for $\zeta < 0$), this change occurs when $\zeta = \frac{3}{4}$, corresponding to $\lambda = \frac{1}{4}$, so there are no real solutions for $\zeta < \frac{3}{4}$ and $\lambda > \frac{1}{4}$, and therefore D is guaranteed to be positive in these regions. Positive- D is the normal situation in physics, and a solution to the MFT PDE Eq.(2.24) which contains only positive- D regions is at least self-consistent (although of course is only as good an approximation to the SPM as the continuum MFT assumptions allow).

When $\zeta > \frac{3}{4}$, D is negative so long as

$$\frac{2}{3} - \frac{\sqrt{\zeta(4\zeta - 3)}}{3\zeta} < \rho < \frac{2}{3} + \frac{\sqrt{\zeta(4\zeta - 3)}}{3\zeta}; \quad (2.30)$$

this is like a gap opening up in ρ when $\zeta > \frac{3}{4}$. At its maximal extent (when $\zeta = 1$), negative diffusion occurs for

$$\frac{1}{3} < \rho < 1, \quad (2.31)$$

so there is still a region where ρ is sufficiently low that negative diffusion does not occur.

In terms of what a negative diffusion coefficient actually means, consider a constant solution $\rho(x, t) = \rho_0$. Insertion into Eq. (2.24) quickly confirms that this is indeed a solution. Now consider adding a small perturbation $\delta\rho(x, t)$ to ρ_0 . The equation for the time evolution of $\delta\rho$ then reads

$$\frac{\partial\delta\rho}{\partial t} = \frac{a^2}{\tau_0} [1 - \zeta\rho_0 (4 - 3\rho_0)] \frac{\partial^2\delta\rho}{\partial x^2}. \quad (2.32)$$

This becomes a little clearer if one takes a Fourier transform with respect to x , so that $\hat{\delta\rho}(k, t) = \mathcal{F}(\delta\rho(x, t))$; then, the equation of motion for $\hat{\delta\rho}$ is

$$\frac{\partial\hat{\delta\rho}}{\partial t} = -k^2 \frac{a^2}{\tau_0} [1 - \zeta\rho_0 (4 - 3\rho_0)] \hat{\delta\rho}. \quad (2.33)$$

This shows us that so long as $\zeta < \frac{3}{4}$, small perturbations to the density are suppressed by exponential decay in time with increasing intensity as their wavenumber increases for all wavenumbers, and so the solution is stable; the same applies if $\zeta > \frac{3}{4}$ so long as we do not stray into situations where

$$\frac{2}{3} - \frac{\sqrt{\zeta(4\zeta - 3)}}{3\zeta} = \rho_- < \rho_0 < \rho_+ = \frac{2}{3} + \frac{\sqrt{\zeta(4\zeta - 3)}}{3\zeta}. \quad (2.34)$$

If we do find ourselves in this regime, small perturbations grow exponentially with time in a situation akin to ripening [58], which, given that the particles are undergoing conserved flow, suggests that we will have a separation into regions with lower and higher densities. Of course, the positive feedback driving this separation stops if the density grows higher or lower than ρ_{\pm} , where we reenter the stable regime. This does suggest that in the MFT a system containing a negative- D region would have a tendency to self-organise itself into alternating domains, with at least the boundaries of these domains having densities of ρ_- or ρ_+ . This is very important: whilst it is no coincidence that these critical values of the density are those densities where our diffusion coefficient is zero, this does suggest that **a solution to the continuum MFT in the $\lambda < \frac{1}{4}$ regime which contains values for ρ in the critical gap $[\rho_-, \rho_+]$ should admit no current.** The search for this predicted effect is in fact the main driving force behind this entire PhD project.

2.3.4 Continuum Limit MFT Solutions

The continuum-limit MFT has given us a partial differential equation for $\rho(x, t)$; therefore, we should try to find some solutions to it, as these may give us clues as to what types of behaviour the SPM might exhibit.

Steady Flow Across a Bounded Domain

It is pretty obvious that $\rho = \rho_0 = \text{const.}$ is a solution to the MFT PDE, and it takes only a little thought to notice that this is in fact the only spatially homogeneous solution available. If we instead look for a solution which lacks time dependence (i.e. $\rho(x, t) = \rho(x)$), the PDE reduces to the ODE

$$-\frac{a^2}{\tau_0} \frac{d}{dx} \left([1 - \zeta\rho(4 - 3\rho)] \frac{d\rho}{dx} \right) = 0. \quad (2.35)$$

Integrating both sides with respect to x , and using the fundamental theorem of calculus, we find that

$$-\frac{a^2}{\tau_0} [1 - \zeta\rho(4 - 3\rho)] \frac{d\rho}{dx} = J_0, \quad (2.36)$$

with J_0 an arbitrary constant, which has been labelled as such in hindsight because it represents the constant current flowing through the system in a steady state. Doing so again, we find that we can invoke the chain rule via

$$J_0(x - x_0) = -\frac{a^2}{\tau_0} \int dx \frac{d\rho}{dx} [1 - \zeta\rho(4 - 3\rho)] \quad (2.37)$$

$$= -\frac{a^2}{\tau_0} \int d\rho [1 - \zeta\rho(4 - 3\rho)] \quad (2.38)$$

$$= -\frac{a^2}{\tau_0} \rho [1 + \zeta\rho(\rho - 2)], \quad (2.39)$$

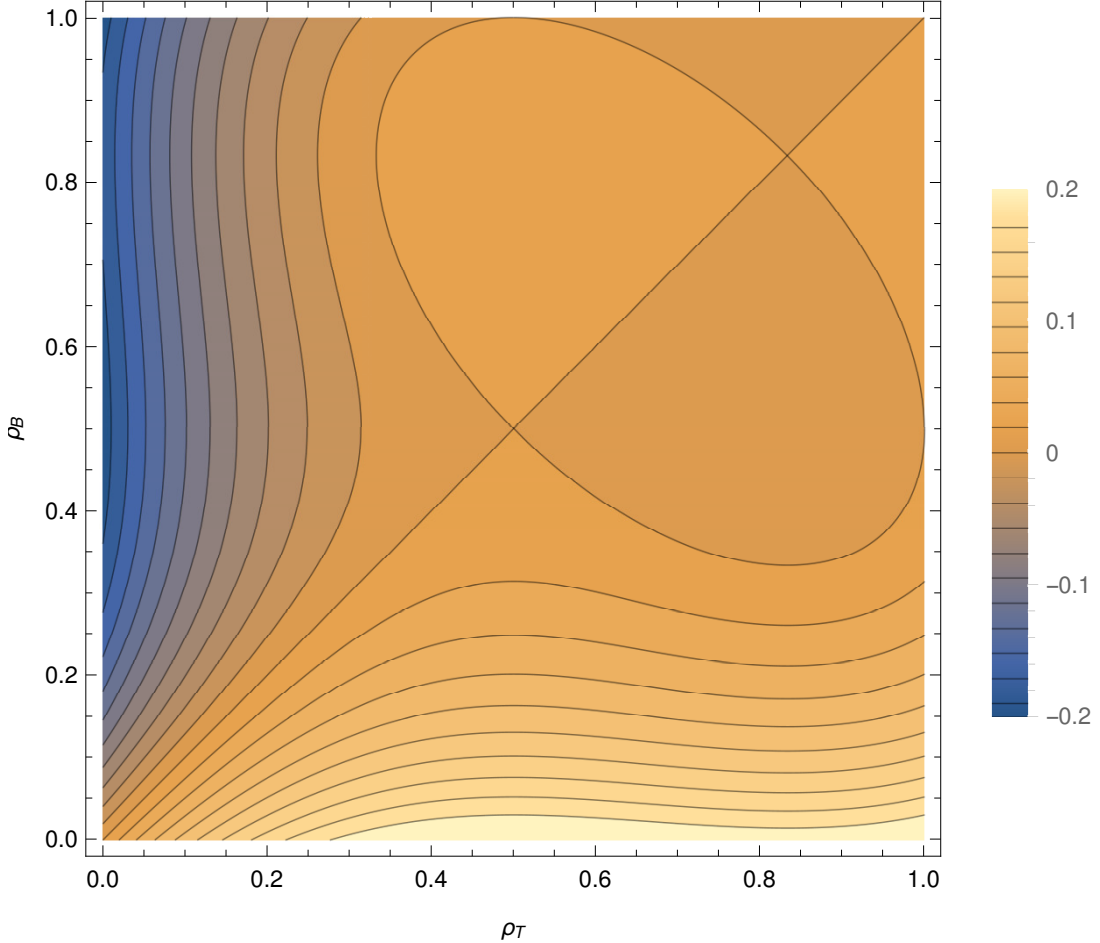
where x_0 absorbs the constant of integration. Thus with a little rearrangement we have x as a function of ρ , with ρ a cubic in x . We can in principle invert this to obtain $\rho(x)$, but let us first consider the appropriate boundary conditions to use.

Let us consider solving problems on a bounded domain; we choose to do this as opposed to an infinite one, as one can see that for our cubic $\|x\| \rightarrow \pm\infty \implies \|\rho\| \rightarrow \pm\infty$ for nontrivial J . Therefore let us consider solutions on the domain $[0, L]$ for $L > 0$. With a second order ODE of this kind, we must supply two boundary conditions, which may be Dirichlet, Neumann or some mixture of the two, and must contain at least one piece of Dirichlet information. However, our ODE does not make any special reference to ρ values of 0 or 1, and therefore if we do not fix ρ at both boundaries it is highly likely that the solution will contain unphysical values for ρ . Therefore, let us apply Dirichlet conditions at both boundaries, so that $\rho(0) = \rho_0$ and $\rho(L) = \rho_L$. Inserting this information into Eq. (2.37) we can fix the constants x_0 and J_0 ; in particular we find that

$$J_0 = \frac{a^2}{L\tau_0} [\rho_0 - \rho_L + \zeta (\rho_0 [\rho_0^2 - 2] - \rho_L [\rho_L^2 - 2])], \quad (2.40)$$

which can be reinserted to yield the desired x_0 . Note that the current is not directly proportional to the concentration difference between the boundaries; thus, the MFT predicts violation of Fick's Law. An illustrative plot of $J_0(\rho_0, \rho_L)$ is shown in Fig. 2.6.

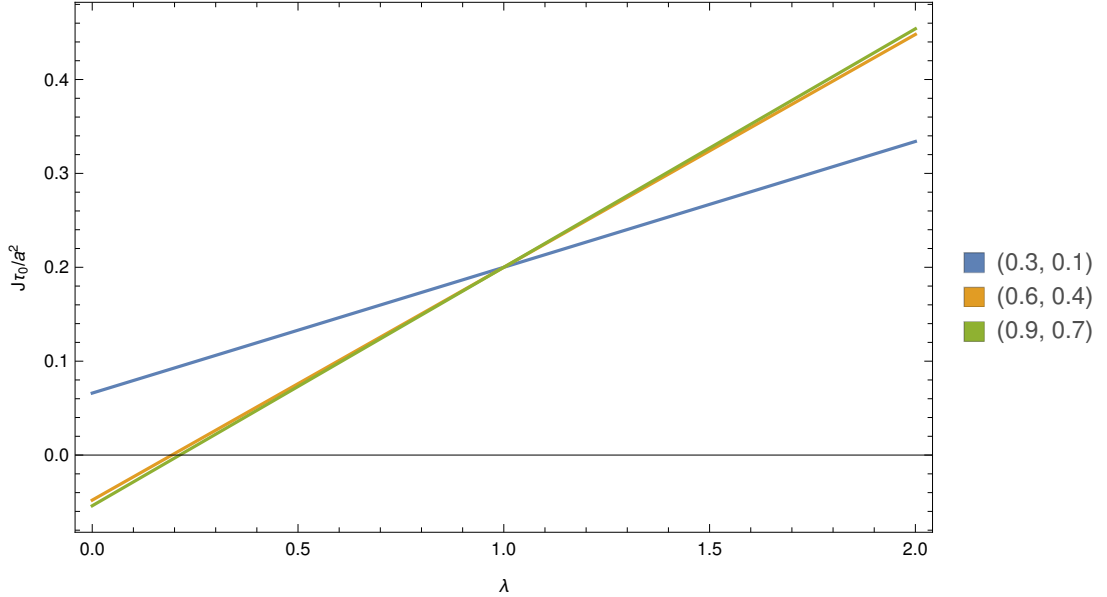
Figure 2.6 A contour plot of the variation of the constant current $J_0(\rho_B, \rho_T)$ in a bounded domain with boundary densities ρ_0 and ρ_L at $x = 0$ and $x = L$ respectively, with $\lambda = 0.2$. Notice how the magnitude of J_0 generally grows as the difference between ρ_0 and ρ_L increases, and how there is a region of boundary condition space in which the current takes the opposite sign one would expect.



This solution in particular is extremely useful, as we can use it to predict the flow which should occur (MFT being correct) if we set up a numerical simulation of the SPM with a length of, say, L lattice points. In particular, if we vary λ whilst keeping the boundaries constant, the measured current should vary linearly, as depicted in Fig. 2.7. Thus, if we were to run simulations with, say, $(\rho_0, \rho_L) = (0.6, 0.4)$, we should see the transition to a backwards or critically slow flow occur. We can use Eq. (2.40) to find the critical value for λ , λ_c , at which the transition to negative diffusion should occur for given boundary conditions. To do this, we simply set $J_0 = 0$ and solve for λ , and find that

$$\lambda_c = 1 - \frac{1}{2(\rho_0 + \rho_L) - (\rho_0 + \rho_L)^2 + \rho_0 \rho_L}. \quad (2.41)$$

Figure 2.7 A plot of the MFT prediction of the dedimensionalised flow rate with varying λ for boundaries $(\rho_0, \rho_L) = \{(0.3, 0.1), (0.6, 0.4), (0.9, 0.7)\}$. Notice how the dependence of J on λ is actually very similar for the high and medium boundary-density-average situations, but is quite different for the low density case. Note that the MFT clearly predicts that the flow should start running backwards when λ becomes sufficiently low, which means that we should be able to see backwards or critically-slow flow in our numerics if we hold the boundaries constant whilst varying λ .



This is shown in Fig 2.8.

We can also obtain a prediction of the system-wide average density

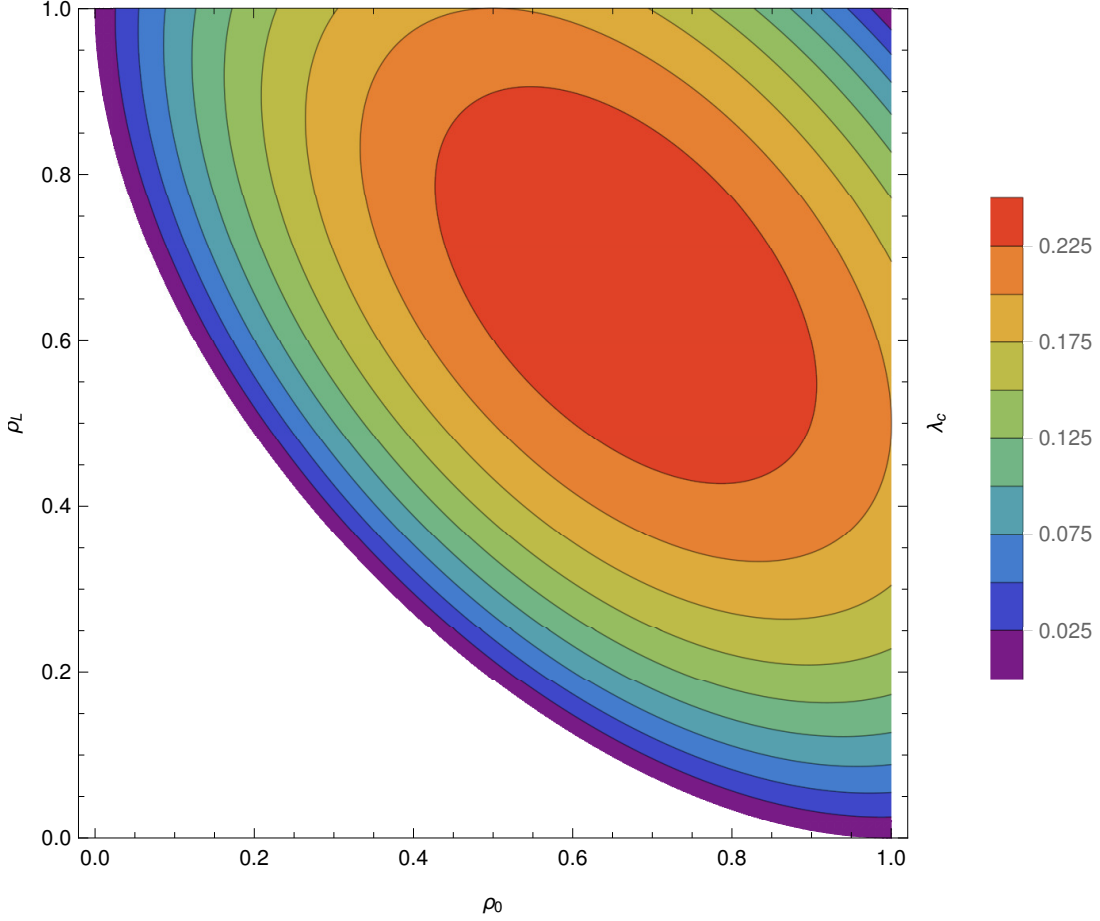
$$\bar{\rho} = \frac{1}{L} \int_0^L dx \rho(x), \quad (2.42)$$

so long as we can invert $x(\rho)$ to find $\rho(x)$ uniquely. The easiest way to do this is using the main result in [30], yielding

$$\bar{\rho} = \frac{6(\rho_0 + \rho_L) + \zeta [9(\rho_0^3 + \rho_L^3) - 16(\rho_0^2 + \rho_L^2) + \rho_0 \rho_L (9[\rho_0 + \rho_L] - 16)]}{12[1 + \zeta(\rho_0^2 + \rho_L^2 + \rho_0 \rho_L - 2[\rho_0 + \rho_L])]}, \quad (2.43)$$

to obtain this one simply imposes the conditions that $\rho(0) = \rho_0$ and $\rho(L) = \rho_L$, and then solves for J_0 and back-substitutes. The variation of the average density with λ for selected fixed boundary conditions is plotted in Fig. 2.9. In general, this overall density deviates very little from the average of the two boundary densities.

Figure 2.8 A plot of the critical value λ_c , specified in Eq. (2.41), which λ must be smaller than in order to cause backward flow with boundary densities (ρ_0, ρ_L) . The region for which λ_c is negative is not included and marked in white, as $\lambda > 0$ for a physically realistic system. This shows that there are boundary configurations for which flow should still occur for arbitrarily small values of λ .

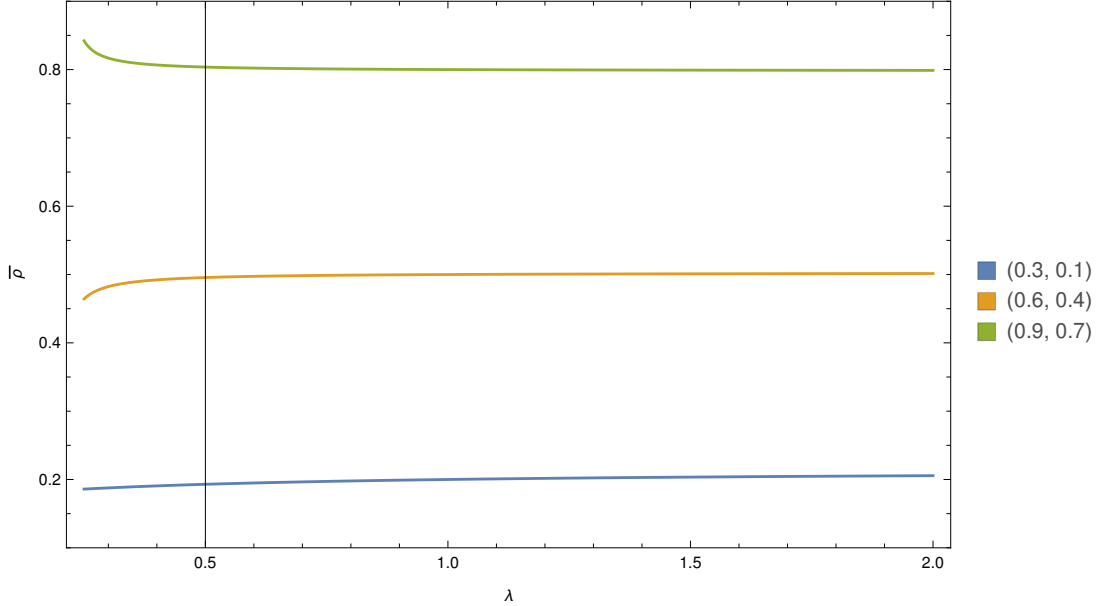


Other Analytic Solutions

Steady flow across a bounded domain is not the only solution for the continuum-limit MFT. We can also attempt to exploit Lie symmetries in the equations to generate solutions. Using the results in [25], we see that there should exist solutions of the form $\rho(x, t) = \phi(\omega)$ with $\omega = x - vt$ for some real v ; intuitively, this corresponds to a solution which simply translates through time with velocity v . After a little rearrangement, this implies that

$$v \frac{d\phi}{d\omega} = -\frac{a^2}{\tau_0} \frac{d}{d\omega} [1 - \zeta\phi(4 - 3\phi)] \quad (2.44)$$

Figure 2.9 A plot of the MFT prediction of the overall system-wide density with varying λ for boundaries $(\rho_0, \rho_L) = \{(0.3, 0.1), (0.6, 0.4), (0.9, 0.7)\}$. We have only plotted for $\lambda > \frac{1}{4}$, as outside this regime the MFT prediction is not unique, and so the inversion formula we need to calculate the density is not valid. In each case the density rarely deviates far from the average of the two boundary densities.



which may be integrated and then solved as a first order ODE to obtain

$$\omega = \frac{a^2}{\tau_0 v} \left[\frac{1}{2} \zeta \phi (8 - 6\mu - 3\phi) - (1 - \zeta [4 - 3\mu] \mu) \log(\phi - \mu) \right] + \omega_0, \quad (2.45)$$

where ω_0 and μ are constants.

Now we need as usual to consider what kind of boundary conditions to use. For simplicity, let us consider a wave of density travelling into an empty region; this implies that $\phi \rightarrow 0$ as $\omega \rightarrow \infty$. The only way to achieve this is by setting $\mu = 0$, leaving us with

$$\omega(\phi) = \frac{a^2}{v\tau_0} \left[\frac{1}{2} \zeta \phi (8 - 3\phi) - \log \phi - \frac{5}{2} \zeta \right] + \omega_0. \quad (2.46)$$

As we can vary ω_0 to shift solutions around in ω essentially arbitrarily, we can choose where ϕ takes a desired value. For convenience, let's make ϕ take the value 1 at $\omega = 0$, which is easily achievable by setting $\omega_0 = 0$. At this point, we are faced with the prospect of trying to invert Eq. (2.46). This would be annoying, although one could be assisted by numerics to lighten the load. However, we can gather plenty of information simply by taking some limits. As $\omega \rightarrow \infty$, $\phi \rightarrow 0$

by design, and so $\phi(\omega) = \mathcal{O}(e^{-\frac{v\omega\tau_0}{a^2}})$; having an exponential tail at the leading edge of the wave, with a thickness proportional to the default diffusion coefficient divided by the wave speed, makes perfect sense. Meanwhile, by considering small variations in ϕ around 1, we may derive that $\phi \sim 1 - \frac{v\tau_0}{a^2\lambda}\omega$ as $\omega \rightarrow 0$. One could see this as being a front, behind which the system is filled by a shock wave moving with velocity v . Notice how both limits suggest that the leading edge of the wave becomes thinner with increasing wavespeed, whilst close to the full region it thickens in proportion to λ .

However, we are left with the problem that we have the free parameter v in the solution. One might hope that we can find the preferred value for v by means of a speed-selection argument as is done with the Fisher-KPP equation [51], but that does not work in this case as the wave tail thickness is monotonic in the wave speed. Therefore, the wave speed seems to be dictated by the initial conditions, which allows some rather bizarre behaviour. For example, in the limit $v \rightarrow +\infty$, the initial condition (in other words, setting $t = 0$ and observing that $\rho(x, 0) = \phi(x)$) resembles an inverted Heaviside step function for $x > 0$; thus this suggests that if we were to start the system with initial condition $\rho(x, 0) = 1 - H(x)$, the high-density region would advance into the low-density region with infinite velocity, regardless of a , τ_0 or λ . This seems somewhat unphysical, and serves as a reminder that the MFT is a guide only, and shouldn't be expected to accurately predict the behaviour of the SPM.

Using [25] there is one last type of solution based upon symmetry. To acquire it, let us define $\xi = \frac{x}{\sqrt{t}}$ and $\rho(x, t) = \chi(\xi)$; then our PDE reduces to

$$\xi \frac{d\chi}{d\xi} = -2 \frac{a^2}{\tau_0} \frac{d}{d\xi} [1 - \zeta\chi(4 - 3\chi)]. \quad (2.47)$$

Taking $\zeta = 0$, this clearly reduces to the standard similarity solution of the diffusion equation as we would expect, so this is the nonlinear analogue of that. Unfortunately, this is a nonlinear second order ODE which isn't particularly amenable to solution, so after some solution attempts we decided to give up at this point and focus on numerics and other analytic avenues.

2.3.5 Implications of Continuum MFT Breakdown

We have already mentioned that the MFT can predict negative diffusion coefficients for $\lambda < \frac{1}{4}$, $\rho \in (\rho_-, \rho_+)$ as defined in Eq. (2.34). However, we should investigate this in a little more detail, as it has testable implications for the SPM.

Treating the MFT at face value, our stability analysis in 2.3.3 suggests that in the event that we have a region with $\rho \in (\rho_-, \rho_+)$ there should be a tendency for the medium to separate into parts which have $\rho \notin (\rho_-, \rho_+)$; of course, the first ρ s for which $\rho \notin (\rho_-, \rho_+)$ are ρ_- and ρ_+ themselves, which are the values for which the diffusion coefficient, and therefore the current resulting from a concentration gradient is zero. So, the process of the medium separating should in general yield a mixture of regions with $\rho = \rho_-$, $\rho = \rho_+$ and other $\rho \notin (\rho_-, \rho_+)$, mixed in such a way that the total number of particles is locally conserved.

It is this nonuniqueness of configuration which causes us some problems if we try to accept the MFT as a good descriptor of SPM phenomenology. In reference to our steady state solution described in 2.3.4, note that $\rho(x)$ is only unique so long as we avoid negative diffusion, otherwise, the cubic inversion we need to perform to transform $x(\rho)$ into $\rho(x)$ is multivalued. One could imagine that we could fix this by patching together sections which cross with $\rho = \rho_-$ or ρ_+ , but then we have essentially unlimited choice of how large to make the sections and how many alternations to include. This means that the MFT makes no prediction of the system-wide average density $\bar{\rho}$ which is unfortunate as this is a quantity which it is easy for us to measure using our numerics.

2.4 The SPM in Higher Dimensions

We initially designed the SPM for use in one dimension, as it was originally intended to represent interacting particles moving along a periodic potential with deep, narrow wells. However, it is only natural to wonder whether a similar model could be constructed in higher dimensions. Recall from Sec. 1.2 that the SPM in one dimension has three properties:

- Spatial homogeneity, which is pretty standard, and we will not mention from now on,

- left-right symmetry, and
- locality, in the sense that only the presence or absence of a particle in an adjacent lattice site may influence the transition rate.

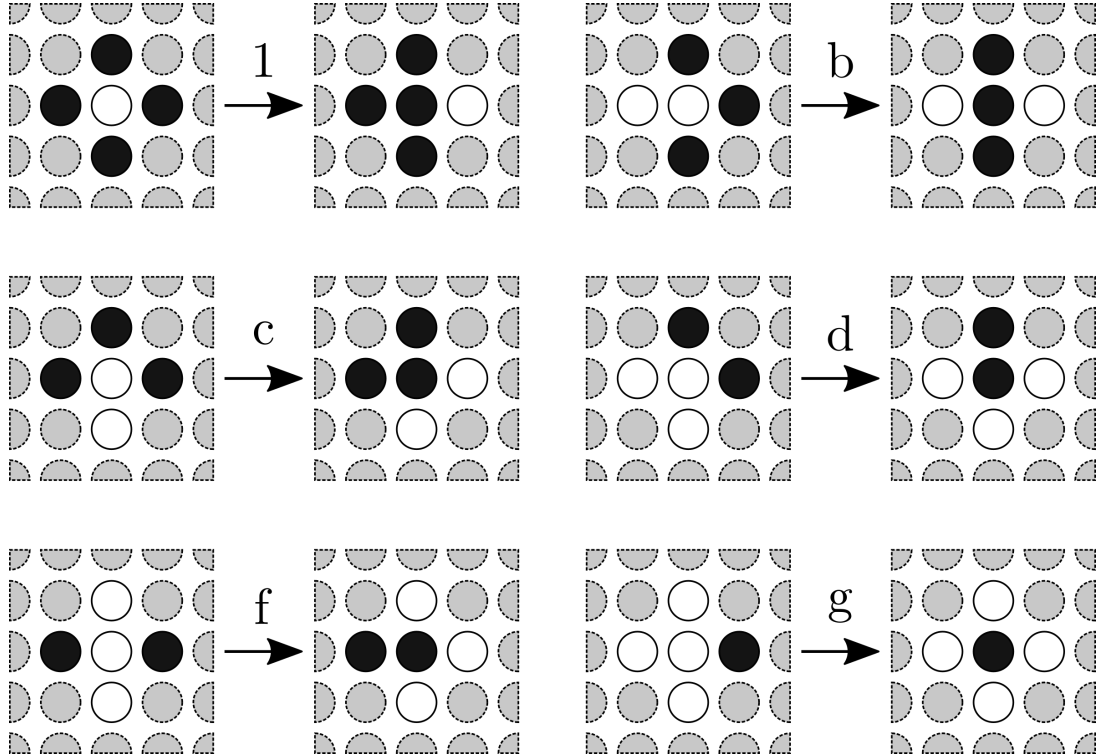
In addition we also proved that (boundary conditions aside) the SPM also obeys detailed balance. This was not put into the model intentionally, but emerges naturally as the space of possible one-dimensional models which are local and symmetric is very small. Let us consider only square lattices in n dimensions, for simplicity. If we attempt to build a model in two dimensions which is symmetric and local, (i.e. obeys all the point group symmetries of the underlying lattice, and whose transitions are only influenced by the immediate environment around a particle), we find that we now have more freedom in the model construction than we did in one dimension. For example, in two dimensions a moving particle might be leaving any one of six possible unique local configurations, as shown in Fig. 2.10, and so such a model would need to be parametrised by 5 rates, once we take time rescaling into account. The number of possible symmetric local hopping models only grows greater in higher dimensions, and this makes it very difficult to analyse the parameter space of such models using numerics. Therefore, we have chosen to investigate most closely those models which in addition obey detailed balance; as it turns out, there is only one such model, regardless of the number of dimensions.

2.4.1 Symmetry + Locality + Detailed Balance = Unique 1-Parameter SPM

When investigating higher-dimensional analogues of the SPM, we initially considered a generic model as shown in Fig. 2.10; however, as the parameter space is so large, we decided to attempt to impose the detailed balance condition and see how much freedom that gave the model. In the end, after some exceedingly tedious casework, we found that in order to obey detailed balance particles needed to move with transition rates specified by the following theorem, which applies in arbitrary numbers of dimensions:

Theorem 1. *Any processes defined on an n -dimensional square lattice in which particles swap places with vacancies and whose transition rates $\sigma(\xi_1 \rightarrow \xi_2)$*

Figure 2.10 The unique available moves in a 2-dimensional symmetric local hopping model. Note that we have rescaled time so that the free particle hopping rate is 1, for consistency with the 1-dimensional SPM. Simultaneous rotations or reflections of both initial and final states are also allowed moves with the same rates. White corresponds to a lattice site occupied by a particle, black to an unoccupied site, and grey to a site which has no effect on the transition rate. In each case a particle moves into an empty space to its right, with its different starting environment determining the transition rate.



- are symmetric (invariant under rotations, reflections and translations of the underlying lattice),
- local (rate at which a particle swaps with a vacancy only depends upon configuration of particle's immediate neighbours),
- and obey detailed balance, i.e. that \exists probability distribution P over configurations $\xi \in \Xi$ such that $\forall \xi_1, \xi_2 \in \Xi$,

$$P(\xi_1)\sigma(\xi_1 \rightarrow \xi_2) = P(\xi_2)\sigma(\xi_2 \rightarrow \xi_1), \quad (2.48)$$

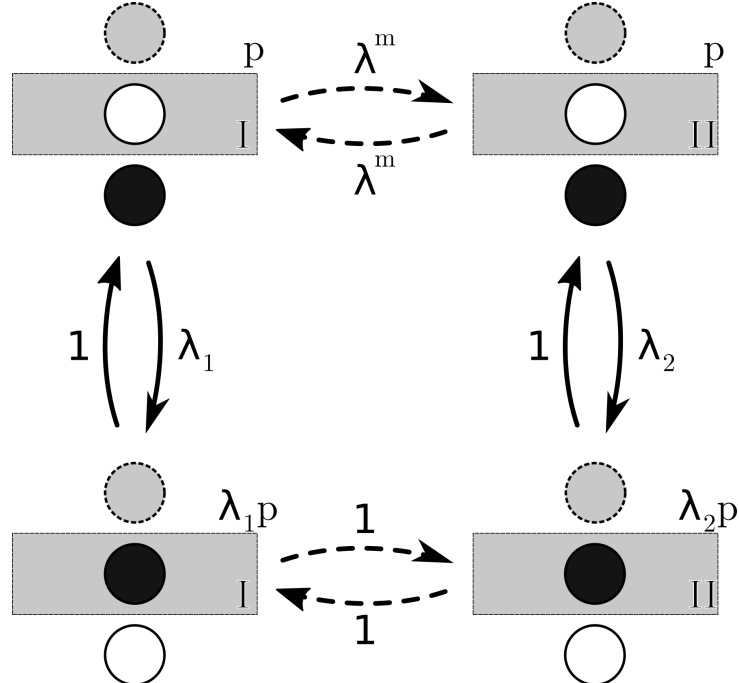
must have a transition rate of the form

$$\sigma(\xi_1 \rightarrow \xi_2) = \frac{1}{\tau_0} \lambda^m, \quad (2.49)$$

where m is the number of particles directly adjacent to the particle which is attempting to swap with a vacancy and τ_0 is an arbitrary constant.

Proof. We have already shown (Sec. 1.2) that the theorem applies in 1-dimension, as there the space of possible models is so constrained that there is only one symmetric local model, which is the SPM. This model, as we showed, obeys detailed balance anyway, so we're done for $n = 1$.

Figure 2.11 *I and II represent two local configurations of m particles, centred around a single site, which may or may not be occupied, in an $(n - 1)$ -dimensional hyperplane intersecting the central site. The dashed arrows represent configurational transitions which require multiple steps, all with the same rate (in this case, λ) as indicated. The grey particle slot represents a slot whose occupation is irrelevant for this calculation, although it must be constant throughout. The expressions in the top right corners of the configurations are the probabilities of our finding the system in that configuration.*



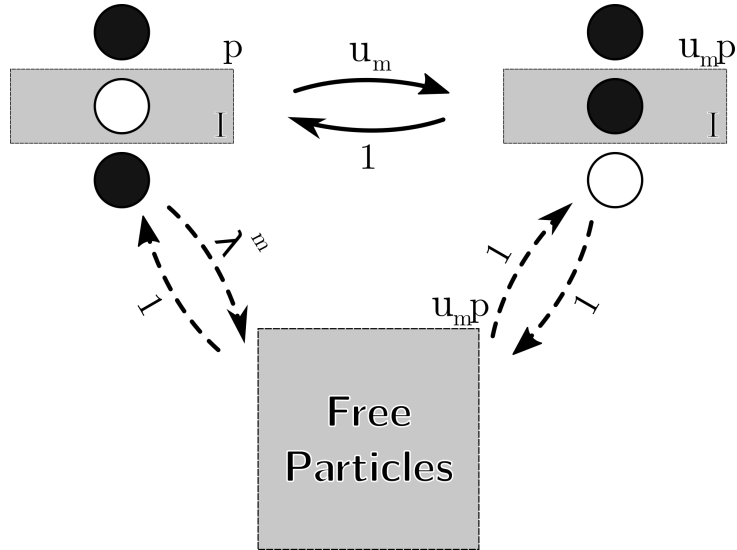
We will proceed with the proof via induction. Let us assume that the result is true in $(n - 1)$ dimensions. Firstly, we need to show that the actual configuration of the particles in contact with a particle does not affect its rate of motion into an adjacent free space. Fig. 2.11 shows just such a situation: there are m particles clustered around the central particle in an $(n - 1)$ -dimensional hyperplane, but in two different local configurations, I and II. Because the model in $(n - 1)$ -d obeys detailed balance, we can consider a reversible chain of moves from one

configuration to the other. We do this by moving each particle adjacent to the central particle outwards, with rate λ . Once they are all separated from the central particle, we can then move them around at leisure, with each move having rate 1 so long as we keep them separate; luckily, there is plenty of room to do this, as we can simply move the particles further away using only rate 1 moves. We can then rebuild the particles from, say, configuration I into their exact state in configuration II. Furthermore, we can do exactly the same thing going from configuration II to configuration I, again using only m rate λ moves and the rest with rate 1. Importantly, if a system obeys detailed balance, then if we can move from one state to another and back again with the same rate, they must have the same equilibrium occupation; therefore, the probability of finding the system in configuration I and the probability of finding it in configuration II must be equal, otherwise the system would violate detailed balance (which the model which we are assuming the system obeys in $(n - 1)$ -d satisfies). However, there is another way to go from state I to state II: we can move the central particle, which we will say occurs with rates λ_1 and λ_2 respectively. Once the central particle is moved, we now have a “gas” of free particles, which we can once again move as we like using only moves of rate 1, in order to deform the system into configuration II. As the probability of our system being in state II is the same as it being in state I, the only way detailed balance can be obeyed is if $\lambda_1 = \lambda_2$. Therefore, the rate at which a particle moves into an adjacent empty space cannot depend upon the configuration of its adjacent particles in a given $(n - 1)$ -dimensional hyperplane, only their number.

Now we need to consider two cases, as the slot directly behind the central particle’s proposed direction of motion can be either empty or full. Firstly, the empty case is considered in Fig. 2.12. This time, we are highlighting the fact that if we move the central particle out of a hyperplane configuration of m particles, which occurs with rate u_m , this results in a gas of free particles; equivalently we could’ve produced a gas by moving the adjacent particles one by one as before, which requires m steps with each with rate λ . As the two gases are equivalent, in detailed balance terms, they must have the same realisation probability. If the probability of our being in the initial configuration (top left) was p , then by detailed balance the probability of our being in a free particle state is simultaneously both pu_m and $p\lambda^m$, and so $pu_m = p\lambda^m$ implying that

$$\lambda^m = u_m. \quad (2.50)$$

Figure 2.12 Here we have used the same diagram rules as in Fig. 2.11.

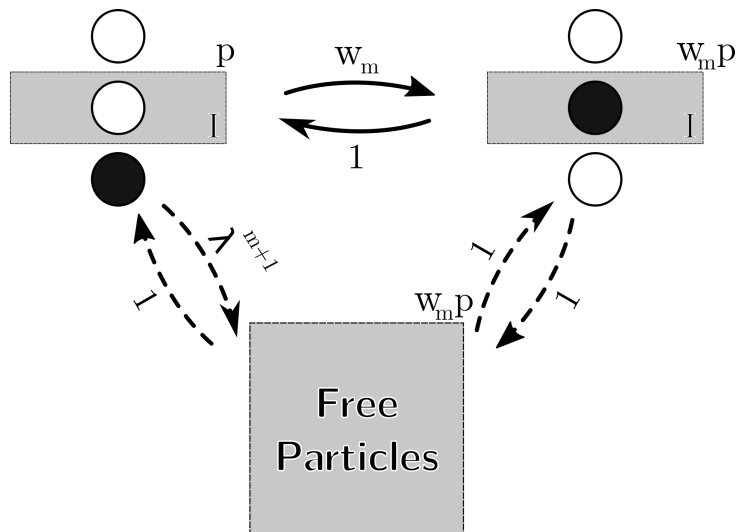


In Fig. 2.13, we show exactly the same thing, only this time there is a particle behind the central particle, and so an additional move must be made in order to create a gas of free particles. This means that the equivalence is now between $p u_m$ and $p \lambda^{m+1}$, and so

$$\lambda^{m+1} = w_m. \quad (2.51)$$

With the constraints that detailed balance imposes upon u_m and w_m , we find that the original proposition for dimension n is true so long as it is for dimension $(n - 1)$ for $n > 1$, and as we know it is true for $n = 1$, the theorem is proved.

Figure 2.13 As Fig. 2.12, but now with a particle behind the central one.



□

Theorem 1 implies that an n -dimensional exclusion model which is symmetric, local and obeys detailed balance must have an energy (defining the equilibrium distribution) which is proportional to the number of particle-particle adjacencies in the system; this therefore limits energy to being contained in the “bond” between adjacent particles, leaving us only with the option of a simple additive bond energy. This means that in order to have a more complicated energy, our only option is to either break symmetry or have a system of rates which considers more than the immediate environment of a particle which is attempting to move, for example considering the environment to which the particle is going.

The advantage of possessing this result is that it highlights that in n -dimensions there is again a special, simple one-parameter model which has many symmetry properties and is therefore a good first target for study. As such, we will perform a mean-field analysis of the n -dimensional SPM, to give us analytical results to compare to later Monte-Carlo numerics.

2.4.2 MFT of the n -Dimensional SPM

In the same manner as in Sec. 2.3.1, we will let $\rho_\chi(t)$ be the mean occupation of the χ^{th} site at time t , where $\chi \in \mathbb{Z}^n$. Let the unit vector in the i^{th} direction be $e_i \in \mathbb{Z}^n$, so that $\rho_{\chi+e_i}$ refers to a lattice site adjacent to the χ^{th} and offset in the i^{th} direction. Then, making the normal MFT assumption (that means of products are products of means), we can say that the rate at which a particle moves from site χ to site $\chi + e_i$ is

$$\begin{aligned} \sigma_{\chi \rightarrow \chi + e_i} &= \rho_\chi (1 - \rho_{\chi + e_i}) [(1 - \rho_{\chi - e_i}) + \lambda \rho_{\chi - e_i}] \\ &\times \prod_{j \neq i}^n [(1 - \rho_{\chi + e_j}) (1 - \rho_{\chi - e_j}) + \lambda \rho_{\chi + e_j} (1 - \rho_{\chi - e_j}) + \lambda \rho_{\chi - e_j} (1 - \rho_{\chi + e_j}) + \lambda^2 \rho_{\chi + e_j} \rho_{\chi - e_j}] \\ &= \rho_\chi (1 - \rho_{\chi + e_i}) [1 - \zeta \rho_{\chi - e_i}] \prod_{j \neq i}^n [(1 - \zeta \rho_{\chi - e_j}) (1 - \zeta \rho_{\chi + e_j})], \end{aligned} \tag{2.52}$$

with $\zeta = 1 - \lambda$ as usual.

Again, we will move to a continuum formulation. To do this, we are best off considering the overall flow between the site at χ and the site at $\chi + e_i$, and then Taylor expanding $\rho(\mathbf{x}, t)$ as a continuous variable. Doing this analytically

Table 2.1 The MFT current in the SPM, as a function of the density gradient, for the first 4 dimensions.

n	Simplified Current, $-\mathbf{J} \frac{\tau_0}{a^2}$
1	$[1 - \zeta\rho(4 - 3\rho)] \nabla\rho$
2	$(1 - \zeta\rho)^2 [1 - \zeta\rho(6 - 5\rho)] \nabla\rho$
3	$(1 - \zeta\rho)^4 [1 - \zeta\rho(8 - 7\rho)] \nabla\rho$
4	$(1 - \zeta\rho)^6 [1 - \zeta\rho(10 - 9\rho)] \nabla\rho$

in arbitrary dimensions is extremely tedious, and more importantly error-prone; thus, computer assistance is useful. Discussion of a code which calculates this MFT current for given n to $\mathcal{O}(a^3)$ may be found in Sec. A.2.

Computing this current for a few low values of n , a pattern emerges, as one can see in Tab. 2.1. Spotting the pattern in n , one can see that the MFT current in n -dimensions is

$$\mathbf{J} = -\frac{a^2}{\tau_0} (1 - \zeta\rho)^{2(n-1)} [1 - \zeta\rho((2n+2) - (2n+1)\rho)] \nabla\rho, \quad (2.53)$$

where the current and density obey the usual continuity equation

$$\frac{\partial\rho}{\partial t} + \nabla \cdot \mathbf{J} = 0 \quad (2.54)$$

with $\mathbf{J} = -D(\rho)\nabla\rho$, D being the diffusion coefficient

$$D(\rho) = \frac{a^2}{\tau_0} (1 - \zeta\rho)^{2(n-1)} [1 - \zeta\rho((2n+2) - (2n+1)\rho)]. \quad (2.55)$$

The equivalent of our 1-dimensional steady state solution may be found by considering a flow from one hyperplane to a parallel one a distance L away. Taking the planes to be separated in the x direction, we find that we have an equivalent solution, where the homogeneous current J_0 is given by

$$J_0 = \int_{\rho_L}^{\rho_0} d\rho \frac{a^2}{L\tau_0} (1 - \zeta\rho)^{2(n-1)} [1 - \zeta\rho((2n+2) - (2n+1)\rho)], \quad (2.56)$$

where ρ_0 and ρ_L are as usual the densities on the bounding hyperplanes. The

density profile is the implicit solution of

$$\int_{\rho}^{\rho_0} d\rho \frac{a^2}{\tau_0} (1 - \zeta\rho)^{2(n-1)} [1 - \zeta\rho((2n+2) - (2n+1)\rho)] = J_0 x. \quad (2.57)$$

The rest of the boundary conditions can be pretty arbitrary. The domain might extend infinitely parallel to the hyperplanes, or could be finite, or on a periodic domain; whichever types of boundary are used, the boundary density must be chosen to match the density specified by the homogeneous solution there.

Limiting and Symmetry Properties of the n -Dimensional MFT

Now that we have derived the diffusion coefficient D in the n -dimensional MFT, we can investigate some special cases, in a similar manner to the 1D situation.

As $\rho \rightarrow 0$, $D \rightarrow 1$, which makes sense as in extremely low-density situations the particles do not interact. As $\rho \rightarrow 1$, $D \rightarrow \lambda^{2(n-1)} \frac{a^2}{\tau_0}$, which again corresponds to the diffusion of vacancies in an almost-full lattice (which depends upon almost fully-bound particles needing to jump in order for a vacancy to move).

When $\lambda \rightarrow 1$, we find that $D \rightarrow \frac{a^2}{\tau_0}$, which makes perfect sense as turning off the interactions gives us normal diffusion again. As $\lambda \rightarrow 0$,

$$D(\rho) \rightarrow (1 - \rho)^{2(n-1)} [1 - (2n+1)\rho], \quad (2.58)$$

suggesting that in that limit negative diffusion occurs at densities higher than $\frac{1}{2n+1}$. In terms of the behaviour for very large λ , one can show that

$$D(\rho) = \lambda^{2n-1} \rho^{2(n-1)} [(2n+1)\rho - (2n+2)] + \mathcal{O}(\lambda^{2(n-1)}), \quad (2.59)$$

so we should expect to see currents of $\mathcal{O}(\lambda^{2n-1})$ for large λ in arbitrary dimensions. Of course, the number of sites adjacent to a particle attempting to move into an adjacent vacancy is $2n-1$, so in the large λ limit $\mathcal{O}(\lambda^{2n-1})$ is the biggest speedup we could reasonably expect to see, and the MFT reflects that.

Unlike the 1D situation, there is no longer a symmetry in the density dependence of the diffusion coefficient. This is because the $(1 - \zeta\rho)^{2(n-1)}$ bracket is symmetric about $\rho = \zeta^{-1}$, whereas the $[1 - \zeta\rho((2n+2) - (2n+1)\rho)]$ bracket's symmetry is about $\rho = \frac{n+1}{2n+1}$; thus, in general they would not share a point of symmetry, and so their product would not be symmetric.

Finding the density at which flow is extremal is annoying, but doable. Differentiating the diffusion coefficient with respect to ρ gives, after factorising,

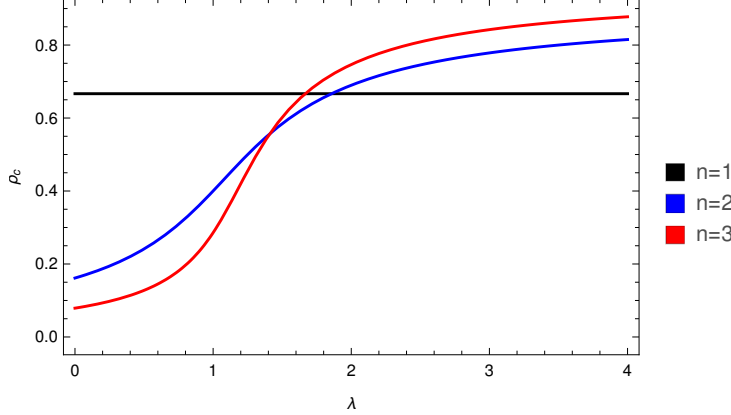
$$\frac{\partial D}{\partial \rho} = -2\zeta(1 - \zeta\rho)^{2n-3} [\zeta\rho(n(2n+1)(\rho-1) + 1) - 2n(\rho-1) - \rho]. \quad (2.60)$$

The first bracket has its zero when $\rho = \zeta^{-1}$, which means that this only causes a turning point for allowed ρ when $\zeta > 1 \implies \lambda < 0$, which is unphysical. The second bracket is a quadratic in ρ . Its root, and therefore the extremal value, occurs at ρ_c where

$$\rho_c = \frac{4}{2\zeta n^2 + (3 - \lambda)n + \lambda + \sqrt{(2\zeta n^2 + (3 - \lambda)n + \lambda)^2 - 8\zeta n(2n+1)}}. \quad (2.61)$$

The extremum is a minimum for $\lambda < 1$ and a maximum for $\lambda > 1$. The variation of ρ_c with λ is shown in Fig. 2.14. In terms of interpretation, this extremum determines where maximal flow occurs for $\lambda > 1$. As $\lambda \rightarrow \infty$, $\rho_c \rightarrow \frac{4n^2+2n-2}{2n(1+2n)}$, which approaches 1 as the number of dimensions becomes very large.

Figure 2.14 The variation of ρ_c , for which flow is extremal, as a function of λ , for $n = \{1, 2, 3\}$. Notice that it starts low and ends high in the 2 and 3-dimensional cases, but is constant in the 1D case.



In all numbers of dimensions, the SPM MFT can produce negative flows. To find out which conditions are required for this, we must solve $D(\rho) = 0$ for $\rho \in (0, 1)$. Luckily we already have D in a factorised form in Eq. (2.55). Assuming $\zeta < 1$, the first bracket cannot have a solution on $(0, 1)$, therefore we seek the zeros of the second bracket. The discriminant of the quadratic in the second bracket is

$$\zeta^2(2n+2)^2 - 4\zeta(2n+1), \quad (2.62)$$

thus the crossover between the existence and nonexistence of real solutions to $D(\rho) = 0$ occurs when $\zeta = \frac{2n+1}{(n+1)^2}$. Using our result for the dependence of ρ_c upon λ (Eq. (2.61)), we see that as we reduce λ from 1, backwards diffusion first occurs for

$$\rho_c = \frac{4(n+1)}{(n+1)(6n-3) + 3 + (2n+1)\sqrt{n(9n-8)}} \quad (2.63)$$

As we have seen, this “gap” of negative diffusion begins at $\rho_c = \frac{2}{3}$ in 1D, and then at $\rho_c \sim 0.22$ in 2D and $\rho_c \sim 0.13$ in 3D.

The SPM MFT in 2-Dimensions

Specifically, in the 2-dimensional case, J_0 is given by

$$J_0 = \frac{a^2}{L\tau_0} \left[\zeta^3 (\rho_0^5 - \rho_L^5) + \frac{1}{2} \zeta^2 (3\zeta + 5) (\rho_L^4 - \rho_0^4) + \frac{1}{3} \zeta (13\zeta + 5) (\rho_0^3 - \rho_L^3) + 4\zeta (\rho_L^2 - \rho_0^2) + (\rho_0 - \rho_L) \right]. \quad (2.64)$$

Note that Fick’s Law (that the current should be proportional to the difference between the concentrations at the boundaries) does not hold. The dependence of flow upon the boundary conditions for some given λ is shown in Fig. 2.15, and the dependence of flow upon λ for some fixed boundaries is shown in Fig. 2.16. We can use these in comparison with our Monte-Carlo data in 2-dimensions.

2.5 Conclusions About the SPM MFT

In this Chapter we have derived a whole host of results about the continuum limit Mean-Field Theory of the Sticky Particle Model defined in arbitrary dimensions. The key things to take away from it are:

- Thm. 1 shows us that the n -dimensional SPM (as defined within it) is the only model defined on an n -dimensional square lattice which is symmetric, local and obeys detailed balance.
- The MFT of this model **always** predicts a transition in which the diffusion coefficient becomes negative for some physically-allowed ρ and λ , regardless of dimension.

Figure 2.15 Plots of the flow in the MFT of the 2-dimensional SPM, where we are varying the boundary densities. The values of λ used are $\{0.2, 0.4, 0.75, 2\}$, going clockwise from top left.

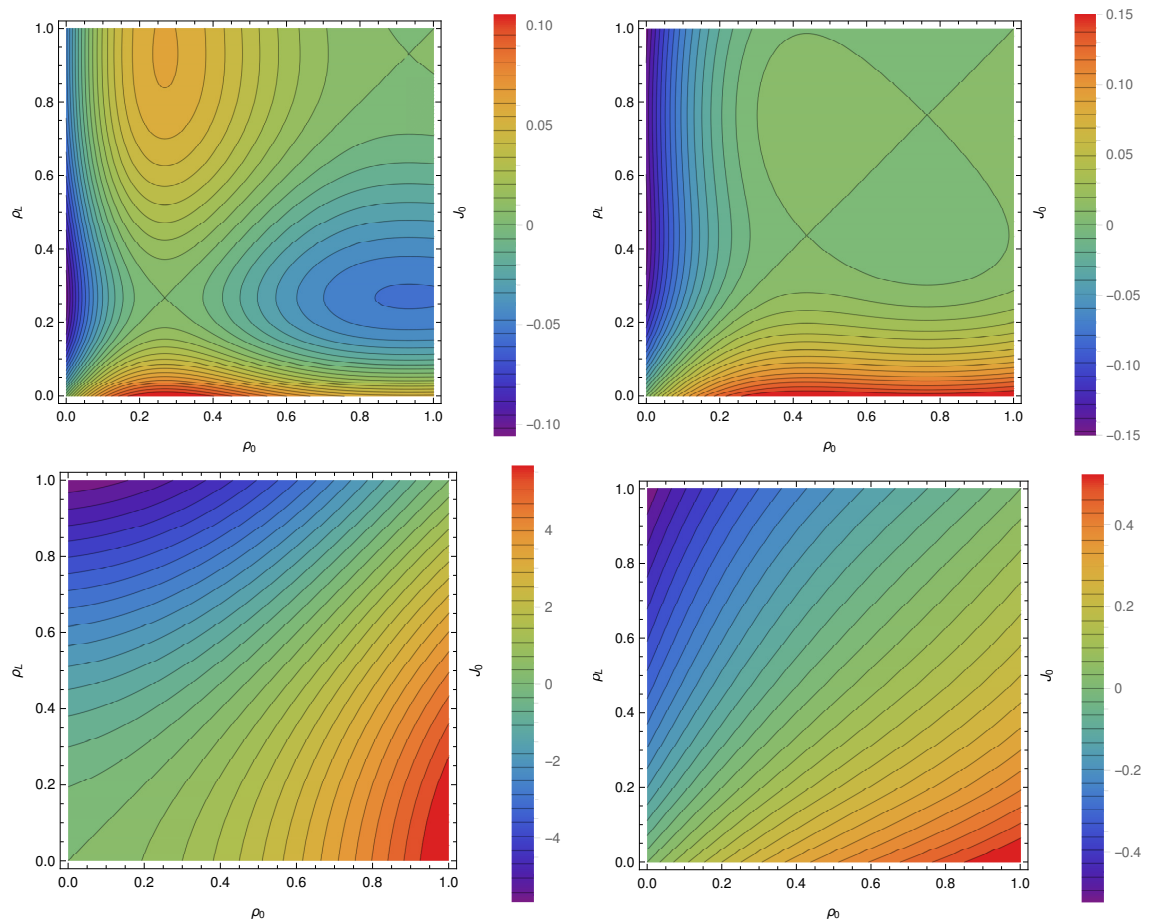
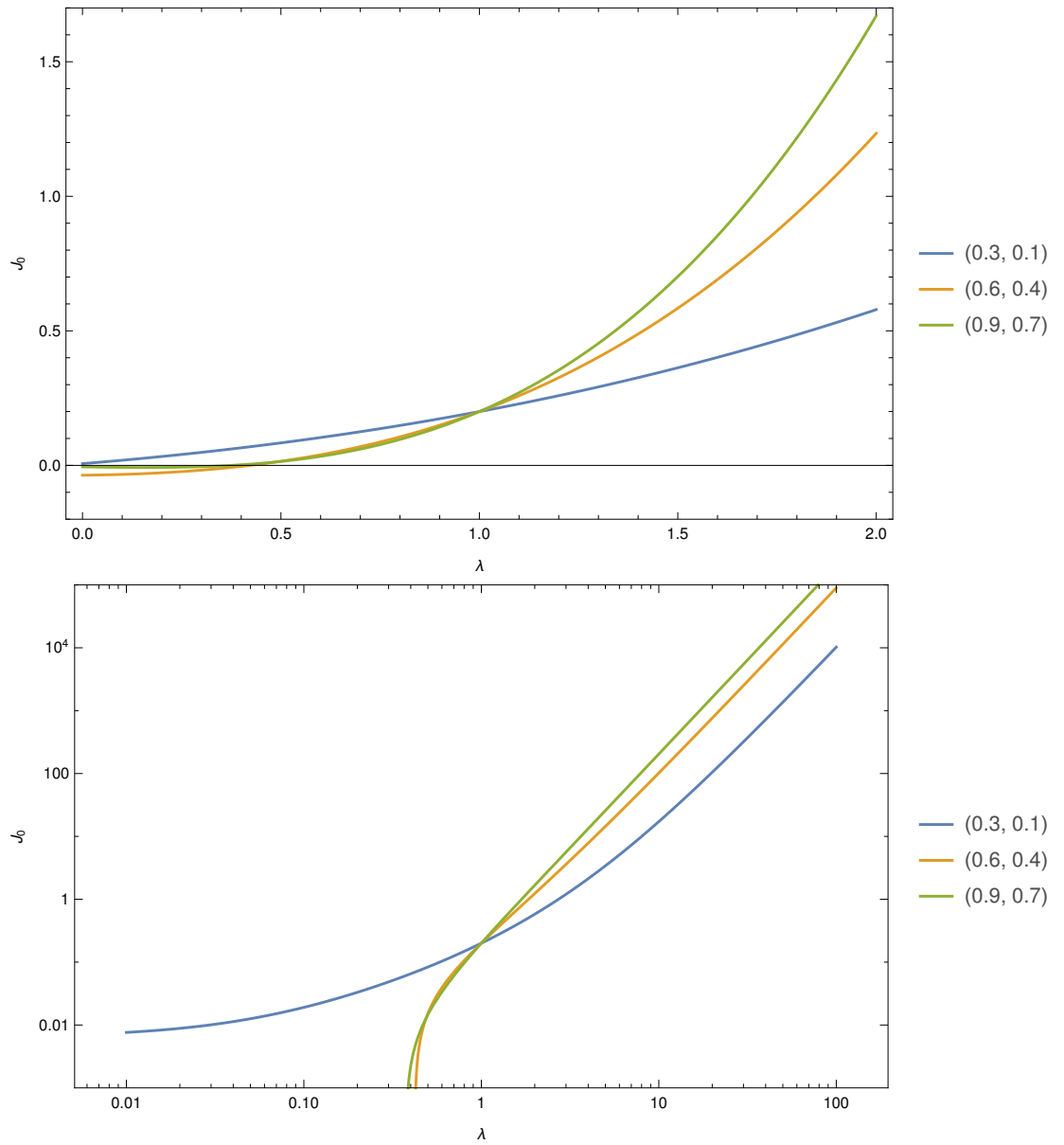


Figure 2.16 Plots of the current variation with respect to λ in the MFT of the 2-dimensional SPM. Boundary conditions are labelled in the legend in the form (ρ_0, ρ_L) .



- Currents for very large λ should scale as λ^{2m-1}

Chapter 3

Transition Rate Matrix Analysis

Now that we have MFT predictions about the relationship between density difference and current in the SPM, it would be good to try to investigate their validity. In Chapter 4 we will use Monte-Carlo methods to do this in 1D and 2D, but in this chapter we will restrict our attention to 1D.

3.1 The Transition Rate Operator for the SPM

The SPM is an autonomous continuous-time Markov Process, which describes continual transitions between states with transition rates depending only upon the current state. As such, if we call the total space of states Ξ then the probability distribution $P : \Xi \times \mathbb{R} \rightarrow \mathbb{R}$ should obey a **master equation**

$$\frac{\partial P(\xi, t)}{\partial t} = \mathcal{A}P(\xi, t), \quad (3.1)$$

where $\mathcal{A} : \Xi \rightarrow \Xi$ is the **transition rate operator** or TRO. Note that I am going to be using column vectors for probabilities rather than row vectors, as many in the probability community do. Parametrising \mathcal{A} via

$$(\mathcal{A}f)(u) = \int_{\Xi} d\xi \sigma(u, \xi) f(\xi) \quad (3.2)$$

puts it in a more familiar, transport equation-style notation:

$$\frac{\partial P(\xi, t)}{\partial t} = \int_{\Xi} du \sigma(\xi, u) P(u, t). \quad (3.3)$$

Here $f : \Xi \rightarrow \mathbb{R}$ is an arbitrary function, intended to be a probability distribution (nonnegative, unit measure, etc), whilst $\xi, u \in \Xi$ are dummy variables and $\sigma : \Xi \times \Xi \rightarrow \mathbb{R}$ represents \mathcal{A} in the basis determined by how we perform the integration.

We demand that σ satisfies

$$\forall \xi \in \Xi, \sigma(\xi, \xi) \leq 0 \quad (3.4)$$

and

$$\forall \xi_1, \xi_2 \in \Xi : \xi_1 \neq \xi_2, \sigma(\xi_1, \xi_2) \geq 0, \quad (3.5)$$

as well as the constraint

$$\forall u \in \Xi, \int_{\Xi} d\xi \sigma(\xi, u) = 0. \quad (3.6)$$

The last constraint implies that

$$\int_{\Xi} d\xi \frac{\partial P(\xi, t)}{\partial t} = \int_{\Xi} du P(u, t) \left[\int_{\Xi} d\xi \sigma(\xi, u) \right] = 0 \quad (3.7)$$

regardless of the structure of P , which is our probability conservation equation.

The formal (forward-time) solution to Eq. (3.1) is given by

$$P(\xi, t) = e^{(t-t_0)\mathcal{A}} P_0, \quad (3.8)$$

where t_0 is some initial time, P_0 is the starting distribution, and the operator exponential is defined by its Taylor expansion, which should converge fine for bounded \mathcal{A} , satisfied for the finite-system SPM. As $e^{(t-t_0)\mathcal{A}}$ and \mathcal{A} share eigenvectors, we see that the eigenstructure of \mathcal{A} is something well worth investigating, as it should give us information about the time-evolution of the system. An important thing to point out is that \mathcal{A} does not in general have orthogonal eigenvectors because it is not in general symmetric, and so we cannot normally diagonalise it using orthogonal transformations. This means that modes do not “decouple” in the way that states do in the Schrödinger equation, and we instead have to deal with an **adjoint system** [52].

Luckily, when it comes to the analysis of steady states, there are a few results that can help us. If we consider the operator $\mathcal{G}_T = e^{T\mathcal{A}}$ (in other words, the **propagator** for a period of time T), it is pretty easy to see that this is a standard Markov Operator, as we are essentially reversing the limiting process we would

perform in order to define a continuous time Markov process as a limit of a discrete time one. If we assume that Ξ is finite and \mathcal{G}_T is irreducible then as a Markov operator it must possess a unique eigenvector with corresponding eigenvalue 1. All other eigenvalues must have modulus between 0 and 1. Therefore, \mathcal{A} must share that same unique eigenvector with associated eigenvalue 0, and its other eigenvalues must have negative real part. In physical terms, the system must have a single steady state probability distribution, which it always relaxes towards exponentially quickly, with a rate determined by the nonzero eigenvalue of \mathcal{A} with real part closest to 0.

Of course, for such finite-state systems (such as the SPM on a finite domain) the integrals become sums, and σ a matrix, Q . In such systems, we can arrange to have some labelling scheme which uniquely relates system states to natural numbers, and therefore relates states to basis vectors in a vector space. In the SPM, a site is either full or empty, which means that there is a natural mapping between states and natural numbers based upon binary representation; a string of 1s and 0s can be associated with a natural number as well as a configuration of particles and vacancies.

3.1.1 A Small Worked Example: Closed System

As a concrete example, let us consider the SPM on a cyclic domain of length 3. There are 2^3 possible combinations, and so 8 possible states: 000, 001, and so forth. The transition rate matrix describing this system is:

$$Q = \begin{bmatrix} 0 & & & & & & & \\ -2 & 1 & & & & & & \\ 1 & -2 & 1 & & & & & \\ & & -2\lambda & \lambda & \lambda & & & \\ 1 & 1 & & -2 & & & & \\ & & \lambda & -2\lambda & \lambda & & & \\ & & \lambda & \lambda & -2\lambda & & & \\ & & & & & & & 0 \end{bmatrix}, \quad (3.9)$$

where we have omitted most of the zero entries for clarity. An alert observer will note that Q is reducible, and so by permuting the basis vectors we can rearrange

the matrix into block form:

$$Q' = \begin{bmatrix} -2 & 1 & 1 \\ 1 & -2 & 1 \\ 1 & 1 & -2 \\ & -2\lambda & \lambda & \lambda \\ & \lambda & -2\lambda & \lambda \\ & \lambda & -2\lambda & \lambda \\ & & & 0 \\ & & & 0 \end{bmatrix}. \quad (3.10)$$

According to our recipe, to learn about the solutions to Eq. (3.1) in this case, we need to know about the eigendecomposition of Q . The block structure of Q' means that there are 4 distinct parts of the state space, between which there are no transitions; this partitioning corresponds to the fact that particle number is conserved on the ring. Two of these sectors correspond to the full and empty states, and their dynamics are completely trivial, in the sense that the state space is 1D and there are no dynamics, as the particles/vacancies have nowhere to go. The remaining sectors correspond to the situation where there is one particle or one vacancy. The matrix is symmetric, meaning that its eigenvalues are real, and we find that both nontrivial blocks can be diagonalised to form a multiple of

$$\begin{bmatrix} 0 & & \\ & -3 & \\ & & -3 \end{bmatrix}, \quad (3.11)$$

with eigenvectors $[1, 1, 1]^T$, $[-1, 0, 1]^T$ and $[-1, 1, 0]^T$ respectively, the latter two forming a degenerate eigenspace.

In this particular example then, we find that there 4 steady states:

- All slots full,
- All slots empty,
- One particle present, with equal chance to be in any particular position,
- The same but with a vacancy instead of a particle.

Whilst the first 2 cases are trivial (one-dimensional probability spaces), in the other two cases we relax towards the steady state with rates 3 and 3λ respectively.

In this example, the TRM was actually symmetric, and so all the eigenvalues were real. It was also highly reducible, due to the strict constraints imposed by the particle conservation law. When we have boundary conditions which permit the creation and destruction of particles, that will change; we will consider that situation now.

3.2 Forming the TRM for Systems with Dirichlet Boundary Conditions

3.2.1 Dirichlet Boundary Conditions

In Ch. 2 we made an MFT for the SPM in 1-dimension, and when investigating steady states used Dirichlet boundary conditions when we needed them. In particular, we had a system of length L and sought solutions in which the system density was pinned at ρ_0 at $x = 0$ and ρ_L at $x = L$.

We would like to do a similar thing for the non-MFT SPM. An exact analogue of the situation does not exist, as occupation number is not defined *a priori* in a Markov process, but merely emerges as a result of the rates prescribed. The closest imitation to it we can get is by allowing particles to be created and destroyed in boundary regions at either end of a chain, and then try to set these rates so that the time-averaged occupation probability in the end sites are ρ_0 and ρ_L respectively. Note that this is a little more involved than simply loading and unloading particles as one does in ASEP, as

- loading and unloading really doesn't simulate the boundary condition we are looking for, which is attachment to a particle reservoir of constant particle density, and
- we actually need to consider a two-site boundary layer attached to each end, because the internal dynamics of the particles depend upon their immediate environment.

To simulate a boundary which is attached to a reservoir with occupation ρ , we allow particles to appear in empty boundary sites with rate $B_0\sqrt{\frac{\rho}{1-\rho}}$ and to disappear from full ones with rate $B_0\sqrt{\frac{1-\rho}{\rho}}$, for some positive B_0 . If we switch off

all other dynamics and consider this in isolation, we would have a collection of decoupled two-state systems. Writing a TRM for this with the first basis vector being the empty state and the second the full one, we get

$$Q = \begin{bmatrix} -B_0\sqrt{\frac{\rho}{1-\rho}} & B_0\sqrt{\frac{1-\rho}{\rho}} \\ B_0\sqrt{\frac{\rho}{1-\rho}} & -B_0\sqrt{\frac{1-\rho}{\rho}} \end{bmatrix}. \quad (3.12)$$

There is of course a zero eigenvalue, which corresponds to a stationary distribution $[1 - \rho, \rho]^T$, precisely as desired.

In order to simulate attaching a reservoir with particle density ρ , we apply the creation and annihilation rates above to the outermost two sites in our lattice. The outermost site only performs these operations. The inner boundary site undergoes these creation and annihilation processes, as well as the normal dynamics of the SPM; thus, particles will move in and out of it as normal, and when the outermost site's occupation is required to determine the transition rate for a particle moving inward, that information is available. One could possibly eliminate the need for the outermost boundary site by averaging over occupations, however we have chosen not to do this for consistency with our Monte-Carlo calculations in Ch. 4.

Observant readers will notice that by using these creation and annihilation rates we are left with a free variable, B_0 . This controls the ratio of the creation and annihilation rates to the internal dynamical rates 1 and λ . In general when we're trying to simulate an adjacent reservoir we want the boundary motion to be “fast” compared to the internal dynamics, and so B_0 may be regarded as a regularisation parameter; any choice of B_0 should be good so long as the creation and annihilation rates sufficiently dominate both 1 and λ . In practise, in our larger-scale calculations we used

$$B_0 = b(1 + \lambda), \quad (3.13)$$

with b set to, 100 or 1000.

3.2.2 Another Worked Example: Open System

Using full boundary conditions, the smallest system we can consider consists of adjacent boundary layers, in which particles pass directly from the inner layer of

one boundary to the inner layer of the other boundary. Unfortunately the state space of such a system is $2^4 = 16$ -dimensional, and so it would be cumbersome to consider such a system as an example here.

However, in the special case in which one boundary has density $\rho_0 = 1$ and the other has $\rho_L = 0$, the outer boundary layers become nondynamical, and the system simplifies considerably; particles can only enter at the full end with rate λ , and can only leave at the empty end. Therefore, we can consider a system consisting of single boundary layers attached to a single internal slot without needing to consider a state space larger than $2^3 = 8$. Using the same state-labelling convention as in Sec. 3.1.1, the TRM for this new open system is

$$Q = \begin{bmatrix} -\lambda & 1 & & & & & \\ & -\lambda - 2 & 1 & & & & \\ & & 1 & -\lambda - 2 & 1 & \lambda & \\ & & & & -2\lambda - 1 & \lambda & \\ \lambda & & & 1 & & -\lambda & 1 \\ & \lambda & & & \lambda & & -\lambda - 2 & \lambda \\ & & \lambda & & & & 1 & -\lambda & \lambda \\ & & & \lambda & & & & & -\lambda \end{bmatrix}. \quad (3.14)$$

This time the matrix is not symmetric, and there does not exist a basis permutation which puts the TRM into block form. If we calculate the characteristic polynomial $p(q) = |Q - qI|$, we find that

$$\begin{aligned} p(q) = q & [q^7 + (9\lambda + 7)q^6 + (34\lambda^2 + 53\lambda + 17)q^5 + (71\lambda^3 + 165\lambda^2 + 103\lambda + 17)q^4 + \\ & + (89\lambda^4 + 274\lambda^3 + 247\lambda^2 + 76\lambda + 6)q^3 + (67\lambda^5 + 256\lambda^4 + 294\lambda^3 + 126\lambda^2 + 17\lambda)q^2 + \\ & + (28\lambda^6 + 127\lambda^5 + 171\lambda^4 + 91\lambda^3 + 15\lambda^2)]q + (5\lambda^7 + 26\lambda^6 + 37\lambda^5 + 24\lambda^4 + 4\lambda^3). \end{aligned} \quad (3.15)$$

Of course, the roots of $p(q)$ are the eigenvalues of Q . Clearly one of the eigenvalues is $q = 0$, and the others could be found by finding the root of the 7th order polynomial, which we will not be doing analytically because it is extremely tedious and besides the point of this example. The 0-eigenvector, and therefore the steady-state probability distribution over the possible configurations, can be

computed with a little care, and turns out to be

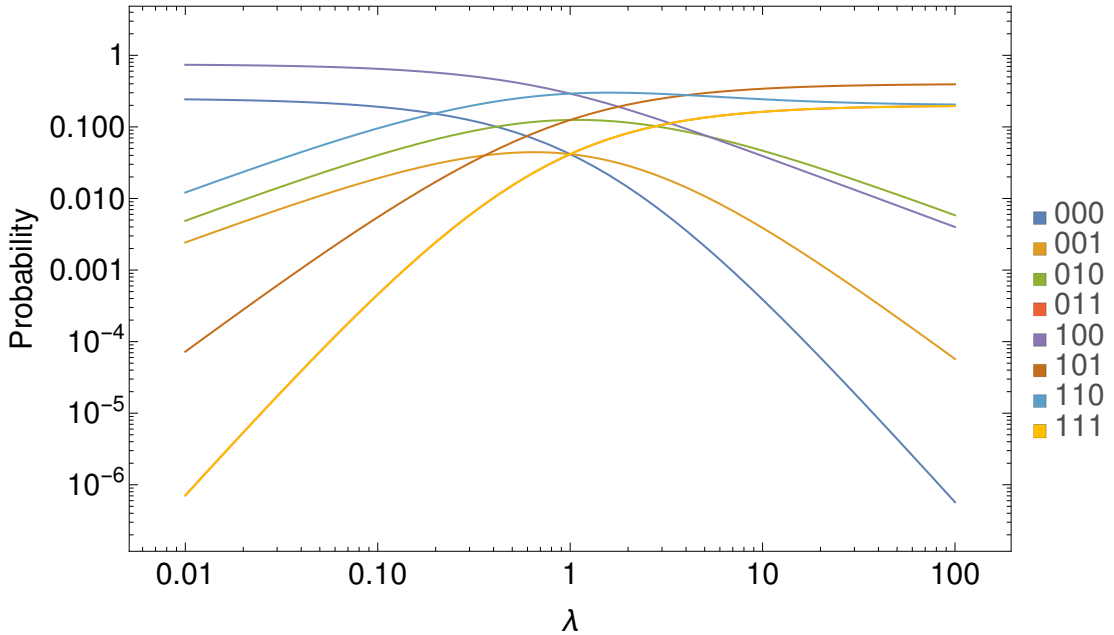
$$q_0 = D^{-1} \begin{bmatrix} 3\lambda + 1 \\ \lambda(3\lambda + 1) \\ \lambda(\lambda + 2)(3\lambda + 1) \\ \lambda^3(\lambda + 3) \\ (\lambda + 3)(2\lambda(\lambda + 2) + 1) \\ \lambda^2(\lambda + 3)(2\lambda + 1) \\ \lambda(\lambda(\lambda + 8) + 14) + 5 \\ \lambda^3(\lambda + 3) \end{bmatrix}, \quad (3.16)$$

where

$$D = \lambda [\lambda(\lambda[5\lambda + 26] + 37) + 24] + 4. \quad (3.17)$$

The variation of the occupation probabilities with λ is displayed in Fig. 3.1. Notice that at extremely small λ the system either empties or a single particle

Figure 3.1 *The variation of the steady-state configuration probability distribution with λ for our open system. The coloured curves correspond to specific configurations, as indicated in the legend.*



gets stuck to the full boundary, essentially preventing further flow by blocking it. Meanwhile, at large λ there are a few fairly popular states, the most dominant being one with alternating particles and vacancies, as one might expect. The steady-state current from left to right in this system can be calculated analytically

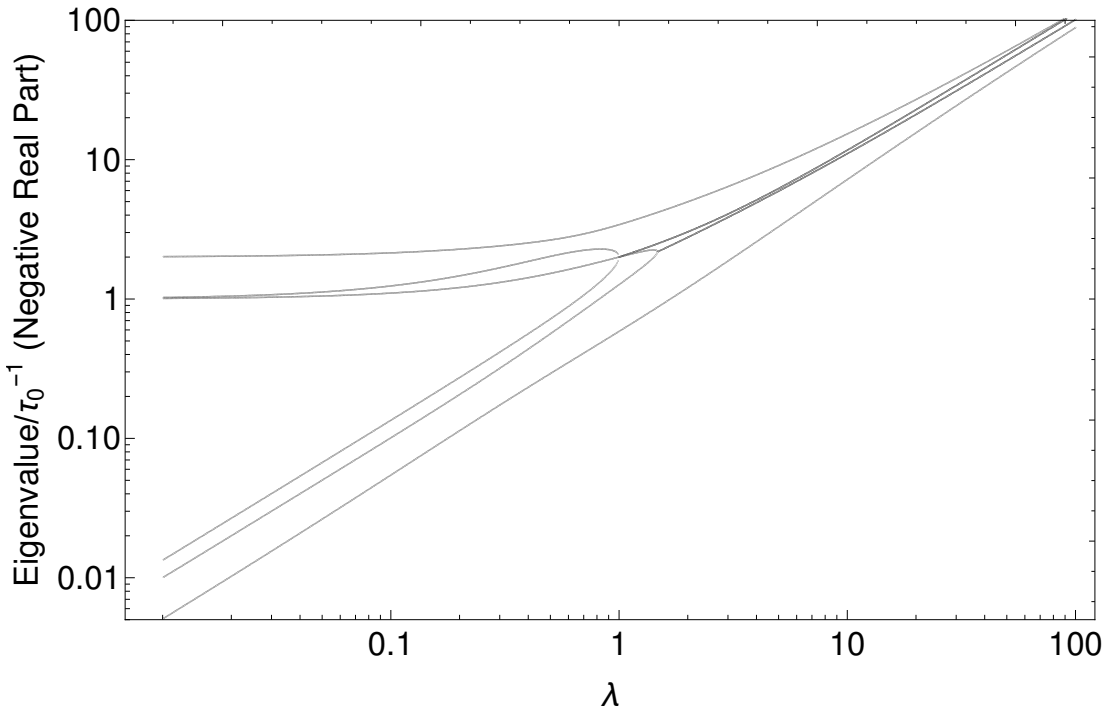
once we have the steady state probability distribution, and turns out to be

$$J = \lambda \left[\frac{1}{4} + \frac{(1-\lambda)(3+\lambda)\lambda^2}{4 + \lambda(24 + \lambda[37 + \lambda(26+5)])} \right]. \quad (3.18)$$

The second term in the bracket is generally dominated by the first, so we can say to an excellent approximation that $J \sim \frac{1}{4}\lambda$. Thus, at least for this tiny example with very extreme boundary conditions, there does not appear to be any change in the scaling of the current with λ .

We can also compute the eigenspectrum of the TRM for this small system; this is displayed in Fig. 3.2. It is in many ways rather similar to the eigenspectra we

Figure 3.2 *The variation of the eigenspectrum of the TRM for our small open system with λ . Here we have plotted $-\Re\lambda$, as λ is expected to be a complex number with negative real part.*



find for larger systems, so see Sec. 3.3.2 for our comments on those.

3.2.3 Construction of the TRM in Sparse Format

As we have seen, it is possible to find the eigendecomposition of the TRM analytically for extremely small systems with special boundary conditions.

However, we'd really like to see what happens for somewhat larger systems, with more diverse boundary conditions. Thus, let us try to develop a method for the numerical analysis of TRMs of arbitrary size.

The important thing to note about transition rate matrices for local lattice models such as the SPM is that whilst the TRM itself grows very aggressively with system size, the TRM is generally extremely sparse. The state space dimension grows as 2^L , and the TRM dimension therefore grows as $2^L \times 2^L$. However, a state containing N particles only has transitions to

- states which differ from the current state by one particle move, of which there are $\mathcal{O}(N)$, and
- states which differ from the current state by a single particle creation or annihilation, of which there are $\mathcal{O}(4)$.

Thus, as $N \leq L$ the number of nonzero entries in the matrix is $\mathcal{O}(2^L L)$, which is not a particularly tight bound. Therefore, the overall density of the TRM is $\mathcal{O}(2^{-L} L)$. Given that there already exist a great many efficient numerical routines for sparse linear algebra operations, there exists the possibility that we could use this to solve the SPM on a finite domain for small systems “exactly” (or at least, up to some nominated numerical tolerance).

To make use of this, we need to assemble the TRM in a suitable sparse format. I have written a Python code which does this. The script itself may be found in [20] at `codes/exact/matStuff/sparseSysRep.py`, but the gist of the algorithm is to simply run through all possible states, document all the transitions they can perform, and store the resulting entries in a sparse matrix element by element. During construction, the matrix should be stored in coordinate list format, i.e. a list of elements of the form (row, column, value), as this is trivial to update as we only inspect each matrix entry once. We can then convert the matrix to a compressed format such as CSC (**Compressed Sparse Column**) or CSR (**Compressed Sparse Row**). We used CSC, but in hindsight CSR would probably have been a better choice as it tends to make matrix-vector multiplication a little more efficient. Once we have the TRM in this format, it is ready for sparse linear algebra operations. Note that whilst these operations generally happen “in place”, this part of the process is the memory-intensive bit, as of course the memory usage scales with the number of nonzero matrix elements, which is $\mathcal{O}(2^L L)$. In terms of actual numbers, we found that 4Gb of

memory was more than adequate to solve a system of 16 sites in total. As the memory required to represent the TRM is the main limiting factor in this kind of calculation, if we were to attempt a larger calculation we would probably switch to using a machine with a very large working memory, such as DiRAC.

3.3 The Eigenspectrum of the TRM

3.3.1 The Computation of the TRM Eigenspectrum

Once we have the TRM Q in CSC or CSR format, we can then use sparse linear algebra. In our code we called the Python routine `scipy.sparse.linalg.eigs` upon it, which itself is a wrapper for C codes [35] which find eigenpairs according to desired criteria; precisely which algorithm to used is determined during runtime, and it may try different methods if it doesn't initially succeed.

In our computations, we typically performed two types of calculation. In the first we merely sought to find the steady state, so which we requested only the eigenvector x_0 associated to the eigenvalue q_0 with smallest absolute value, which should always be numerically zero. We requested that the eigenpair be found to a relative accuracy ϵ accuracy of 1 part in 10^{12} , which amounts to saying that

$$\frac{\|Qx_0 - q_0x_0\|}{\|x_0\|} \leq 10^{-12} = \epsilon \quad (3.19)$$

where $\|\cdot\|$ is some reasonable subordinate matrix norm (in our case, the 1 norm). Because we requested the eigenvalue closest to 0, `eigs` used the shift-invert method [43], leading to greater accuracy in the computation of eigenvalues near to 0 which is exactly what we wanted. For the other type of computation, we instead requested the k eigenpairs with largest real part, which most likely provoked the code to use a Implicitly Restarted Arnoldi Method (IRAM) [33, 34]. This is not as accurate for computing the steady state, but yields vastly more accurate results when computing the other eigenpairs compared to the first method.

3.3.2 The Structure of the TRM Eigenspectrum

Using our code (`codes/exact/matStuff/sparseSysRep.py` in [20]), we can compute the eigenspectrum of an SPM system with boundary densities connected

at both ends. Such a computation requires the following parameters to be specified:

- $\rho_0 \in (0, 1)$, the density of the reservoir connected to the left end of the domain.
- $\rho_L \in (0, 1)$, the density of the reservoir connected to the right end of the domain.
- $L \in \mathbb{N}$, the system size. The way we have defined things in the code, we do not count the two sets of two particles representing the boundary; thus, $L = 1$ actually refers to a system which contains 5 lattice sites, of which 4 are busy doing boundary duties.
- $b > 0$, the variable which controls the separation of timescales between the flickering motion on the boundaries and the internal motion within the bulk of the system. This should be set to something large, and compared to other values of it to ensure that it is working as a regularisation parameter (i.e. large changes to b have minimal impact on the relevant internal dynamics of the system, even if they have a great impact on the boundary dynamics).
- $\lambda > 0$, the internal anomalous movement rate in the SPM.
- ϵ , the relative accuracy the calculation aims for in the sense of Eq. (3.19).
- $1 \leq k < 2^{L+4}$, the number of eigenvalues to compute.

For consistency we kept L , b , ϵ and k constant during runs of calculations. This leaves ρ_0 , ρ_L and λ to be varied. In terms of what to vary and how to display the data, we decided to allow the spectrum to depend upon only one variable, and picked λ to be that variable. We generally chose $\rho_0 = 0.6$ and $\rho_L = 0.4$ in order to study a system in which, at least for $\lambda = 1$, the density is middling and a current flows. We then computed the resulting eigenspectrum in a couple different ways. First, we performed a relatively small calculation, in terms of the number of eigenvalues demanded and the number of λ used. We altered the values of L and b between runs, so that we can see what impact they have on the eigenspectrum. We then performed a very large calculation, in order to get a good look at the eigenstructure as a whole. In Ch. 2 our MFT suggested that a transition might occur around $\lambda = \frac{1}{4}$, so we should look out for odd behaviour in that regime.

To actually perform these TRM calculations, we used Edinburgh Compute and Data Facility’s Linux Compute Cluster, known as Eddie3. We will discuss this machine and its capabilities further in Chapter 4. Although we did initially consider the possibility of exploiting the natural parallelisability of the numerical linear algebra routines, we concluded that it was not probably not worthwhile in terms of computational gains, whilst requiring a lot of extra development time to implement. Instead, we simply submitted large numbers of separate serial jobs with different parameter values (e.g. for λ , ρ_0 , ρ_L) to Eddie3, and then allowed the machine to process them in its own time.

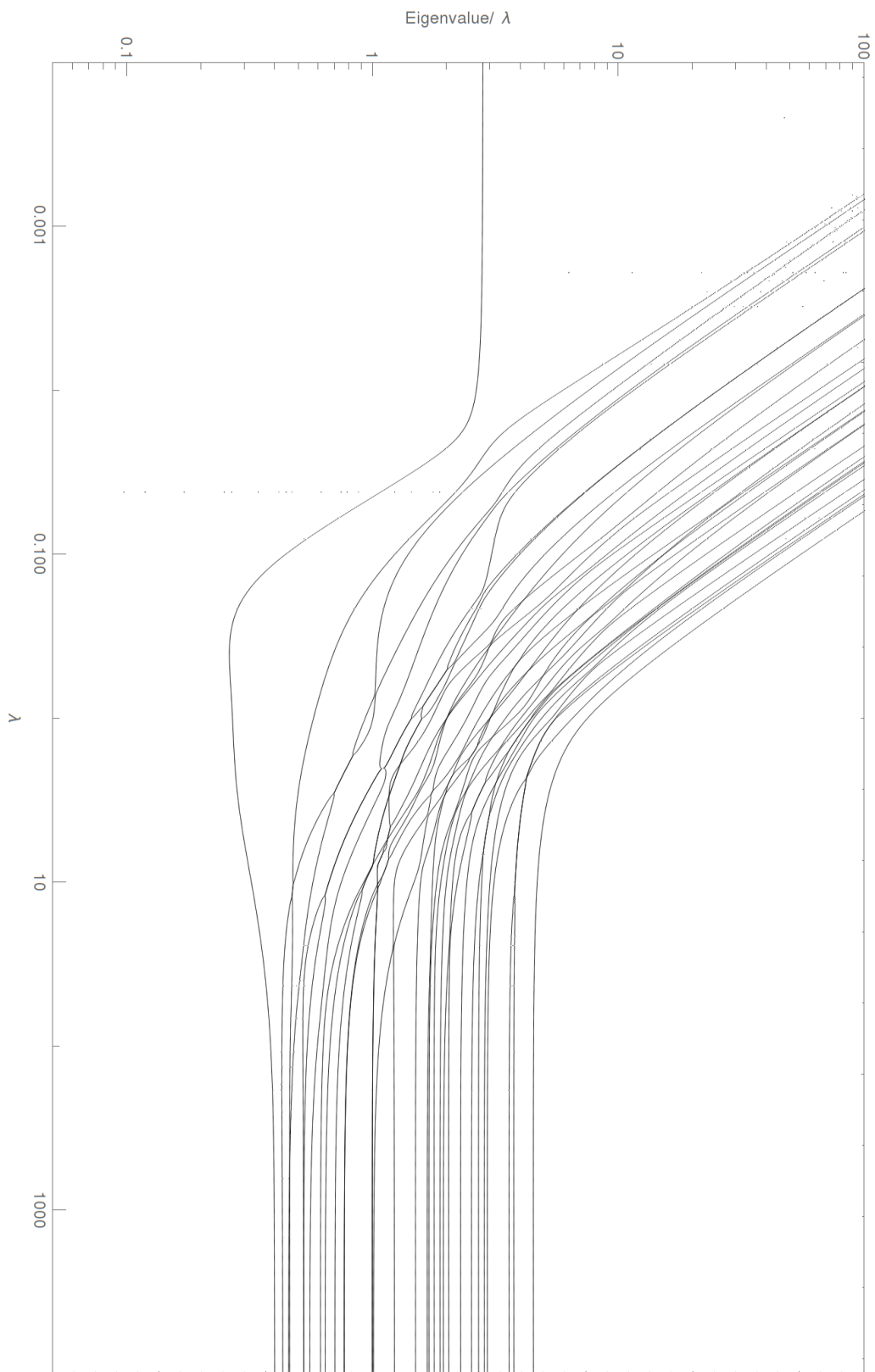
Small Calculations

First, we performed a calculation with $L = 5$, $b = 1000$ in which we computed the negative real part of the 32 eigenvalues with real part closest to zero for a wide range of λ with fixed boundary conditions. The resulting eigenspectrum is displayed in Fig. 3.3. Of course, for such a system we expect that all eigenvalues have negative real part, as we discussed in 3.1, so we have chosen to plot the negative real part divided by λ as a function of λ ; the zero eigenvalue, which we expect to exist and is generally found to exist in numerical terms, has been ignored, as its magnitude is simply an artefact of the numerical calculation and is therefore meaningless except possibly as a check on the numerics. The decision to divide by λ was taken because the eigenvalue closest to 0 (which dominates approach to equilibrium) mostly scales as $\mathcal{O}(\lambda)$, so plotting without division uses graph space poorly.

There are a several things to note about this spectrum:

- It would appear that, for all λ , there is a single eigenvalue which is closest to 0 and undergoes no definitive crossing as λ varies. At both extremes of λ , it clearly scales as $\mathcal{O}(\lambda)$, but is unusually low in an intermediate regime of $\lambda \in (0.03, 10)$, reaching a minimum at $\lambda \sim 0.3$, which could be interpreted as an “avoided crossing” with the 0-eigenvalue. This is important, as the eigenvalue with smallest negative real part is the one that controls the approach to equilibrium; thus, we can see that around 0.3 the system should take unusually long to relax from an arbitrary prepared state to equilibrium.
- All eigenvalues tend to scale as $\mathcal{O}(\lambda)$ as $\lambda \rightarrow \infty$.

Figure 3.3 The TRM eigenspectrum, computed for a system with $\rho_0 = 0.6$, $\rho_L = 0.4$, $L = 5$, $b = 1000$. Here we have plotted $-\Re\lambda$, as λ is expected to be a complex number with negative real part.



- Eigenvalues other than the bottom one tend to scale as $\mathcal{O}(1)$ at small λ . Thus, whilst the overall approach to equilibrium occurs with rate $\mathcal{O}(\lambda)$, there are still plenty of (probably more localised) processes occurring over much quicker timescales, whilst the whole system is sluggish to equilibrate.
- The eigenvalues tend to retain their order at the extremes of λ , but they frequently cross, merge and separate again in the intermediate regime. This suggests that something complicated is occurring; an analytic solution to this dynamical model would need to describe these crossings in detail, as they are important as eigenvalue crossing implies the appearance of degenerate eigenspaces in the decay modes which the associated eigenvectors refer to. This makes it look rather unfeasible that such an analytic solution could be constructed in the first place.

Of course, this is only the 32 eigenvalues with real part closest to zero; there could be different behaviour in the other ones. Before we perform a larger calculation however, let us turn our attention to the dependence of the eigenspectrum upon b and L , which we have studied by repeating our calculation with different values for those parameters, as shown in Fig 3.4. Again, there's a lot going on in this image, so let's break it down.

- Firstly, let us note that keeping L constant and switching b between 100 and 1000 seems to have very little impact on the eigenspectrum, as we can see by the fact that the points corresponding to the same system sizes are more or less lying on top of each other unless we delve into the low- λ limit of the $L = 5$ system. In the same limit, we see that the discrepancy is vastly reduced in the $L = 10$ system, suggesting that it is less bad for large systems, and is in some sense a small-size effect. Regardless, it would appear to be the case that adjusting b doesn't affect these low-lying eigenvalues very much, so it seems to be playing its role as a regularisation parameter as intended. Thus, we're simply going to use $b = 1000$ from now on, unless explicitly specified otherwise.
- The bottom eigenvalue, which controls relaxation to equilibrium, is generally several orders of magnitude lower for the $L = 10$ system than for the $L = 5$ one; this effect is particularly extreme in the limit of small λ . This makes sense; the larger system should take much longer to equilibrate than the smaller one, as so many more fluctuations need to occur to make it

Figure 3.4 The lower (negative real) TRM eigenspectrum, computed for a system with $\rho_0 = 0.6$, $\rho_L = 0.4$, with all combinations of $L = \{5, 10\}$, $b = \{100, 1000\}$. Missing computations, visible via the vertical gaps in the data, are due to computational issues, rather than being numerically meaningful. Note that in many places green/black and blue/red lines overlap, because their results are so similar; the image is deliberately prepared in a high resolution so that these intricacies may be observed, at least in the digital copy.

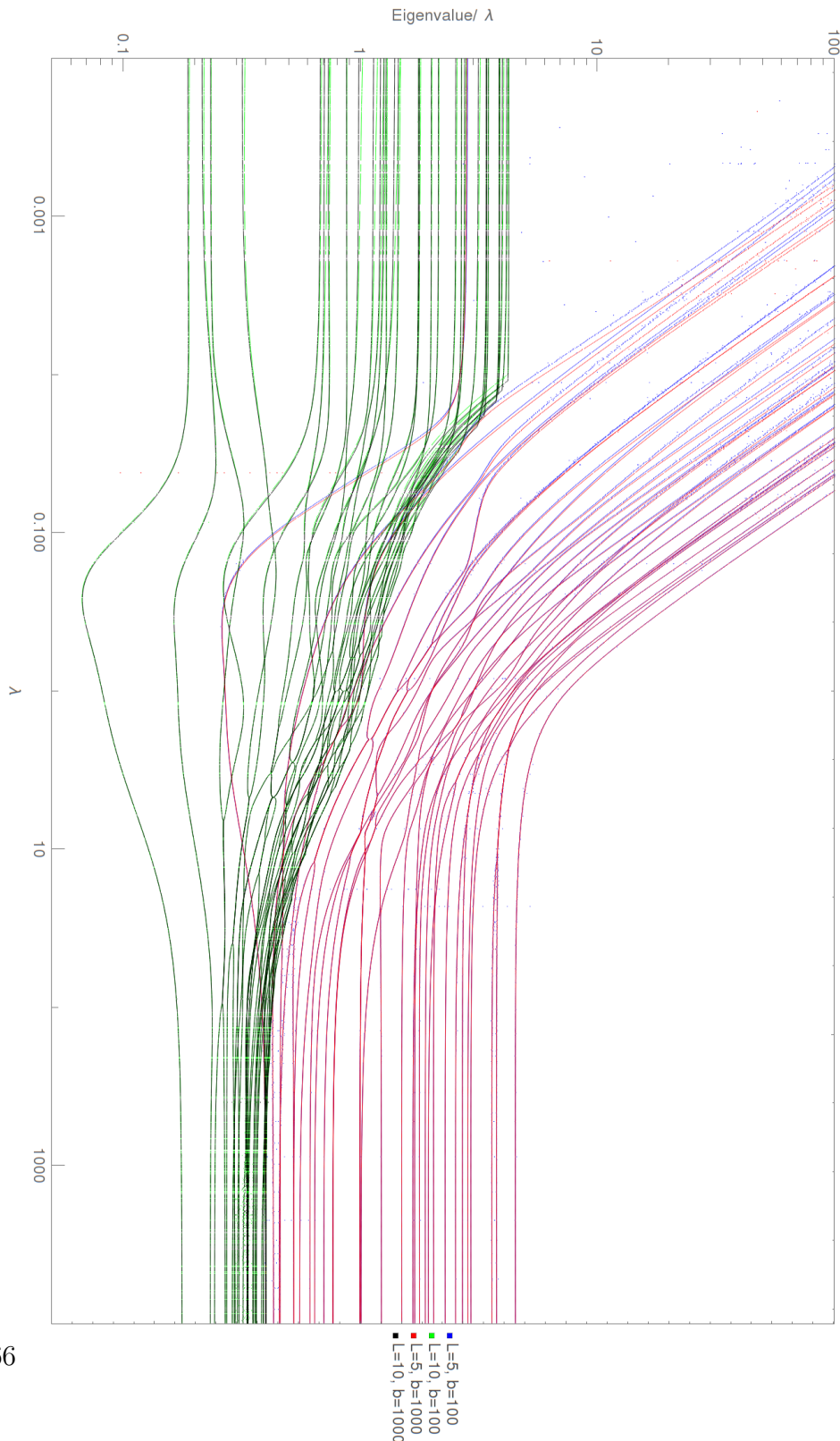


Table 3.1 A table of the number of slow modes occurring at low λ for given L .

L	5	6	7	8	9	10	11	12	13
Nº. Slow Modes	1	3	6	11	20	36	64	113	199

change its global state. This is something we should remember for later, as it suggests that equilibration time might scale pretty aggressively with system size, which is bad news for our attempts to simulate the system using Monte-Carlo methods (Ch. 4).

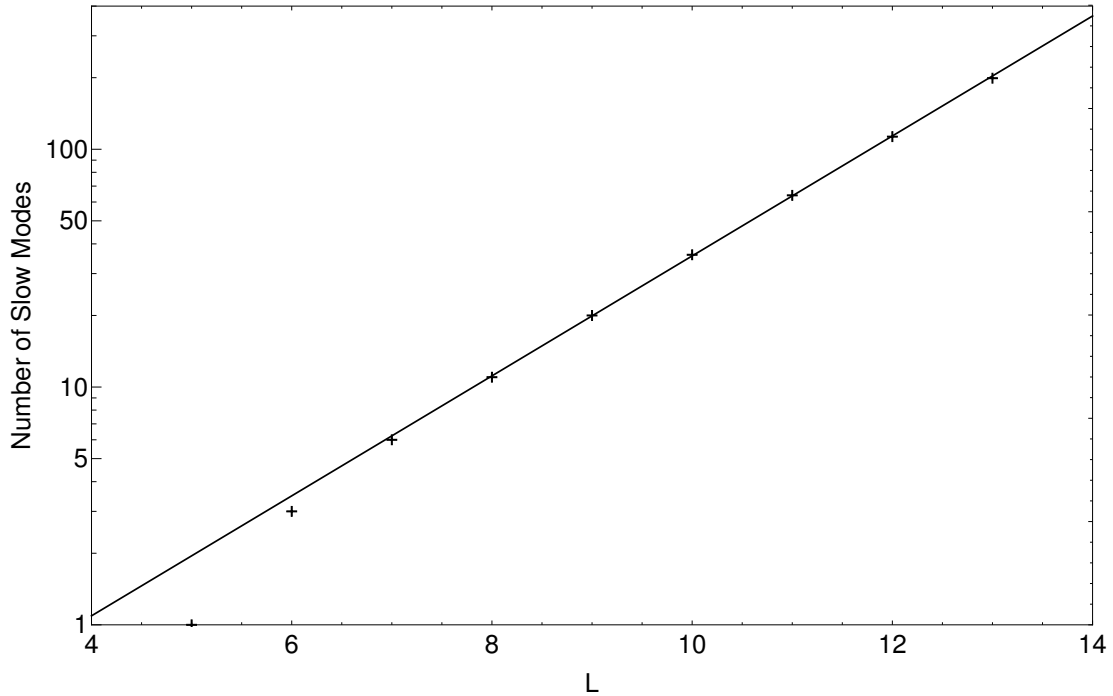
- The big, obvious difference between the spectra of different system size is the behaviour at small λ . For $L = 5$ there is only 1 eigenvalue which scales as $\mathcal{O}(\lambda)$ as $\lambda \rightarrow 0$, whereas for $L = 10$, it would appear that they all do!

The last point begs the following question: how does the number of eigenvalues corresponding to “slow modes” at small- λ scale with the system size? This is important, because it determines how many of the available decay modes would tend to persist for any meaningful amount of time during the relaxation towards equilibrium. We will attempt to address this in the next subsection.

The Scaling of the Number of Slow Modes at Low λ

To find out how the number of nonzero eigenvalues in the $\mathcal{O}(\lambda)$ -scaling band (as observed in Fig. 3.4) scales with system size, we can simply fix λ to be sufficiently low (say, $\lambda = 0.0001$) and repeat computations of the low-lying eigenspectrum for different L . Here, due to the computational limitations we are up against, we only compute up to $L = 13$. The number of slow modes as a function of L is displayed in Tab. 3.1. If we plot the number of slow modes as a function of system size on a plot with a logarithmic y -axis, as we have done in Fig. 3.5, it is rather obvious that this number scales exponentially with system size. However, the number of slow modes seems to scale as $\mathcal{O}(2^{0.84L})$, whereas the number of possible states, and therefore the total number of eigenvalues of the TRM, scales as 2^L . Thus, one can see that although the number of slow modes grows very aggressively with the system size, it would appear to eventually become outpaced by the growth in the total number of eigenvalues; in this way, we can say that the slow band carries increasingly less of the total eigenvalue density as system size becomes large.

Figure 3.5 A plot of the scaling of the number of slow modes in the eigenspectrum of the TRM of an SPM system of size L . The trendline displayed has equation $N^{\text{Slow Modes}} = 2^{a(L+b)}$, with $a = 0.84$, $b = -3.9$.



The Upper Part of the Spectrum

By varying L and b and analysing the lower (more physically relevant) part of the TRM eigenspectrum, we concluded that b has very little impact and essentially acts as a regularisation parameter, whilst L , the system size, has a large impact, particularly on the approach to equilibrium. However, both b and L contribute to the actual numbers contained within the TRM, so it stands to reason that they must impact the eigenspectrum in some way. Therefore, we have done an additional check, by varying b and L and performing a calculation in which the 64 eigenvalues with largest negative real part were calculated. The negative real parts of these eigenvalues are displayed in Fig. 3.6. We see that now the tables are indeed turned. Altering L does have a very small effect on the upper band, as we can see by how the red/black and blue/green points lie on top of each other. On this graph, we see that for the $L = 5$ datasets there are apparently two bands, whilst for $L = 10$ there is only one; however, recall that we have produced this by plotting the negative real parts of the 64 eigenvalues with largest negative real part; thus, as the $L = 10$ systems have $2^5 = 32$ times as many eigenvalues in total,

it makes sense that we may not have finished the very top band in the $L = 10$ case yet whilst we have moved on to the second band in the $L = 5$ case; thus, we conclude that system size has little effect on the top of the eigenspectrum.

The value of b , however, has a huge impact, as it determines the overall magnitude of these larger eigenvalues. The eigenmodes associated with them almost certainly relate to fluctuations at the boundary, and then the ensuing joint fluctuations travelling a little into the bulk. As these are boundary effects, it again makes sense that L has little impact. The value of b directly controls the speed of the fluctuations at the boundary, thus the large shift in magnitude observed should be expected.

Large Calculation

Now that we are more or less satisfied that the value of b doesn't matter so long as it's quite large, let's perform a similar calculation (sweeping through λ with constant boundary conditions), but this time compute a lot of eigenvalues in order to get a general overview of the TRM. Plotted in Fig. 3.7 are the negative real components of the 1024 eigenvalues with smallest negative real part, for the TRM of an SPM system of length $L = 8$ and regularisation parameter $b = 1000$. We say that this is the “full” eigenspectrum not because we have computed all of the eigenvalues (we have not, as there are $2^{12} = 4096$ in total), but because the eigenvalues with very large negative real part seem to converge upon each other, forming the hyperbola-shaped entity towards the top of the graph. We believe that this is because the relevant dynamical modes correspond to extremely rapid changes in system state which are limited to the region immediately around the boundaries; as these should have no impact on large-scale properties such as the current, they are of very limited interest to us.

This large computation continues the themes we have seen in the small ones:

- For large λ there is a thick band of eigenvalues spread over a couple of orders of magnitude which scale as $\mathcal{O}(\lambda)$.
- For intermediate λ the bottom eigenvalue becomes unusually small, whilst the higher ones in the thick band are constantly crossing over each other.
- As we go to small λ a thin band of $\mathcal{O}(\lambda)$ -scaling eigenvalues split off from the main sequence, which scales as $\mathcal{O}(1)$.

Figure 3.6 The upper (negative real) TRM eigenspectrum, computed for a system with $\rho_0 = 0.6$, $\rho_L = 0.4$, with all combinations of $L = \{5, 10\}$, $b = \{100, 1000\}$.

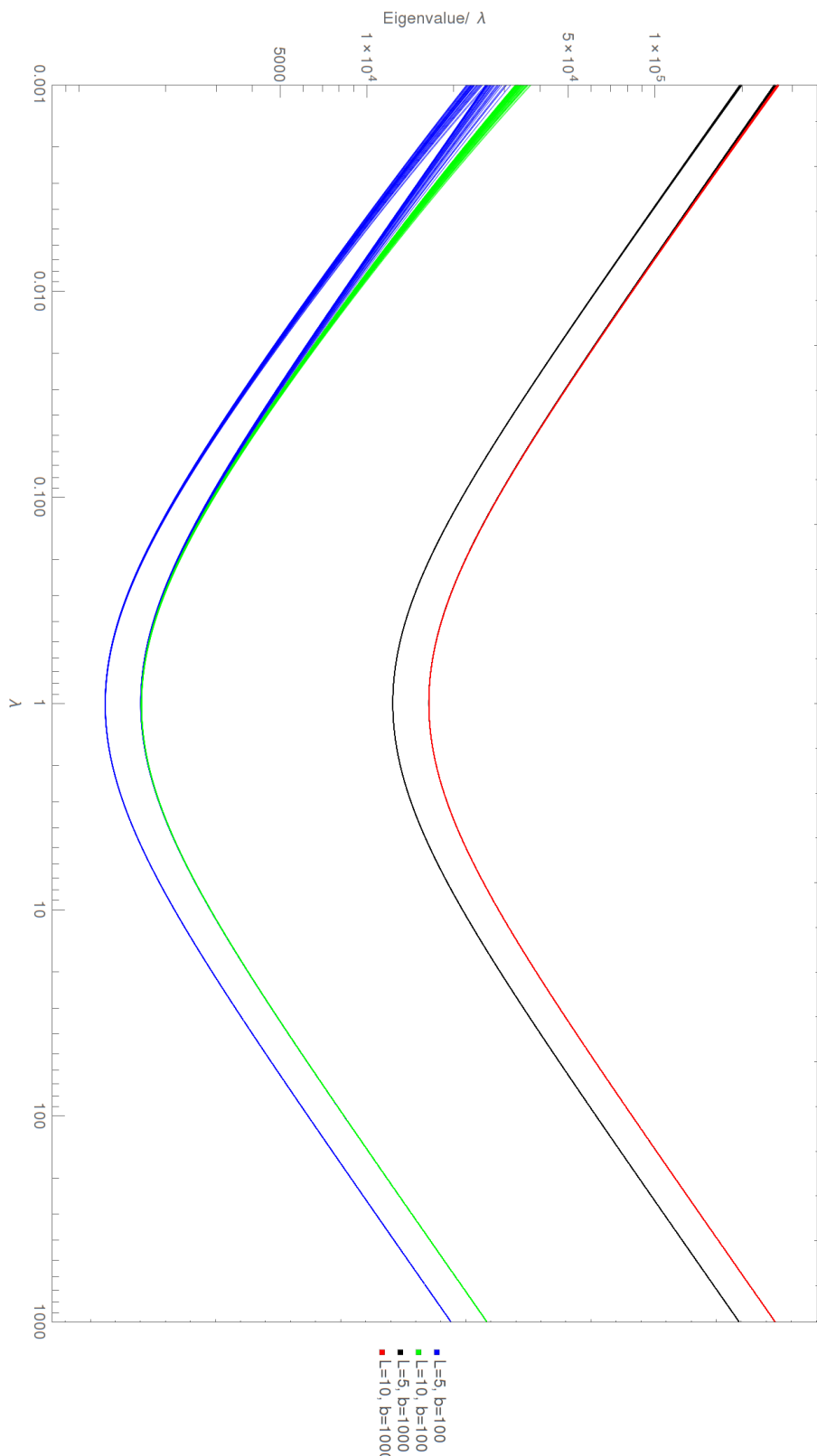
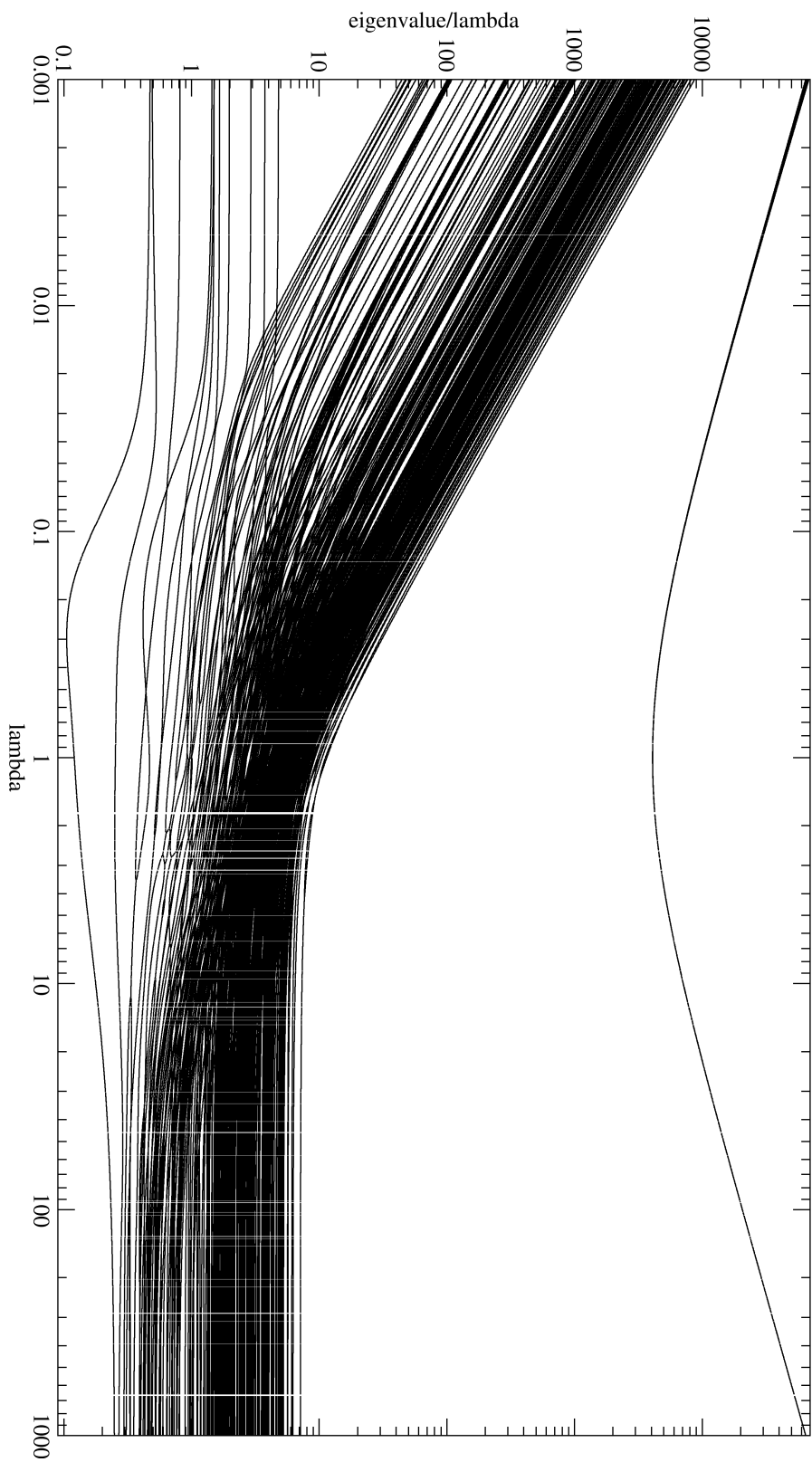


Figure 3.7 The “full” (negative real) TRM eigenspectrum, computed for a system with $\rho_0 = 0.6$, $\rho_L = 0.4$, with $L = 8$, $b = 1000$. Missing computations, visible via the vertical gaps in the data, are due to computational issues, rather than being numerically meaningful.



- For all λ there is the hyperbola-shaped band of eigenvalues with highly negative real part, which are many orders of magnitude different to the main sequence; thus, their dynamics operate over an extremely short timescale, and they are almost certainly attributable to the flickering motion at the boundaries.

3.3.3 Current and Density in the Steady State

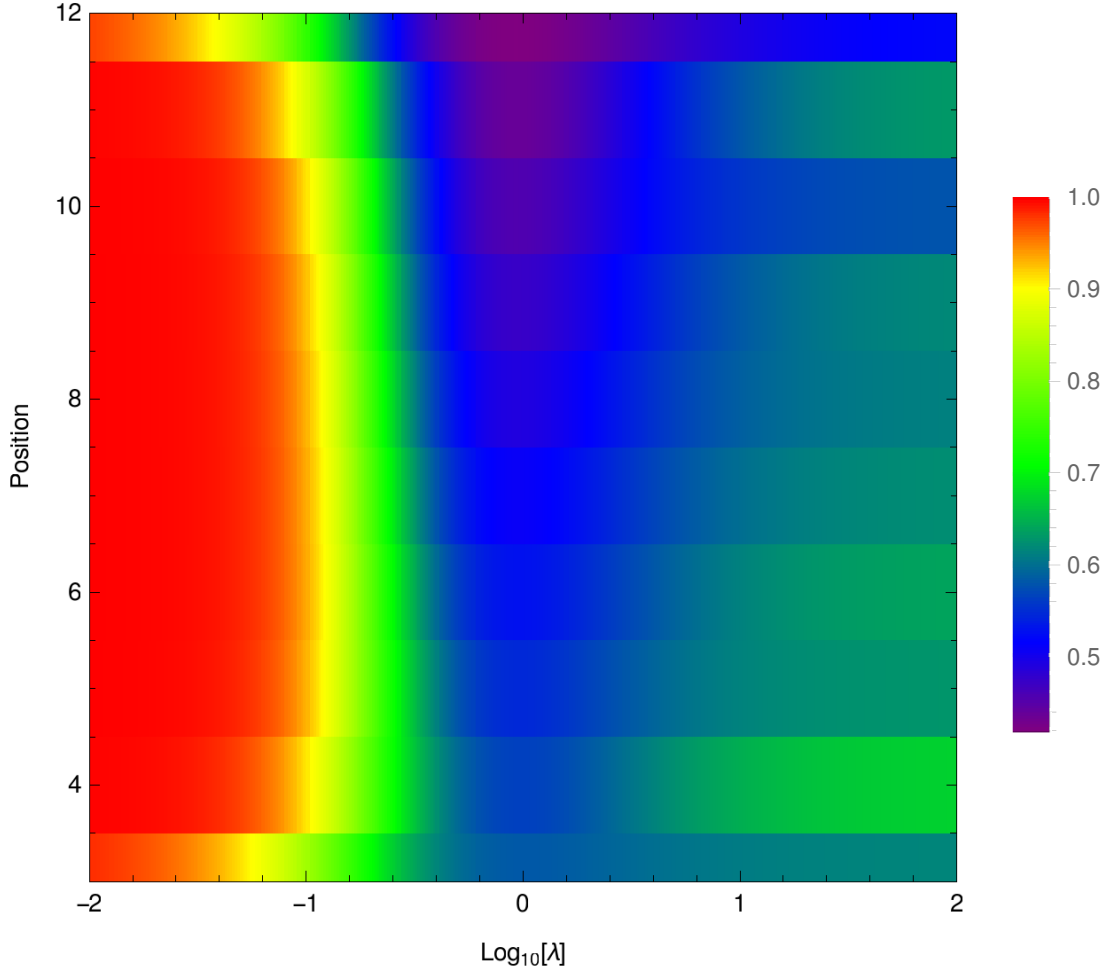
The eigenvectors of the TRM correspond to decay modes, and in general contain both positive and negative components; thus, they do not in general correspond to a particular distribution, only to a time-dependent part of a sum of vectors on their way to equilibrium. The exception to this is the 0-eigenvalue eigenvector, which **does** correspond to a physical state, if properly normalised.

Given a vector corresponding to a normalised probability distribution, we can extract the mean occupation of its i^{th} site by taking the inner product of the distribution vector with a vector which has component 1 on states in which the i^{th} sites is occupied and 0 otherwise. Thus, we can construct an operator $P : \Xi \rightarrow \mathbb{R}^{L+4}$ which can tell us the density profile of the system given its ground state, which we have found using the linear algebraic methods discussed in Sec 3.3.1. We can create a similar operator $J : \Xi \rightarrow \mathbb{R}^{L+3}$ which gives the current; however, if used on a steady state, it simply gives a constant result internal to the system, due to the existing constraint that particle number is conserved. We can of course extract the homogeneous current through the system by using this operator and then simply keeping one of the current components.

TRM-Computed Density Profile

By way of example, we computed the density profile for a system with $L = 10$, $b = 1000$, again sweeping through a wide range of scales of λ as in the previous section. We kept the boundaries constant with our usual $\rho_0 = 0.6$, $\rho_L = 0.4$ configuration. A density plot of the data is shown in Fig. 3.8. Looking at $\lambda = 1$, we see that there is a roughly constant gradient for the density profile between the boundaries, which makes sense as this is the simple exclusion limit, so it's essentially just normal diffusion. As we go to smaller λ , we see that the system in general is quite full. Presumably this is because material has been sucked into the system due to the attraction implied by the small λ ; this indicates that the

Figure 3.8 A coloured plot showing the variation of the density profile with λ in steady state for a system with boundary conditions ($\rho_0 = 0.6, \rho_L = 0.4$) of size $L = 10$. Note that the indices of the internal sites are 3-12 inclusive, as 1-2 and 13-14 are reserved for the boundaries, whose densities are already prescribed and therefore aren't plotted here.



boundaries used are a bit odd in this limit, as the system might not naturally form a homogeneous phase for such a λ and could instead wish to form a mixture of lower and higher density clumps.

Our theory about why this occurs is as follows. At large λ , we see that the density profile defaults to $\rho \sim \frac{2}{3}$ plus oscillations on the boundaries which decay as we go towards the interior. This is suspiciously close to the critical density of the MFT (Ch. 2) which permits a maximal flow; therefore, we suggest that the system self-organises at high λ to favour configurations that permit high current. The reason this density permits a high current is that in such a configuration, any particular particle should on average be in contact with an adjacent particle, with

a free space to move into, so the dynamics of the system should be dominated by λ rather than 1. If the density were higher, some particles don't have spaces to move into, so that will slow things down; if the density were lower, particles aren't receiving the speed benefit of being a neighbour. We believe that this self-organisation occurs in the bulk, with thin boundary layers occurring near to boundaries with densities fixed away from $\frac{2}{3}$. We believe that this thin layer is revealed by the oscillatory layer observed near to the boundaries; right next to the boundary, in alternating sites, particles will tend to linger in sites where they are alone, rapidly leaving when they are prompted by the arrival of a new particle in the space next to them. This effect then smooths out as one goes deeper into the bulk.

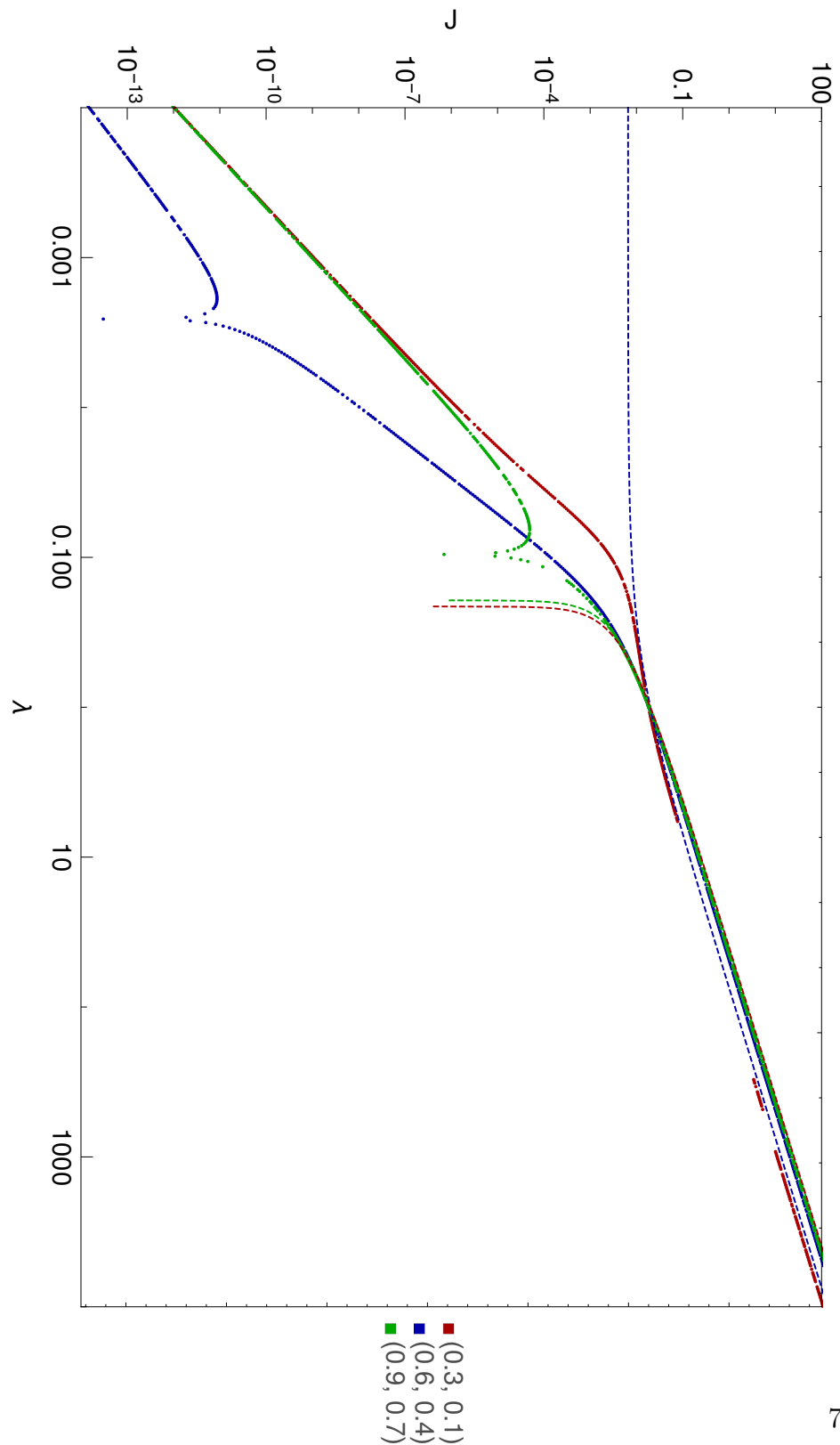
As for why a density which permitted fast flow would be favoured, consider what happens when a region of low flow comes into contact with one of high flow: the high-flow region will invade the other region with particles or vacancies, raising the overall flow rate (which previously would have been limited by the slowest-flowing region) and thus flushing out or bringing in new particles. In this way, the system as a whole will tend to favour the fast-flow densities, as they are more stable than the alternatives. We discuss more numerical data about the system density in Sec. 4.3.2, and that seems to generally support the conclusions we have reached here using our TRM method.

TRM-Computed Current

Whilst we computed the density profile, we also measured the steady state current. We also performed the same computation for different boundary conditions, and the results are displayed in Fig.3.9, along with the corresponding MFT prediction. Note that some of these calculations failed, hence the gaps in the spectra. There's a lot going on here, so let's break it down.

- At large λ , we see that the scaling ($\mathcal{O}(\lambda)$) is the same for both the MFT and the TRM numerics. The actual values predicted by the MFT and the TRM calculations differ slightly, but not by a great deal until we have $\lambda < 1$. It is to be expected that there is a discrepancy, as the MFT is in the continuum-limit whereas the TRM system is only of size $L = 10$. Furthermore, there should be a discrepancy anyway as the TRM system is not mean-field; it just doesn't seem to be so relevant in this regime.

Figure 3.9 A logarithmic plot showing the variation of current with λ in steady state for a system with boundary conditions (ρ_0, ρ_L) as indicated with system size $L = 10$. The current measurement is oriented so that positive current corresponds to flow from high density to low (the normal case). The relevant MFT prediction is shown via a dashed line in each case.



- At $\lambda = 1$, MFT and TRM calculations coincide, because the boundary conditions all differ by the same amount and $\lambda = 1$ is the trivial case of simple exclusion.
- As we explore very small values of λ , we find that the MFT and the TRM have very little resemblance. For boundary conditions $(0.3, 0.1)$ and $(0.9, 0.7)$ the MFT predicts that the flow should start running backwards or at the very least be pinned at zero, whilst for $(0.6, 0.4)$ it suggests that the current should tend to a constant as $\lambda \rightarrow 0$. Instead of the flow discontinuously switching to zero, the TRM results show a more gradual reduction of the current. Measurement by comparison with a trendline shows that the current varies as $\mathcal{O}(\lambda^3)$ as λ becomes small.
- There is an intermediate regime in which the dependence of the current upon λ transitions between $\mathcal{O}(\lambda^3)$ and $\mathcal{O}(\lambda)$. This is the situation for $\lambda \in (0.03, 0.5)$.
- There is also some slightly odd behaviour on display in terms of the apparent “poles” in the current for the $(0.6, 0.4)$ and $(0.9, 0.7)$ -boundaried systems, observed around $\lambda = 0.002$ and $\lambda = 0.1$ respectively. This could be due to a close-approach of the 0th and 1st eigenvalues, causing the algorithm to pick the wrong one under certain circumstances. We have attempted to filter the results by imposing the inequality $\|q_0\| \leq \lambda K$ for $K = 10^{-9}$ with q_0 being the “zero” eigenvalue, but some results may have slipped through this net. Likewise, this criterion may have been too stringent in some cases, resulting in otherwise valid datapoints being removed (hence the gaps observed in the $(0.3, 0.1)$ data at higher λ -values).

So, it seems that whilst we don’t see a transition to zero flow as predicted by the MFT, we do see a big change in the way the flow depends upon λ as we pass between the large- λ to small- λ regimes.

TRM-Computed Diffusion Coefficient

It is also possible for us to compute an approximation to the effective diffusion coefficient. Recall that the diffusion coefficient D should satisfy

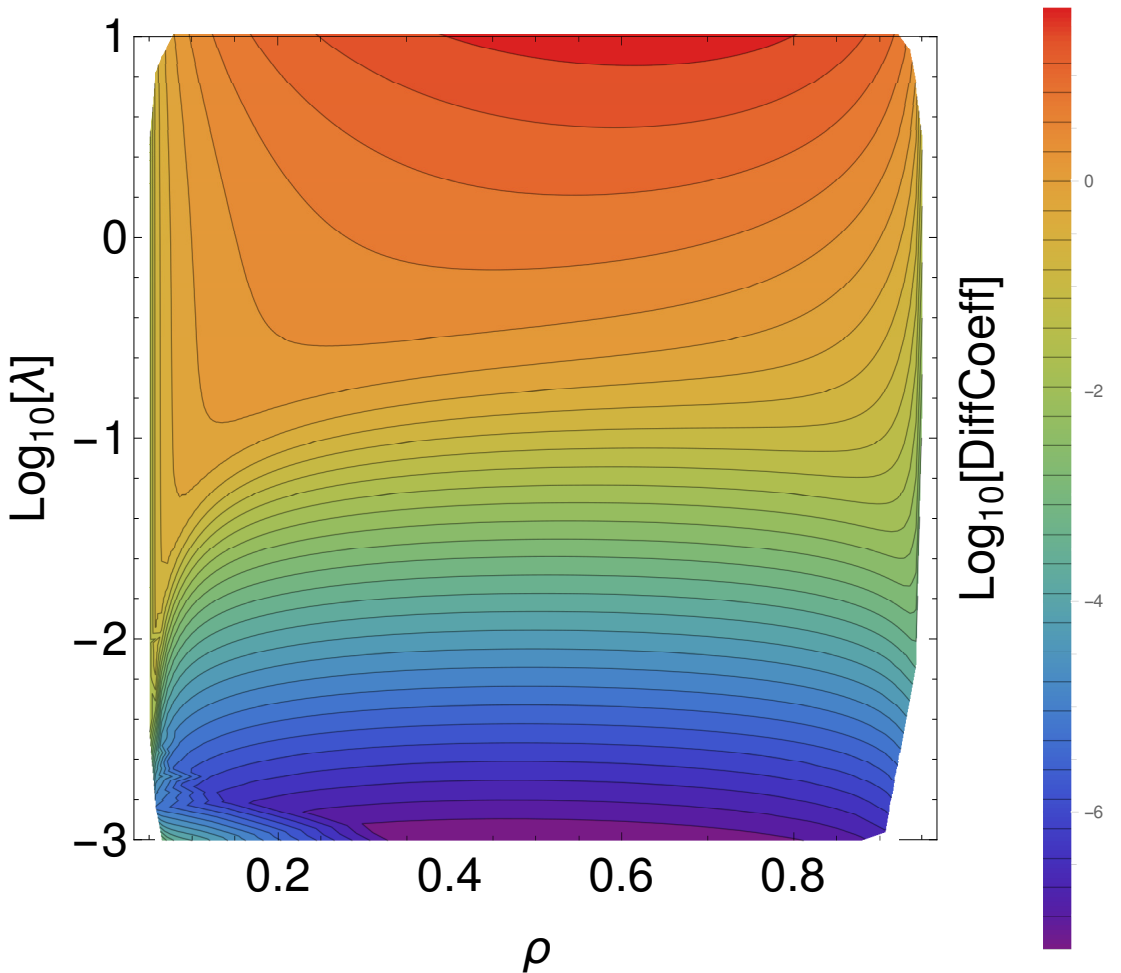
$$\mathbf{J} = -D\nabla\rho; \quad (3.20)$$

thus, we should be able to compute the diffusion coefficient using the TRM by computing the current J with boundary conditions $(\rho_0, \rho_L) = (\rho + \frac{1}{2}\delta\rho, \rho - \frac{1}{2}\delta\rho)$, and then evaluating the quantity

$$D(\rho, \lambda) = \frac{L}{\delta\rho} J. \quad (3.21)$$

We performed such a calculation, in which we picked $\delta\rho$ to be 0.001 and $L = 10$. We tabulated D for a range of λ and ρ , and a contour plot of the data is displayed in Fig. 3.10. In general, for given $\lambda < 1$ we see that the variation with ρ is

Figure 3.10 A coloured plot showing the variation of the diffusion coefficient with λ and ρ in steady state for a system of size $L = 10$.



usually pretty mild, with the more extreme diffusion coefficients tending to occur for intermediate ρ . The exception to this occurs primarily at small- λ , low density, where the diffusion coefficient is unusually high. This is presumably because the density of particles is so low that the small value of λ has little impact on the

diffusion coefficient. There is also some odd behaviour, in particular for extremely low λ and low ρ . We probably shouldn't trust those results. As $\lambda \rightarrow 0$, the space of vectors with eigenvalue zero switches from being 1-dimensional to being very high-dimensional, because any state containing adjacent particles becomes a steady state (and in fact an absorbing state). Thus, we should expect that at some as we go to smaller and smaller λ our calculations should start behaving badly because the lower nonzero eigenvalues become numerically indistinguishable from the actual zeros, and that is probably what is happening here. For $\lambda > 1$, we see that maximal flow for a given λ occurs for intermediate values of ρ , consistent with the normal SEP result for $\lambda = 1$. We can see that as λ becomes large, the maximal flow density drifts towards $\rho = \frac{2}{3}$; this agrees with our notion, backed by the MFT, that maximal flow at large- λ should occur for $\rho = \frac{2}{3}$.

The trend in terms of λ is that the gradient of the diffusion coefficient as it varies with λ and ρ is generally low for large λ and high for small λ . In light of our results in Fig. 3.9, this makes sense as the power law seems to change as we switch between low and high λ . This suggests that an order parameter of the form

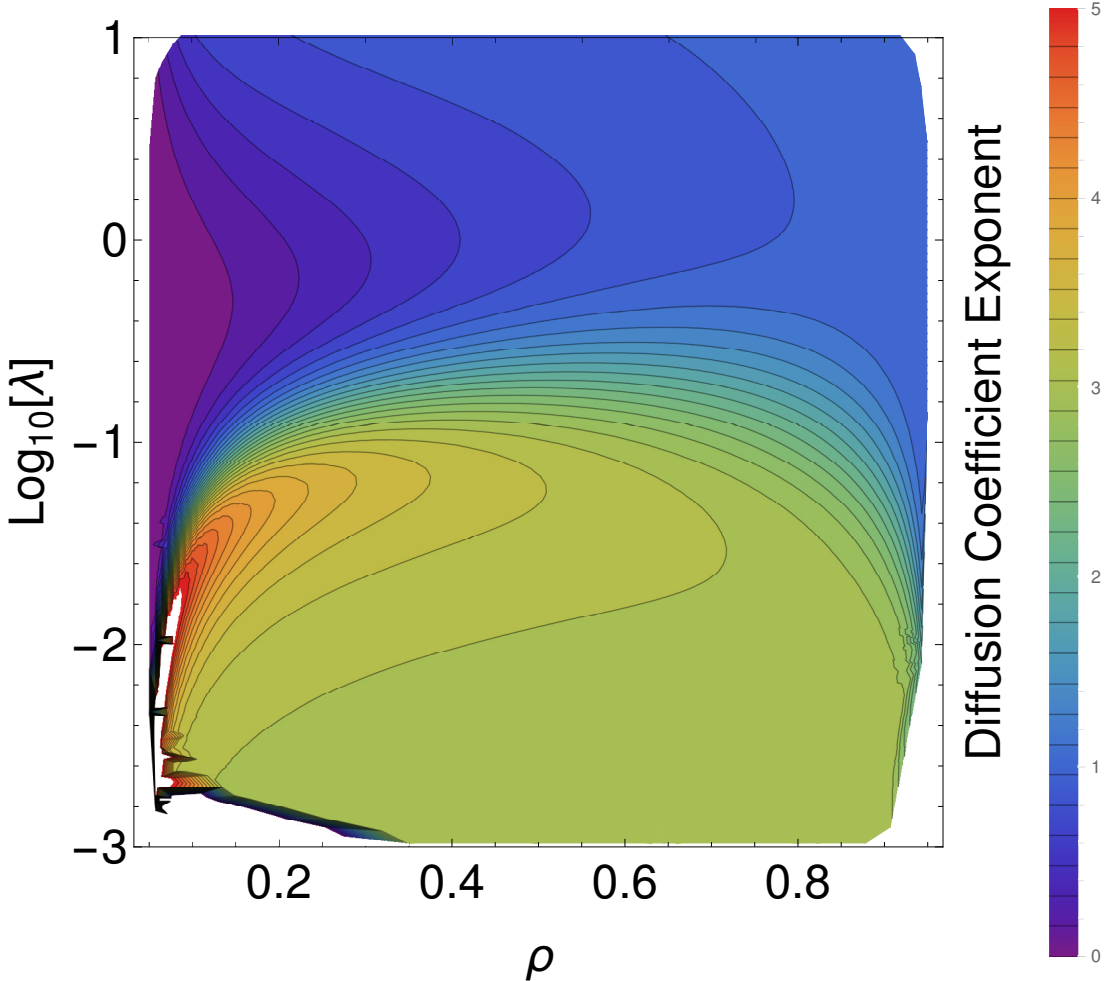
$$\chi(\rho, \lambda) = \left(\frac{\partial \ln D}{\partial \ln \lambda} \right)_\rho \quad (3.22)$$

should reveal the power-law structure. We can compute this from our existing data in Fig. 3.10, and it is displayed in Fig. 3.11. As you can see, this order parameter does seem to nicely partition (ρ, λ) space into two components, divided by a region of extremely rapid change. The order parameter χ could be regarded as some kind of susceptibility. An issue here is that it is hard to see how χ 's apparent transition will vary with system size, as $L = 10$ is a very small system, and transitions only become sharp in the limit of large systems. We could of course use it in a Monte-Carlo calculation in a larger system, but then we have the problem that it's difficult to take meaningful derivatives of noisy data. We will leave it, then, as a curiosity.

3.4 Time-Dependent Properties of Small SPM Systems

Although we have mostly concentrated on calculating steady state properties of the SPM, it is also possible to calculate some dynamical properties.

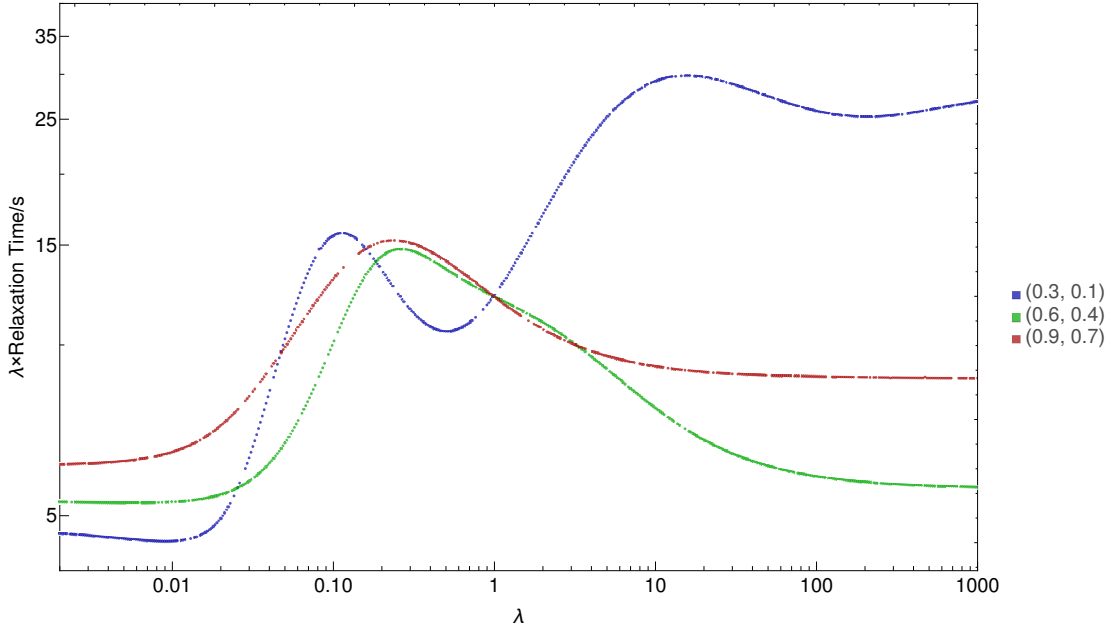
Figure 3.11 A coloured plot showing the variation of the order parameter χ with λ and ρ in steady state for a system of size $L = 10$.



3.4.1 The Relaxation Time for the SPM

As we have seen, the eigenvalue with least negative real part effectively controls the rate at which a generically-prepared system equilibrates, by acting as a lower bound on the rate of relaxation towards equilibrium. Therefore, the reciprocal of this relaxation rate should yield a characteristic time for convergence to equilibrium, the relaxation time. We have computed this relaxation time for our three standard boundary conditions in Fig. 3.12. Notice first that we have plotted the relaxation time multiplied by λ , as the relaxation time generally scales as $\mathcal{O}(\lambda^{-1})$. One can see why we made this choice by looking at the extremes, where the lines are generally quite flat.

Figure 3.12 A plot showing the dependence of the relaxation time upon λ for a system of size $L = 10$ with boundary densities $(0.3, 0.1)$, $(0.6, 0.4)$ and $(0.9, 0.7)$. In terms of units, here we are presuming that the default diffusion rate $\tau_0 = 1\text{s}^{-1}$.



Observe that the relaxation times for large λ are generally a little higher than for low λ once the $\mathcal{O}(\lambda^{-1})$ dependence is taken into account. In particular, the system with low densities at the boundary is much slower to relax to equilibrium than the system with high boundary densities, which in turn is slow compared to the system with medium densities. This is presumably because the system is attempting to reach the maximal flow density we observed, $\rho = \frac{2}{3}$, and it finds it more awkward to do that the further away the furthest boundary is from $\frac{2}{3}$.

For very low λ , the difference between boundary configurations isn't so great, and we believe that the differences between the boundaries occur for the same reason as for the high- λ situation, only now the system is trying to fill instead of hold at $\rho = \frac{2}{3}$. For intermediate λ , things are less clear. At $\lambda = 1$, all systems equilibrate at the same rate; other than that, behaviour varies pretty wildly. Equilibration time is generally on the high side for $\lambda \in (0.03, 1)$, which is where the current looks like its undergoing some kind of transition, so this increase in relative equilibration time could be interpreted as an accumulation of fluctuations in that regime.

3.4.2 Time-Evolution of States

Recall from Sec. 3.1 that the Master Equation (Eq. (3.1)) has a formal solution given by Eq. (3.8), in which we premultiply the initial state by a matrix exponential of the TRM. Throughout this chapter we have been making use of the fact that the TRM is sparse in order to perform our computations. Thus, it would seem that we couldn't investigate the time evolution of systems, as e^A is in general not sparse even if A is sparse, and thus we would instantly run out of memory if we tried to compute anything.

However, the premultiplication of a vector by a sparse matrix can be performed *in place*, and this is implemented by Python's routine

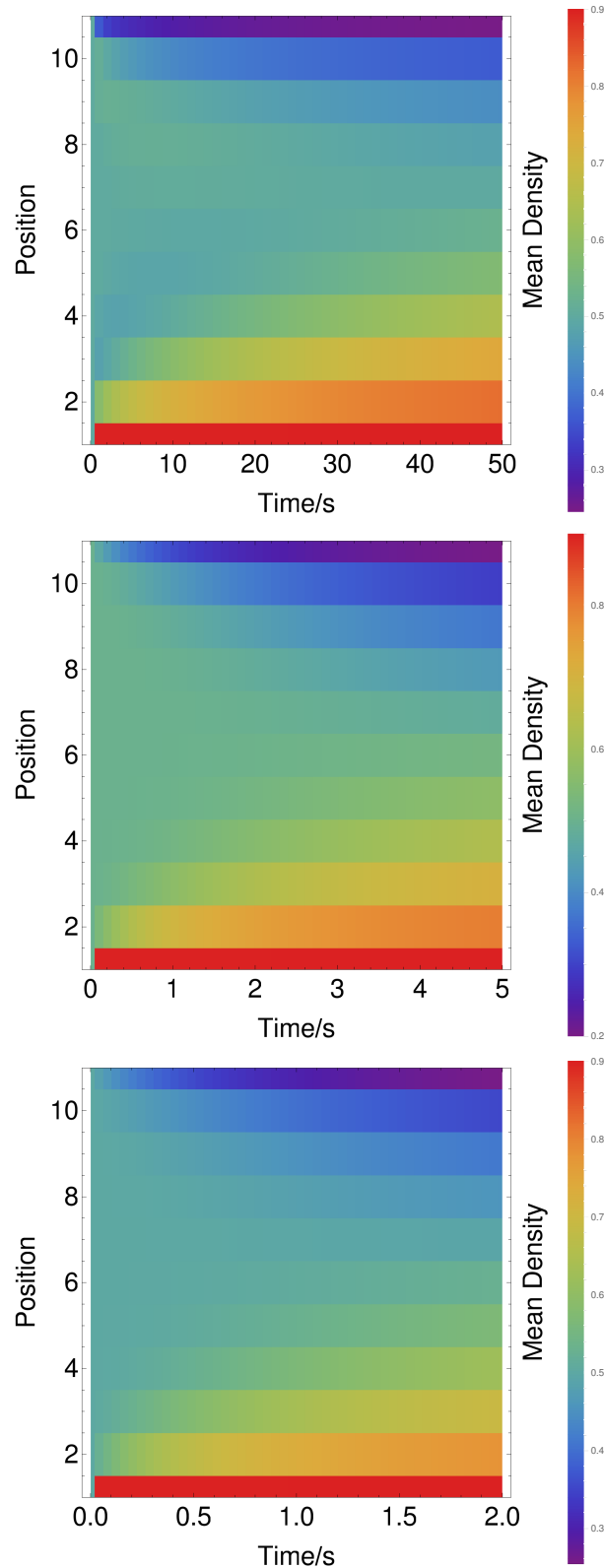
`scipy.sparse.linalg.expm_multiply`. Therefore we have been able to calculate the time-evolution of arbitrary initial distributions. By way of an example we prepared three systems with initial uniform distributions, in which all possible configurations are equally likely, and then monitored how their spatial occupations varied as they relaxed towards equilibrium (which should always occur, as discussed in Sec. 3.1). The results are displayed in Fig. 3.13. In the plots we have included the innermost site in the boundary layer; notice that it switches to the “correct” mean occupation almost instantly, which is exactly what is supposed to happen as it represents a highly responsive reservoir. The system then gradually makes its ways toward equilibrium, starting at the boundaries and working inward, and the characteristic timescale over which this occurs seems to be in line with our results from 3.4.1.

Of course, this is more of a demonstration of what this method could achieve than an actually useful result. We are quite sure that with a little effort one could use it to calculate time-dependent spatial correlation functions, for example, but we simply worked out how to perform TRM calculations too late in the project to be able to use it to full effect.

3.5 Conclusions

Numerically approximating the eigenpairs of the transition rate matrix is a convenient alternative to the use of Monte Carlo methods for the computation of the properties of a Markovian statistical mechanics system. When using the TRM, we sacrifice system size for accuracy, as the memory requirement for TRM

Figure 3.13 Plots of the time-evolution of the density profiles of systems prepared with uniform distributions. These systems are of size $L = 10$, with boundary densities $(0.9, 0.1)$, $b_0 = 100.0$ and $\lambda = \{0.1, 1.0, 2.0\}$, going from top to bottom, respectively. The total time intervals have been adjusted to suit the equilibration time.



calculations scales exponentially with system size, whilst similar Monte Carlo calculations' memory requirements scale linearly. However, the TRM method avoids the sampling issues which often emerge when attempting Monte Carlo simulations, and can yield the relevant statistics with relative ease once the matrix computations are completed. Furthermore, we can also investigate time-dependent properties at our convenience, which can be awkward in Monte-Carlo calculations as there we don't usually work with normal time.

The main reason we performed these calculations, however, is to investigate the current flowing due to the boundary conditions. We found that the MFT prediction that the currents drops to zero or becomes negative below a critical λ (depending upon boundary conditions) does not seem to be correct; however, we have found that the scaling of the current does seem to undergo some kind of transition, from $J \propto \lambda$ for large λ to $J \propto \lambda^3$ for small λ . This is something which we can investigate further using Monte-Carlo methods on larger-scale systems, and we will do this in the next chapter.

Chapter 4

Monte-Carlo Simulations of the SPM

We now have numerical results for SPM systems using TRM analysis; however, this only allows us to study relatively small systems. In order to study larger ones, we have used Monte-Carlo methods. In this chapter, we will discuss the methods we used, the results they yielded, and their meaning, with particular emphasis on what they tell us about the suspected transition between low and high- λ behaviours.

4.1 Numerical Simulations of Continuous-Time Markov Processes

Here we will discuss the theory behind the Monte-Carlo methods used to simulate continuous-time Markov processes. We will assume throughout that we have the computational means to produce pseudorandom floating-point numbers in a way which closely approximates the uniform real distribution over $(0, 1)$.

4.1.1 Purpose of Monte-Carlo Methods

We should first describe what we mean by a Monte-Carlo method. In essence, Monte-Carlo methods refer to numerical routines in which we attempt to

characterise an unknown distribution, generated via known rules, by using pseudorandom numbers in order to produce sample data which is hopefully faithful to the original distribution, at least in terms of the statistics we are trying to calculate. A good example of a commonly-used Monte-Carlo method in Physics is the Metropolis-Hastings algorithm [49], which in its original form is used to calculate statistics for equilibrium statistical mechanics systems.

In our situation, we wish to be able to mimic a continuous-time discrete-state Markov process. As we saw in Ch. 3, the state space for a TRM system of size L scales as $\mathcal{O}(2^L)$; thus we quickly run out of memory if we try to consider exact probability distributions, which correspond to vectors in \mathbb{R}^{L^2} . We can, however, store individual configurations, which only occupy $\mathcal{O}(L)$ space. Therefore, we need to find a way to produce trajectories through the discrete state space which sample the actual space of system trajectories well enough to allow us to access the statistics we want. Of course, there isn't a unique “best” way to do this. We have considered two different approaches, which differ primarily in the way in which they convert the original continuous time into discrete steps which we can use in an algorithm.

4.1.2 Evenly-Spaced Timesteps

If we wished to numerically approximate an ODE system, one might use the Euler forward [6] or Runge-Kutta [64] methods. These both involve discretising time simply by dividing it into evenly-sized pieces, and then converting the ODE into a discrete form by using finite differences to approximate derivatives. We need to be careful to choose a small enough timestep for the approximation to the derivative to remain good, but otherwise it is a very simple and effective approach.

We can do a very similar technique with continuous time Markov processes. In our SPM system, if we ignore the boundaries, there are two rates, 1 and λ , and our system is homogeneous. Let us represent the system with a binary array of length $L+2$, with L sites for the bulk and a site each representing the boundaries. Therefore, in order to simulate the action of the SPM as defined in Sec. 1.1.2, we can use the following recipe:

1. **START.** Advance time by Δt . Pick a site, which we will call Site, (of which there are $L+2$) at random. If the site chosen is one of the boundaries with

density ρ , reset the site to be occupied with probability ρ and unoccupied with probability $1 - \rho$.

2. If Site is occupied, pick one of the two adjacent sites, which we will call Target, at random with equal probability. This will be the site we attempt to move into. If Site is not occupied, go back to **START**.
3. *If Site is not on the boundary:* If Target is occupied, go to **START**. Otherwise, consider the other adjacent site, which we will refer to as Rear. If Rear is empty, move the particle in Site into Target randomly with probability $\frac{1}{1+\lambda}$; otherwise, move the particle with probability $\frac{\lambda}{1+\lambda}$. Return to **START**.

If Site is on the boundary: If Target is outside the system, go to **START**. If Target is occupied, go to **START**. Assign an occupation value for Rear randomly, occupied with probability ρ , unoccupied with probability $1 - \rho$, where ρ is the density of the relevant boundary. Now, if Rear is empty, move the particle in Site into Target randomly with probability $\frac{1}{1+\lambda}$; otherwise, move the particle with probability $\frac{\lambda}{1+\lambda}$. Return to **START**.

We define Δt via

$$\Delta t = \frac{\tau_0}{(L+2)(1+\lambda)}. \quad (4.1)$$

In terms of the algorithm's ability to produce reasonable trajectories, we simply need note that the rates at which particular transitions should occur are in the correct proportions, and that the boundaries result in the correct densities in equilibrium; then, we just need to verify that the rate at which free particles move is the correct one in absolute terms, which it is, and we're done.

For Monte-Carlo methods, we generally rate their performance by the amount of computational power required to explore a given amount of the probability space. In methods in which we are exploring this space by advancing through time (and invoking ergodicity) we desire methods which move us quickly through time whilst maintaining good sampling and performing little computation.

The advantage of this method is that it is very simple; thus, there aren't too many opportunities for error when writing the code, it uses very little memory (all calculations can be performed in-place), and each iteration should be very fast as there are very few overheads. It should also produce trajectories which are good samples of the original probability distribution we are trying to replicate.

If λ is close to 1, the probability of rejection (i.e. a step which results in no overall change to the system) is $\sim \frac{1}{2}$, and this is the situation in which the algorithm really shines; similarly it also performs well for large or small λ if the system density is very high or very low respectively. For extreme λ and generic densities, performance drops off considerably, as we are often performing lots of calculations and advancing time very little, and thus not sampling much of the distribution per computation step.

We could have made this code marginally more efficient by making the more likely moves certain, and correspondingly adjusting the timestep size Δt to account for this; however, this only improves efficiency by a factor of around 2 , whilst making the code more complicated, so as we only used this method to verify the results of our main code it didn't seem worthwhile. It is possible for us to get around this issue by advancing time in a variable fashion, although this comes at the cost of a little more computation per iteration.

4.1.3 The N-Fold Way, or Gillespie Algorithm

A popular way to produce trajectories for a continuous-time Markov process is the N-Fold Way, also known as the BKL or Gillespie Algorithm [8, 46, 59]. It evolves us through time as follows:

1. **START**: Make a list of all states which can be transitioned to in a single move from the current state, and the associated rates at which this occurs.
2. Weight each successor state by the transition rate into it, and then select a successor state by random selection from a uniform distribution over the weighted possible successors. Change the system state to the chosen successor.
3. Now advance time by an increment chosen from an exponential distribution whose decay rate is the sum of all of the rates of the possible transitions to a successor. Go back to **START**.

Now we just need to supply the rates that define the SPM (Sec. 1.1.2), along with some additional rates describing processes at the boundary. Specifically, we use the method described in 3.2.1 to do this, whereby we have a double layer of “blinking” boundary sites and sites in the internal layer undergo the same

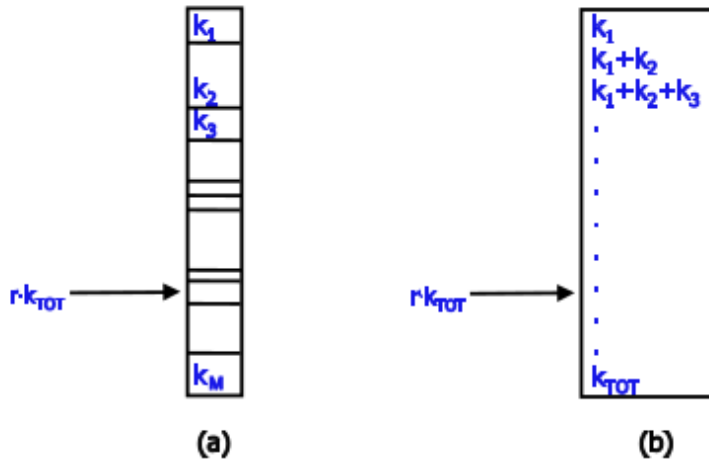
transitions as in the bulk. However, unlike in our TRM calculations, we should not set the incoming and outgoing rates to be extremely high, as then these rather trivial processes come to dominate the calculation and cause the timesteps to be on average extremely small, wasting our computing time. Instead, we set them to be proportional to the geometric mean of 1 and λ , and thus in the language of (3.12) this corresponds to setting $B_0 = \sqrt{\lambda}$. This way the boundaries refresh often, but not too often, and should still act as suitable reservoirs, which we can test by comparing small systems with Chapter 3 and comparing with code in Sec. 4.1.2.

We will get into the fine details about how the software we use implements KMC in Sec. 4.2.2. Let us first discuss how we obtain the required probability distributions using the uniform distribution on $(0, 1)$, $U(0, 1)$:

- We can randomly choose the successor state required in step 2 by creating a list of weighted partial sums. If the transition rate from the current state the i^{th} potential successor state is k_i , then let us define $k_{\text{Tot.}} = \sum_i^n k_i$, where n is the number of potential successors. Create the list of partial sums via $s_i = \sum_j^i k_j$, then generate the random number $u = rk_{\text{tot}}$ where r is drawn from $U(0, 1)$. We can then use a binary search to find $i : s_{i-1} \leq u \leq s_i$, and then this i indicates the successor state which has been chosen. This process is illustrated more visually in Fig. 4.1.
- In step 3, we need to generate random numbers in an exponential distribution with decay rate k_{tot} . We can do this by generating r from $U(0, 1)$, and then $w = -\frac{1}{k_{\text{tot}}} \log r$ follows the desired distribution.

I will defer to Voter (see in particular Sec. 5 of [59]) for the “proof of correctness” of the method. The primary advantage of this method is that we are certain to advance time every step, so we are not potentially “wasting” steps as when we use even timestepping; this comes at the cost of having to compute which transitions are possible from the current state. For our SPM, a given state has $\mathcal{O}(L)$ possible transitions, thus the time complexity of a single timestep is $\mathcal{O}(L)$; note that our method with evenly-spaced timesteps has constant time complexity, but the size of each timestep scales as $\mathcal{O}(L^{-1})$; thus we’re not actually losing as much as it appears by using variable timesteps. Furthermore, there is the possibility that the process by which we calculate which transitions are possible could be performed in parallel, and so the walltime cost of a single timestep in the n-fold way can

Figure 4.1 An illustration of the suggested method for choosing a successor state in the n -fold way. Reproduced from [59].



end up comparatively cheap. The process of choosing a successor state once the options are found involves performing the equivalent of a search, and therefore takes $\mathcal{O}(\log L)$ time and so should be insignificant.

4.2 Implementation of Monte Carlo Methods

4.2.1 Our Implementation of a Metropolis-Hastings Algorithm with Evenly-Space Timesteps

We have written a Fortran code which implements the algorithm in Sec. 4.1.2. This is stored in [19] in `evenTimesteps/evenTimesteps.f`. This programme initialises the system to have a particle density equal to the average of the two desired boundary densities, and then proceeds in a manner extremely faithful to the simple accept/reject algorithm.

4.2.2 KMCLib

The vast majority of our Monte-Carlo calculations have been performed using the n -fold way, described in Sec. 4.1.3. This is implemented for continuous-time Markov processes on crystalline lattices (of which the SPM is an example) in

a software package called **KMCLib**, documented at [32] developed by Dr Mikael Leetmaa.

KMCLib is a Python-wrapped C++ package. This means that the frontend, where one specifies the system to be simulated, the data to be recorded, and how the simulation is run, is written in a Python script; then, when this script is run, it executes C++ code in order to represent the system and actually carry out the desired operations. Furthermore, **KMCLib** can perform calculations in parallel if so desired. Whilst there exist examples [22, 45] of kinetic Monte-Carlo codes other than **KMCLib**, we chose to use that one due to our familiarity with all of the languages involved, and preference for a Python frontend.

Of course, setting up different calculations which vary different parameters or measure different things require different scripts. Going through every script we wrote individually would not be particularly instructive; therefore we have instead chosen to focus upon a single set of codes designed to perform a particular calculation, which we have annotated and included in [19] in `kmc/1d/currentCalc`; the intention is that a reader wishing to reproduce any of our results could do so by performing a few simple modifications to the code listed there. A more comprehensive codebase is stored at [20], but this is sparsely annotated working code, and so might not be as helpful.

A code which provides Python input for **KMCLib** is contained within `concFlow.py`. This script takes in several command line inputs. These provide the parameters for a simulation of the SPM, with the desired value of λ , system size and boundary conditions. It then sets up the representation of the system configuration and the means to enumerate possible transitions and their associated rates, as is necessary to implement the n-fold way. The initial configuration is generated by randomly inserting particles into the system until its density is equal to $\frac{1}{2}(\rho_0 + \rho_L)$; we then perform N_{eq} KMC steps in order to equilibrate the system (in case the initial configuration we chose was highly deviant from the norm for the prescribed parameters). The actual measurements are performed by time-averaging values for system quantities (e.g. the number of particles entering the system at one end) over N_{meas} steps, relaxing the system (in other words, performing steps but taking no measurements) for N_{req} steps, and then repeating this process N_{pass} times. This way, we can generate N_{pass} time-separated observations of, say, the total current through the system, and because we are relaxing the system between measurement runs we should not have to worry too much about the results being unduly correlated with each other, (assuming we set N_{req} high enough). Thus,

we supply `concFlow.py` with the following parameters as command line inputs:

1. The particle reservoir concentration at one end of the domain, ρ_0 .
2. The particle reservoir concentration at the other end of the domain, ρ_L .
3. The value of λ to use in the simulation.
4. The system size, L .
5. The interval between measurements performed by the analysis routines, N_{anal} . This should be set to 1 in order to measure the current.
6. The number of equilibration steps, N_{eq} .
7. The number of analysis steps per pass, N_{meas} .
8. The number of reequilibration steps per pass, N_{req} .
9. The total number of passes, N_{pass} , which give separate sets of observations, performed during this calculation.
10. A timescale, δt , which indicates how often to evaluate, and to what accuracy to record, times, when measuring the number of particles in the system. We recommend that this be small compared to the expected KMC timestep size.

In terms of the output of the code, it produces a short file summarising the input parameters, some trajectory dump information (usually redirected to `/dev/null` in order to save hard memory, which is often in short supply), as well as data taken by measurement routines. We nominate, from a suite of possible routines, which measurements we would like it to take during analysis phases. Note that in our calculations, we do not use any quantity's value during particular KMC steps; rather, we always average our quantities over some amount of time. This is partly because some of the quantities we are interested in do not really have any value during a single timestep (e.g. the flux of particles through one of the boundaries), and also because the amount of time spent in particular configurations could potentially vary wildly between configurations. The amount of time spent in a particular configuration in the n-fold way is drawn from an exponential distribution with decay rate k_{tot} , as we saw in Sec. 4.1.3; thus, one could easily imagine a situation in which the transition time varies wildly. For example, say we have a system with very low λ . If this system was quite full,

there would be few transitions possible, and those possible transitions would likely occur with low rates, therefore the KMC timesteps would tend to be very long. However, later during the same simulation we could find ourselves in a situation where the system is less full, and so more transitions can occur, and generally with much higher rates, leading to much shorter timesteps. Thus, we shouldn't really treat particular quantities derived from these configurations with an equal footing, as the amounts of time the system spends in each are so very different.

The precise nature of our time-averaging depends a little on the measurement in question. The types of measurements we usually perform are the following, where T is the total time elapsed during our N_{anal} step measurement run:

- **Current** We count the total number of particles which enter or leave a given boundary over the course of the measurement run. Let the number of particles entering and exiting at the 0 boundary be u_0 and w_0 respectively, and likewise for the L boundary with u_L and w_L . Then

$$J = \frac{u_0 + w_L - u_L - w_0}{2T} \quad (4.2)$$

should be a good estimate of the total current through the system during that time period.

- **Block Size Distribution** In one dimension, we can look at a configuration and count how many contiguous runs (“blocks”) of particles there are of different sizes (e.g. size 1 means a single particle sandwiched between adjacent vacancies). We can find the distribution of block sizes, weight it by the length of the associated KMC timestep, and then add this to a running total. If we do this over our N_{meas} analysis steps and then normalise, we can build a histogram of the block sizes during that time period.
- **Particle Density** Similarly, we can count the total number of particles in the system, weight it by the length of the KMC timestep, and then use this to build another histogram of the system particle density. By keeping track of particles entering and leaving the system, it would be possible to code this very efficiently to take $\mathcal{O}(1)$ time; however, as our routine to detect block sizes scans through the system and counts as it goes along, we have just opted for a simple $\mathcal{O}(L)$ scan of the whole system for our density measurement as well.

Using these analysis routines, we can generate time-averaged values for particle

density histograms, the block size distribution and the current. By calculating N_{pass} separate instances of these observables, we get N_{pass} samples from the relevant distributions, and from there we can probe the statistics of these variables.

4.2.3 Managing KMCLib Calculations in Parallel

Of course, it is one thing to have a code which can run on a laptop to produce the output of a particular simulation over the course of a day. It is quite another undertaking to run thousands of separate calculations in order to map out parameter spaces and compute derived quantities such as the diffusion coefficient.

We have been running our calculations on Edinburgh University’s `Eddie3` computing cluster. This machine does not boast the high level of processor interconnection density of `ARCHER` or the extremely high working memory of `DiRAC`; however, for the purposes of our calculations it turns out that we need neither. The KMC algorithm only stores a single state of the system under simulation at any given time, therefore its space complexity only scales as $\mathcal{O}(L)$. Furthermore, whilst `KMCLib` can be run in parallel mode in order to take advantage of a multithreaded environment, this isn’t actually an advantage when we wish to run very large numbers of separately-parametrised calculations, as the total amount of CPU time required remains the same, whilst incurring additional overheads associated with parallelism. Therefore, we have used a single-threaded environment for all of the calculations featured in this thesis.

In order to set up a batch of calculations, we use the following procedure, implemented by the codes stored in `kmc/1d/` within [19]:

1. Create a batch of input files, in the subdirectory `jobInputs/`. In our setup, we require that files titled `testInput.i` are generated, with $i \in [1, n]$ where n is the total number of calculations to be performed. These input files are typically generated by a code such as `lambdaFlucCreator.py`; parameters which determine the overall structure of the system (e.g. L , the system size) will usually be held constant across calculations, whilst parameters such as the stickiness or the boundary densities will be varied between them. These input files contain a single line of code, which will be appended to `python` and called in the command line.

2. In order to actually perform the calculations, we submit them as `gridengine` batch jobs. We run the script `kmcSubmit.sh`, which submits the nominated tasks whose input files are in `jobInputs/`, using the scripts `kmcJobArray.sh` and `initKmc.sh` for intermediate steps. `kmcSubmit` is also the place where we specify calculational parameters, such as maximum memory usage, maximum runtime, etc; these will be taken into consideration by `gridengine` when it comes to scheduling these calculations, so it is important that the maxima be relatively tight upper bounds, otherwise the calculation priority will be extremely low, assuming that the cluster in question is being simultaneously used for many other calculations.
3. The jobs will then be executed, in their own time. The results will be placed in the location nominated by the input files.
4. Once the run is complete, and the data has been saved, we are then ready to process it into a more useful format, in our case a data file which can be interpreted by Mathematica, the programme we used for most of our analysis and graphing. This is done using a script such a `lambdaPostProc.py`. Note that such a script needs to be able to handle the fact that data may not be produced for some of the calculations (around 5% in our experience). The most likely source of the problem seems to be an issue with type conversion between Python and C++, which only seems to become a significant issue in larger calculations.

Throughout our calculations, we have stored data in a human-readable format, instead of in a more compressed binary format. This is because we believe that the benefit of having a human-readable format, and therefore a much greater ability to look through data and check the output, outweighs the associated memory cost (around a factor of 10 or so), especially given that any memory reduction attained due to such a format change wouldn't alter what was feasible in terms of what we can afford to store.

4.3 1D Calculation Results

Most of the calculations we have performed are for the 1-dimensional version of the SPM. As we have already performed calculations relating to 1D behaviour in

Ch. 2 and Ch. 3, we already have results which can be compared directly to our Monte Carlo calculations; thus, we will be plotting them together wherever we feel it is appropriate.

In terms of what to calculate, we can use our previous calculations to motivate our future ones. Using Monte Carlo, we can calculate the quantities we already investigated, such as current and particle density. In addition, we can also look at the time-evolution of particular configurations, to gain insight into the mechanisms by which particles are transmitted during flow. This is something our MFT says essentially nothing about, and our TRM calculations are too small to see anything meaningful in this regard.

4.3.1 Flow Patterns

First, let's talk about these flow patterns. Of the two methods available, we have only implemented the visualisation of flow using the KMC calculations. This is because the n-fold way produces a more “realistic” trajectory for the SPM, in the sense that the trajectory is an exact reproduction of the behaviour of the continuous-time Markov system; our other method, the simpler accept-reject algorithm, should reproduce correct behaviour when long-term time averages are taken, but might behave badly over small times. For example, in this method, there is a **minimum** timescale over which **any** particle can move, which is not the case for KMC, with its random timestepping.

Whilst this random timestepping makes for a more formally correct trajectory, it does make it a little more difficult to produce visualisations of particle trajectories. Our method for overcoming this is as follows:

1. Calculate a trajectory, with whatever choice of system parameters we like. The most condensed way to do this in terms of hard memory during calculation runs is to keep track of which slots' occupancies change state at each timestep, and retaining the timestamp of each timestep.
2. From this occupancy data, we can use linear interpolation in order to assign a continuous occupancy variable to all sites at all times. Between timesteps, all sites not directly involved with a transition would have an occupancy of 1 or 0, and those involved in the transition would smoothly switch from occupancies of 0 to 1 and vice-versa.

3. We can now make a new, evenly-stepped grid of space and time. We can integrate the interpolated KMC data over the time spacings of the new grid in order to find average occupations over the specified timeframe.

Thus, we can produce a spacetime diagram which shows the motion of particle density through the system over time. Clearly this method depends upon supplying a timescale δt over which we perform our averaging; a large δt will ignore most of the specifics of the motion, whereas a very small value will reveal a system in which only one particle is moving at any given time.

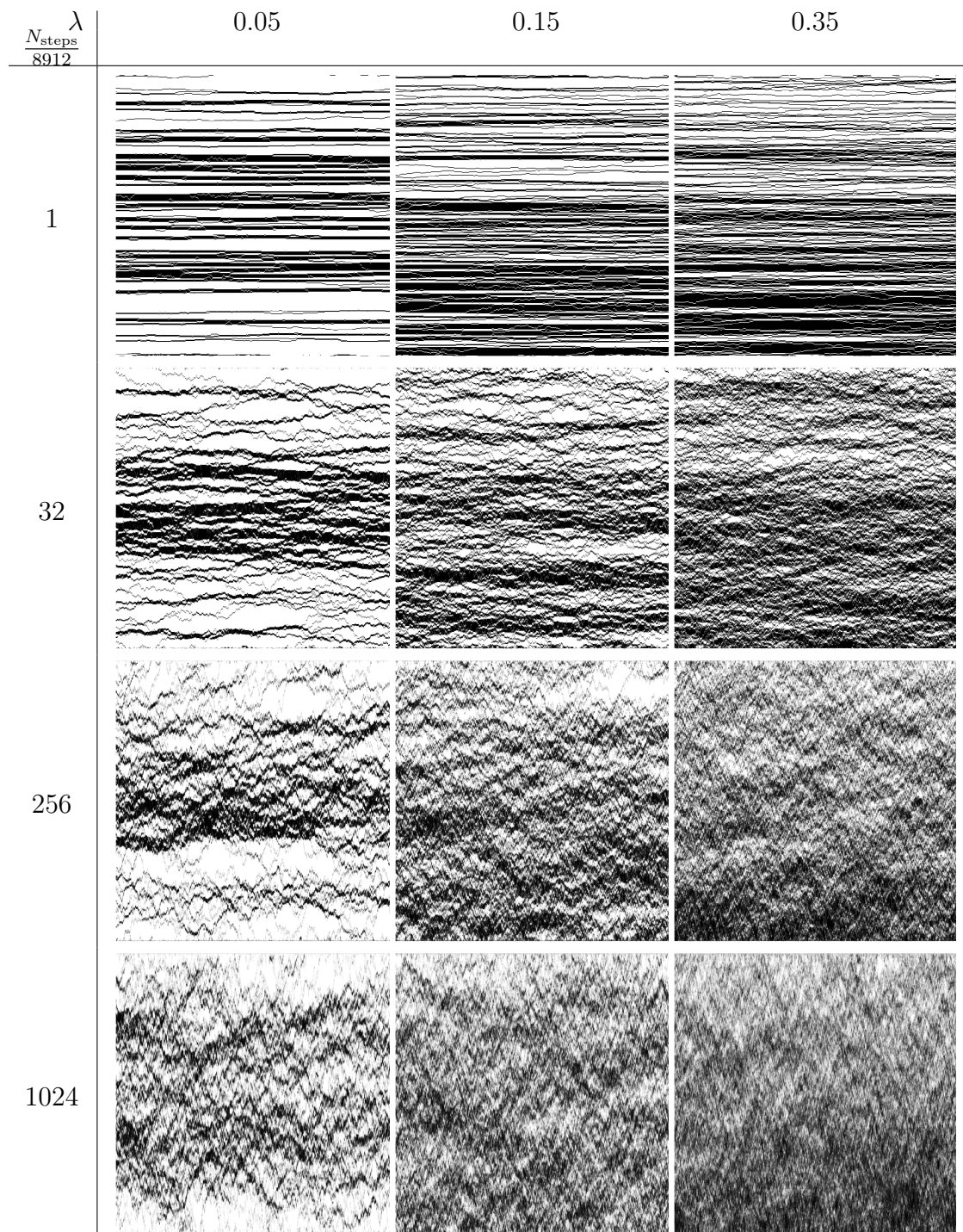
Flow Visualization for Sticky Particles

We have performed calculations which illustrate the behaviour of an SPM system in 1 dimension, displayed in Fig. 4.2. These plots were generated by simulating SPM systems with $L = 512$ and boundary conditions $(\rho_0, \rho_L) = (0.75, 0.25)$, with $\lambda \in \{0.05, 0.15, 0.35\}$. We simulated over differing numbers of KMC steps, N_{steps} , in the end performing $N_{\text{steps}} \in \{8192, 262144, 2097152, 8388608\}$ steps respectively. Once the data was collected, we could lookup the total elapsed time in each simulation, T , and then divide that time by 512 in order to obtain a discretization timescale δt , as required by our method for visualising flow patterns described above in 4.3.1. In this way, we can visualise what the flow looks like over different timescales for different values of λ . Note that the average size of a KMC step **does** depend implicitly on the value of λ ; thus, the timescales portrayed in Fig. 4.2 are not consistent between the plots, as the timesteps are multiples of lengths $\sim \{6, 2, 1\} \times 10^{-2}\text{s}$ for $\lambda \in \{0.05, 0.15, 0.35\}$ respectively. In all of these plots, dark tones represent low time-averaged particle occupation, whilst light tones represent high time-averaged particle occupation.

Each of the systems here show the behaviour of particles with low- λ , so we are in the sticky regime; however, all of our previous results indicate that there should be rather large differences in behaviour as we switch from relatively weak stickiness (here embodied by $\lambda = 0.35$) to strong stickiness (portrayed by the $\lambda = 0.05$ situation). The images used to create Fig 4.2 are relatively high-definition, which should enable readers using the digital copy to zoom in order to see the fine details. Our principle observations are as follows:

- At the shortest timescale, one can quite clearly see the motions of individual particles. As one might expect, they are less likely to be seen unbound

Figure 4.2 Spacetime plots of the particle flow in 1 spatial dimension, as described in 4.3.1. In each case, the *x-axis* represents **time** and the *y-axis* **space**. The higher-density boundary is the one at the top of each image. Dark tones indicate low particle density, light tones high.



from neighbours in the lower- λ systems than the higher- λ ones. In the low- λ regime, we are much more likely to see big blocks of particles, possibly containing a low concentration of mobile vacancies. Between these blocks we have a dilute “gas” of usually individual particles.

- Focussing now on the $32\times$ longer intermediate timeframe, we can see that in the extremely low- λ situation we have blocks of particles separated by voids of vacancies. These voids contain a dilute gas of particles. Over these longer timescales, we see that the blocks of particles do in fact slowly migrate around the system, occasionally breaking apart or reforming during their travels. Also notice that the voids are more likely to be found towards the centre of the system than adjacent to the boundaries. The chemical potential (Fig 2.3) for small- λ is minimised for high density, thus a boundary held at any density should be expected to in practise generate a high local density regardless of the density it is set to emulate; as we move away from the boundary its correlations with the interior weaken, so we think that the accumulation of particles on the boundary is an edge effect with a certain depth, and that the situation towards the centre of the system is more representative of the preferred bulk behaviour.
- Meanwhile for higher- λ , we see a “tissue paper” pattern over these intermediate timescales; the system is similar to a gas of randomly-walking particles, but there is a little bit more short-range correlation than that, hence the observed texture in the image.
- Now looking over longer timescales, we see that for the lowest- λ it is in fact the case that the voids towards the centre of the system do in fact appear and disappear over time. Given that we know that there are still (small) flows occurring in this regime (see Sec. 4.3.2), it is likely that when these voids are created and destroyed, there are small overall biases in terms of which void boundaries more particles are extracted from or shed into. We suspect that this is the primary mechanism by which transport across the system is achieved in this regime. Meanwhile, the higher- λ systems are becoming something closer to a continuous grey gradient from the top boundary to the bottom, suggesting that the overall transport is more diffusive in nature.

Repulsive Particles

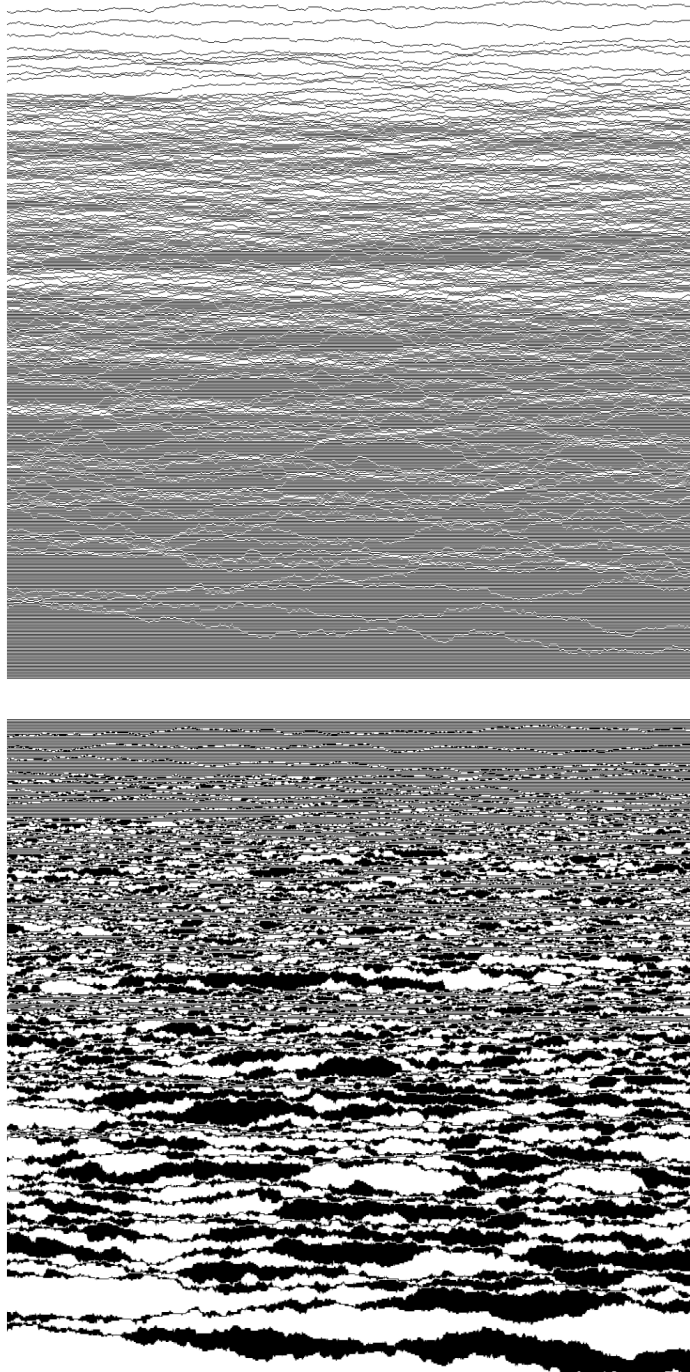
Of course, we can do similar calculations with repulsive particles, for which $\lambda > 1$. Of the most interest is the extreme case in which $\lambda \gg 1$, when we should expect that particles have an almost explosive tendency to separate if brought together. We have performed such a calculation, with results displayed in Fig 4.3, with a system of length $L = 1024$, $\lambda = 10^6$ and $(\rho_0, \rho_L) = (0.99, 0.01)$, for which we performed 40960 KMC steps. The time slices used in the plot are of size 2×10^{-7} s.

As before, time goes from left to right, space from top to bottom. The top plot displays the time-averaged density shaded the normal way (light being dense, dark being empty). The bottom plot displays the same information, only this time we have applied the function $f(x) = 1 - x$ to the density at every other site as we move along the spatial axis; thus we reveal that in this limit our system is partitioned into domains, in the same way that an antiferromagnet might be. The boundaries between these domains can move quite rapidly, and the motion of such a domain wall corresponds to the transport of a particle; thus we think that it is this domain boundary motion which controls the rate of transport in this regime.

4.3.2 Scans Through λ with Constant Boundary Densities

We can perform calculations in which we hold all things constant except λ , analogous to our existing calculations done using our TRM and MFT results. In these calculations, we computed the properties of systems with boundary densities $(\rho_0, \rho_L) = (0.3, 0.1)$, $(0.75, 0.25)$ and $(0.9, 0.7)$, using both the evenly-timestepped Monte Carlo method and KMC. In this case, our KMC calculations used systems of size $L = 64$, whilst our other method used systems of size $L = 100$. To account for the different system sizes used, we have rescaled the current and its moments, whilst leaving most other quantities such as particle density as they are. In the case of current, we have multiplied by L in order to achieve this normalisation; this is because a normal diffusive current is driven by concentration gradient, therefore if we use the same concentration difference we should expect the resulting current to vary as $J \sim L^{-1}$. Note that for our KMC calculations we performed initial equilibration runs of 4000000 steps, followed by 1000 of our alternating analysis/relaxation passes of 16000 steps each way;

Figure 4.3 Spacetime plot for a system of repulsive particles. As before, time increases along the x -axis and space along the y -axis. The top plot displays the time-dependent density using the normal shading scheme (white is full, black is empty, grey indicates partial occupation). In the bottom plot, we invert the shading scheme every other site; thus, regions populated with alternating particles and vacancies are now displayed as solid blocks, with the moving boundaries between those blocks being domain walls.



thus, this should provide us with decent quality data, at least until λ becomes so small that particles can barely move through the system. Our evenly-timestepped calculations were performed with 10000 equilibration steps followed by a single measurement run of 100000000 steps, so we aren't calculating the other moments of the current using that method.

Mean Current

Fig. 4.4 displays the variation of the current with λ . Here, the dashed lines correspond to the MFT predictions, the joined circles to TRM-computed results, the triangles to results computed using evenly-timestepped Monte Carlo and the crosses to KMC calculations. Fig. 4.5 displays the same data, but over a wider range of λ values. We have already discussed the TRM results and their relation to the MFT results back in Sec. 3.3.3. Our main observations about the current are as follows:

- At large λ the current seems to vary in proportion to λ , in agreement with our TRM and MFT results. The actual constants of proportionality don't quite match, which is a common issue in all of these results. We have seen in Sec. 4.3.1 that there is usually a boundary layer of excess particles or vacancies next to both boundaries, thus it is possible that this issue arises from this boundary layer causing the current to not scale with L in quite the way we expect. However, this is something we can check by varying the system size and checking the current variation with λ , as we have done in Figs.4.7.
- For $\lambda \in (0.01, 0.3)$, the current undergoes power law variation with λ , again in agreement with our TRM calculations, with $J \propto \lambda^3$.
- For smaller values of λ , the observed mean current starts to become noisy, at least in the logarithmic plots, and essentially saturates to a low value. Our interpretation of this is that for these extreme low values of λ the current signal becomes extremely weak, as it begins to depend on the motions of extremely small overall numbers of particles during the measurement period; thus, in that regime the current is dominated by a form of shot noise, and so it becomes difficult to measure the current accurately in this regime.

Figure 4.4 The mean current observed to flow from a boundary with greater particle density to lesser particle density in 1D. Here the boundary densities are held constant throughout, whilst λ is varied. The lower plot is the same data as the upper one, but with logarithmic axes instead of linear ones. The dashed lines correspond to the MFT predictions, the joined circles to TRM-computed results, the triangles to results computed using evenly-timestepped Monte Carlo and the crosses to KMC calculations. Note that we do not have reliable error estimates for the evenly-timestepped Monte Carlo calculations.

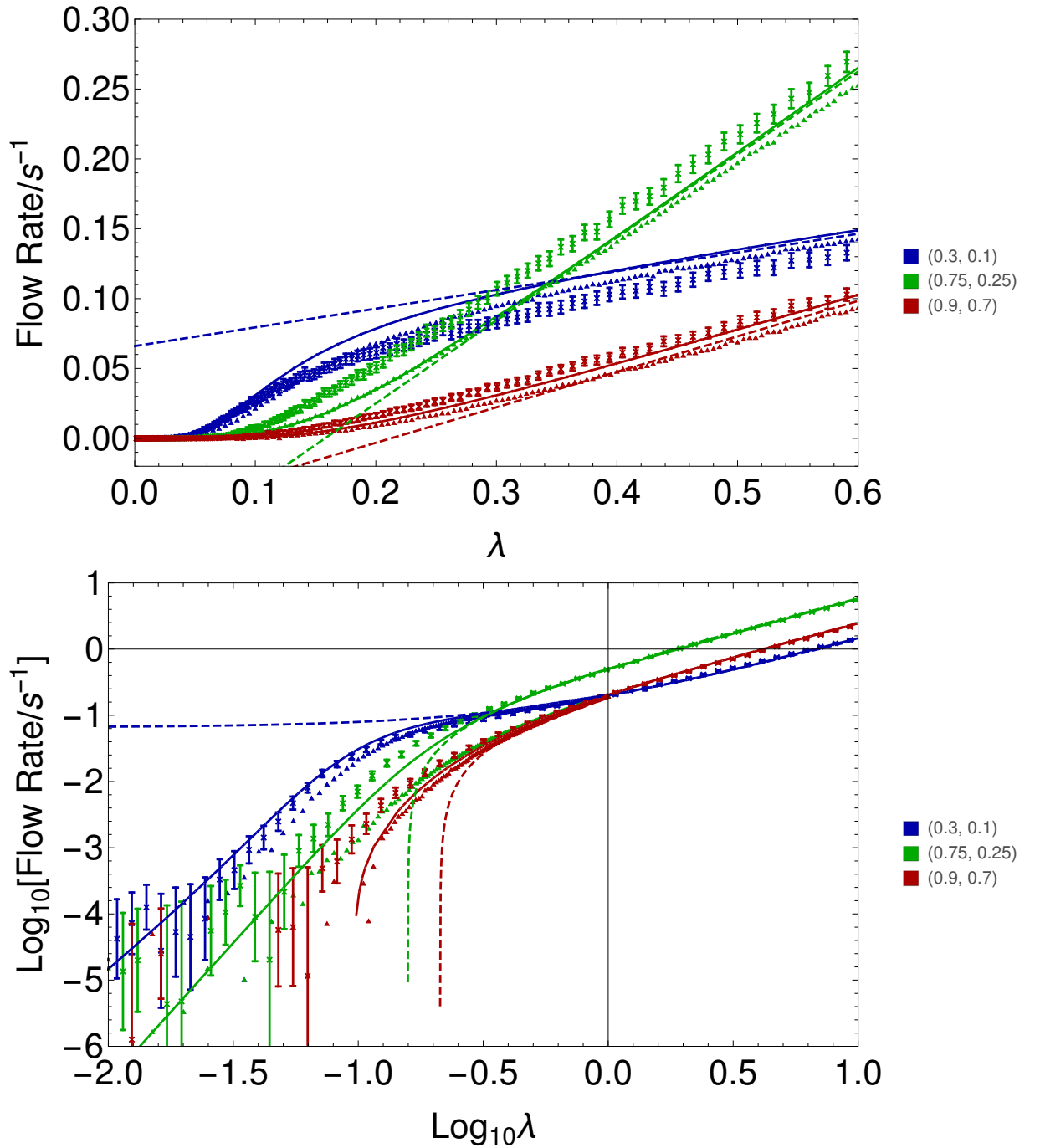


Figure 4.5 As the logarithmic plot in Fig. 4.4 but over a much wider range of λ -values.

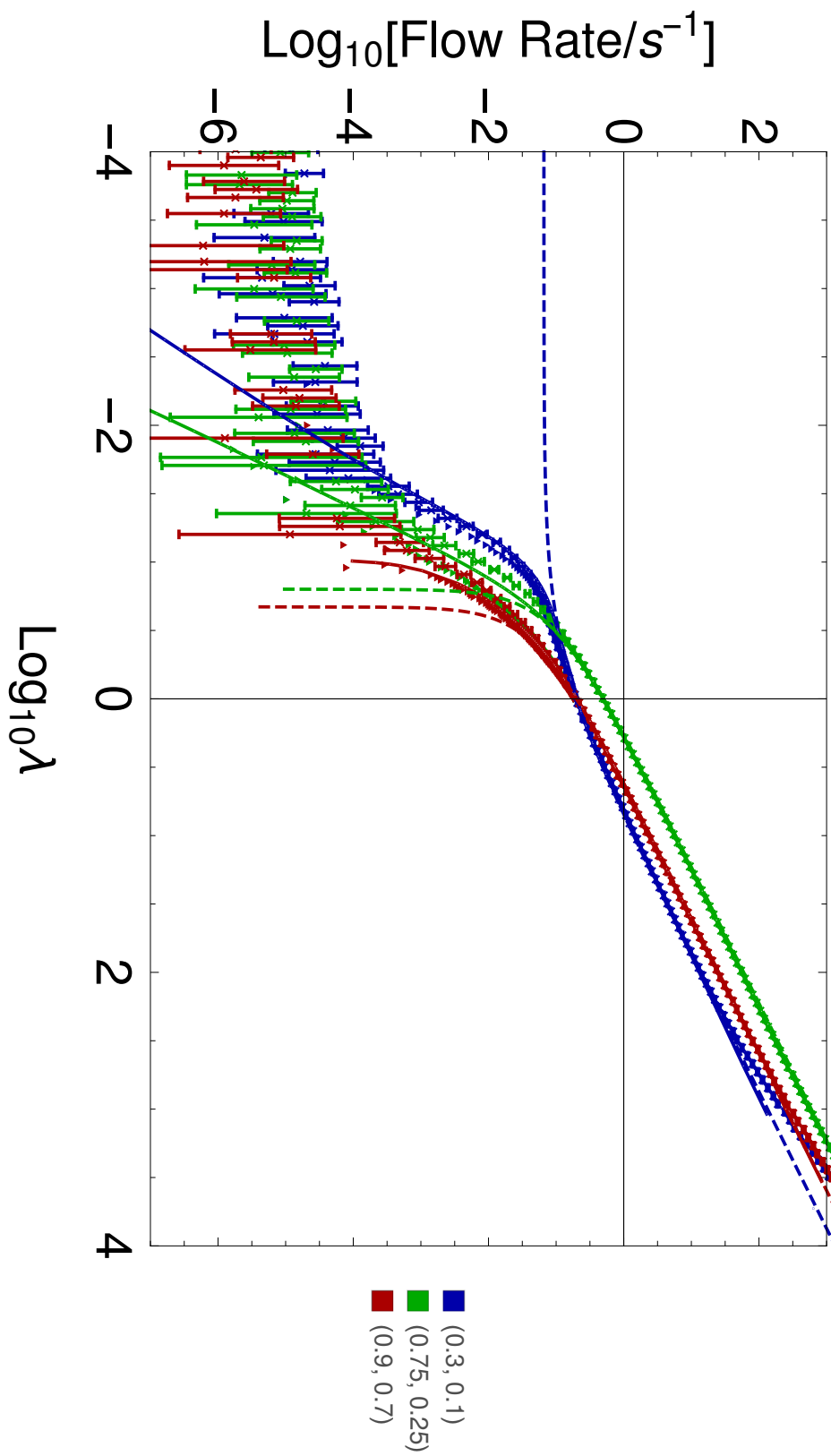
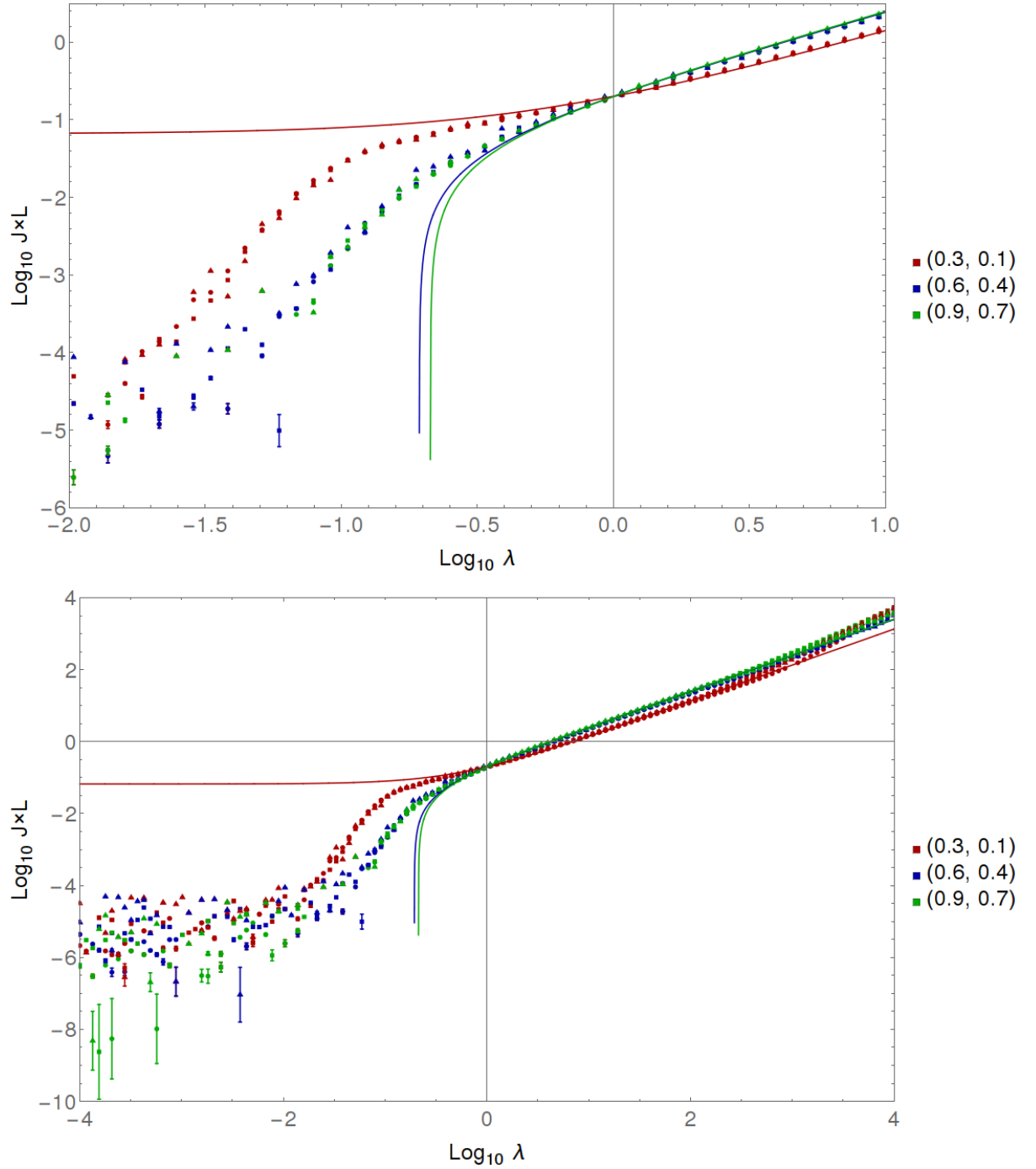


Figure 4.6 As Fig 4.4, but we are now comparing Monte Carlo results from systems of different size instead of the other calculation methods. Here, **circles**, **squares** and **triangles** represent systems of size $L = 32, 64$ and 128 respectively. The currents computed have been normalised via multiplication by L . Note that all error bars are present; when invisible, this suggests that they are smaller than symbol size. We believe that the errors for the extreme low- λ regime are underestimates, due to the systems not having had time to fully equilibrate. MFT results are displayed for comparison as solid curves.



Thus, we still seem to see the same “transition” we saw when analysing TRM results. To ensure that this behaviour in the current isn’t just an artefact of system size, we can vary the system size whilst measuring the current, as we have done in Figs. 4.6 and 4.7.

Here we see that our method for normalising currents for different system sizes actually seems to work quite well, at least over the system sizes we are looking at. It also indicates that our choice of $L = 64$ behaves well until $\lambda < 0.05$, at which point the fluctuations start to become very large compared to the observed mean current.

An important thing to note here is that the critical λ at which the “transition” occurs does **not** seem to be sensitive to the system size. Similarly, the λ at which the results “plateau” and reduction in λ no longer meaningfully reduces the current also depends very weakly upon system size, if at all. This plateau is presumably due to the flow becoming so slow that the number of particles moving in and out of the system over a given timeframe is becoming so small that it becomes very susceptible to noise, and so when we plot logarithmically we see the plateau with many results scattered under it.

Current Higher Moments

Using our KMC calculations, we can also compute the higher moments of the current. As we do not have any particular theory which predicts these higher moments, we do not have very much to say about these results, other than simply stating what we see. It is worth noting that we don’t detect divergences in these moments around the bend of our “transition”, therefore it does not seem to be a transition in the traditional phase transition sense, as there we would expect to see discontinuities in observables, and here current is the kind of observable we should expect to manifest that kind of behaviour. These moments, up to and including the current kurtosis, are displayed in Fig. 4.8. Note that no units for skewness and kurtosis are listed as they have already been normalised using the scale set by the variance.

There’s a little bit of a bend in the variance as we go through the transition, but nothing major. Skewness is typically positive but fluctuates a lot, and goes negative past certain thresholds at large λ . Kurtosis is bounded and possibly negative for λ above the transition threshold, then starts growing large and

Figure 4.7 Calculations of the dependence of current upon λ , repeated using KMC with different system sizes as indicated. Here we have focussed on the boundary setup $(\rho_0, \rho_L) = (0.75, 0.25)$ and region $\lambda \in (0.04, 0.25)$, which constitutes the bend in our supposed transition. Standard errors in the current were computed using observed current variances. The fact that the errors seem to increase with system size suggests that the larger systems are fluctuating more due to poorer equilibration.

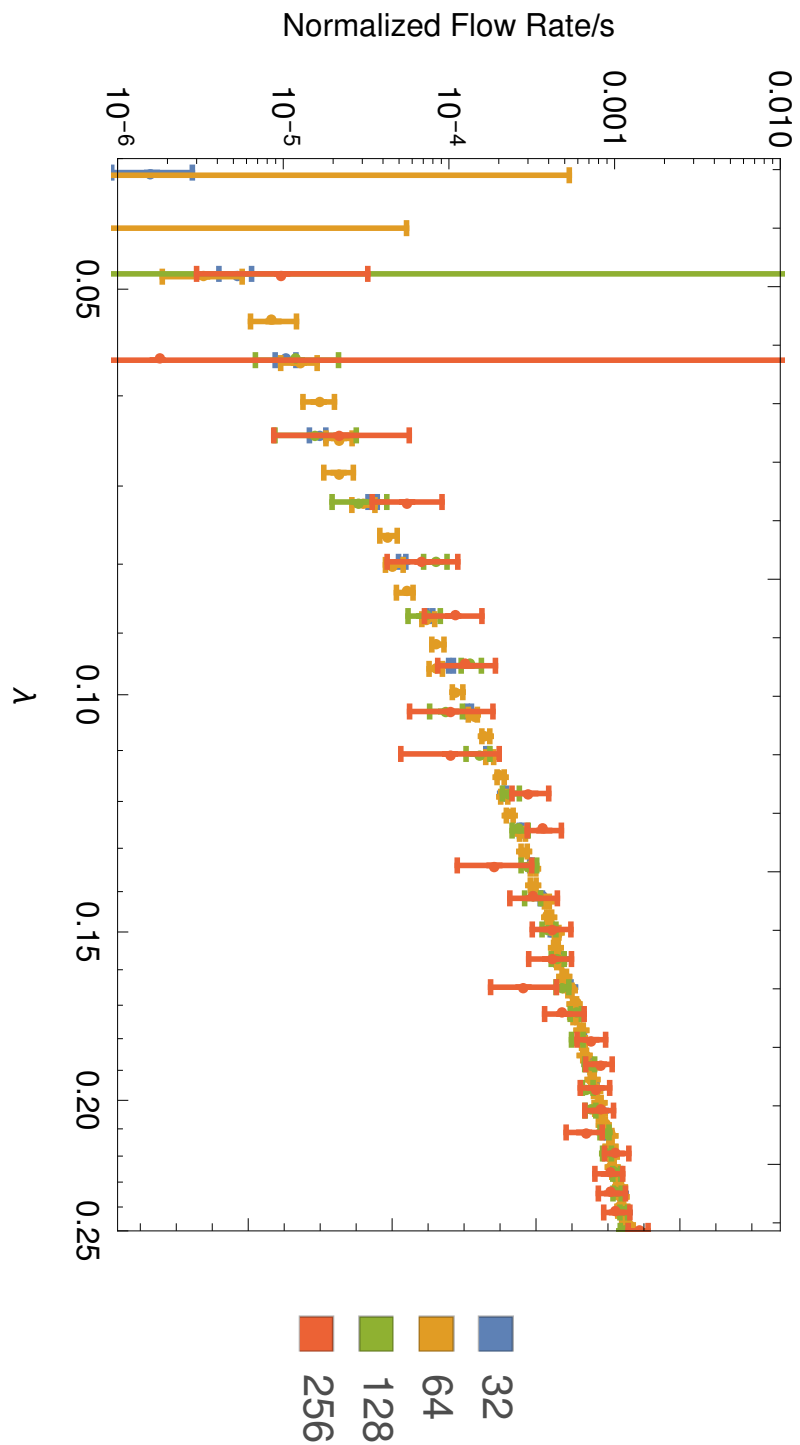
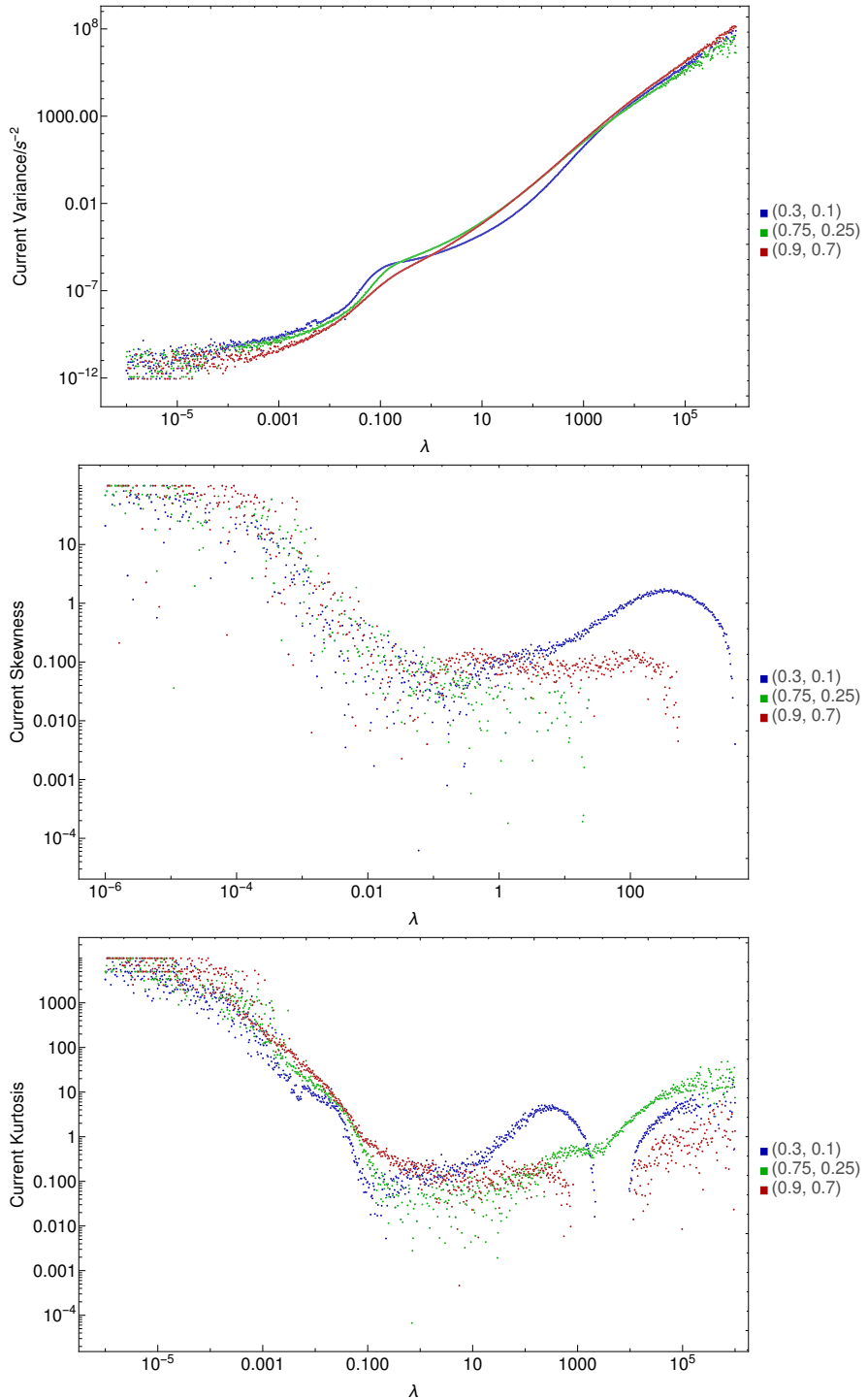


Figure 4.8 The higher moments of the current, measured using KMC in the same setup as used in Fig. 4.4. Note that we do not have reliable error estimates for these quantities, as their computation would require good knowledge of these same higher moments; given the already dubious quality of the skewness and kurtosis readings (which one can assess visually from the spreading of nearby points on the graph), we can't make a proper assessment of the error in the variance.



positive as we go through the suspected transition. Thus, we have several different pieces of weak evidence of something happening in the transition region, but nothing clear and conclusive like a spike or discontinuity.

Overall Density

In addition to measuring current and its moments, we can measure the mean overall density of particles in the system. We did this using the same system parameters as in Fig. 4.4; the variation in this mean density with λ for different boundary conditions is displayed in Fig. 4.10.

The most striking feature here is how the densities converge for extreme values of λ regardless of the actual boundary conditions used, converging to 1 for extremely small λ and to around $\frac{2}{3}$ for extremely large λ . The behaviour seen here is in accordance with our existing computations as seen in 3.3.3, and our theory about this is as expressed there: in short, that at small λ , high density is favoured for “energetic” reasons (the attempted minimisation of equilibrium free energy), whilst at very large λ our system self-organises to have a density of $\sim \frac{2}{3}$ in order to enable maximal flow to occur due to a stability argument.

We can also measure the variance of the densities we observed, and use this to gauge the size of the density fluctuation, $\text{Var}(\rho) = \text{Var}(N)/L$, where N is the number of particles in the system. In the results displayed in Fig. 4.9, we have computed the density fluctuation in our 1D SPM system with boundary conditions $(\rho_0, \rho_L) = (0.6, 0.4)$, using the evenly-timestepped Monte-Carlo method. Here we have calculated this fluctuation for systems of various different sizes, and then normalised the fluctuation via multiplication by system size. Note that we have two datasets for $L = 400$ as we used two different numbers of timesteps to see what impact it had; it would appear that this impact was quite negligible.

As this causes the points to generally align for $\lambda > 0.3$, this suggests that in that regime the dependence of $L \times \text{Var}(\rho)$ upon L is pretty weak; therefore, the density fluctuation scales as $\mathcal{O}(L^{-1})$, implying that the number of particles in the system fluctuates as $\mathcal{O}(1)$, which makes perfect sense when you consider that the system allows particles to enter and leave the system only at the two boundaries, which do not change with the system size in any sense. We also observe that there is a visible bump as we pass through the suspected transition, but as with our

Figure 4.9 The variation of the fluctuation of the density observed in the SPM system with λ for different boundary conditions, in 1D. Error estimates are not available due to our inability to reliably calculate higher moments. This variance is normalised via multiplication by the system size L .

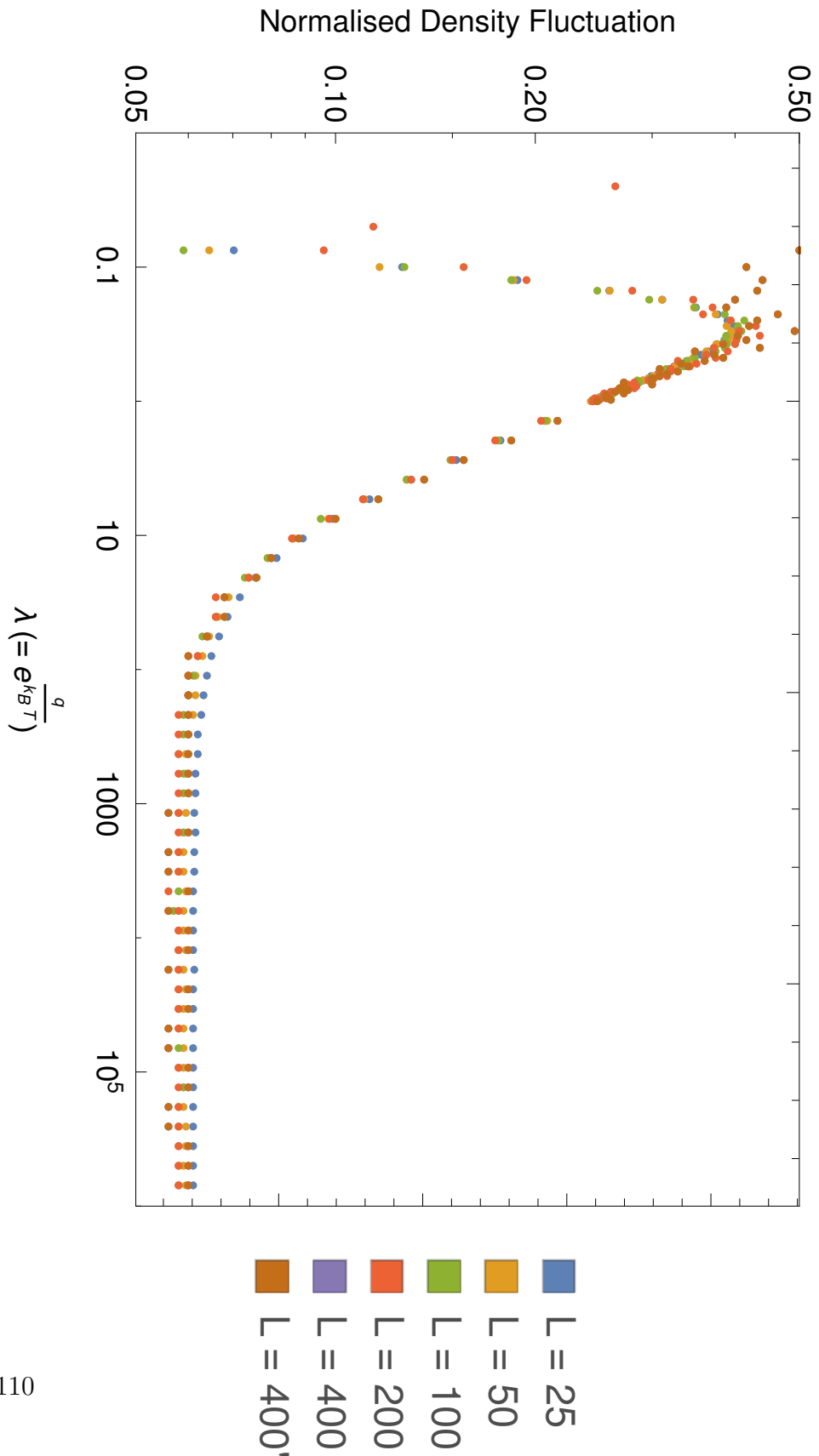
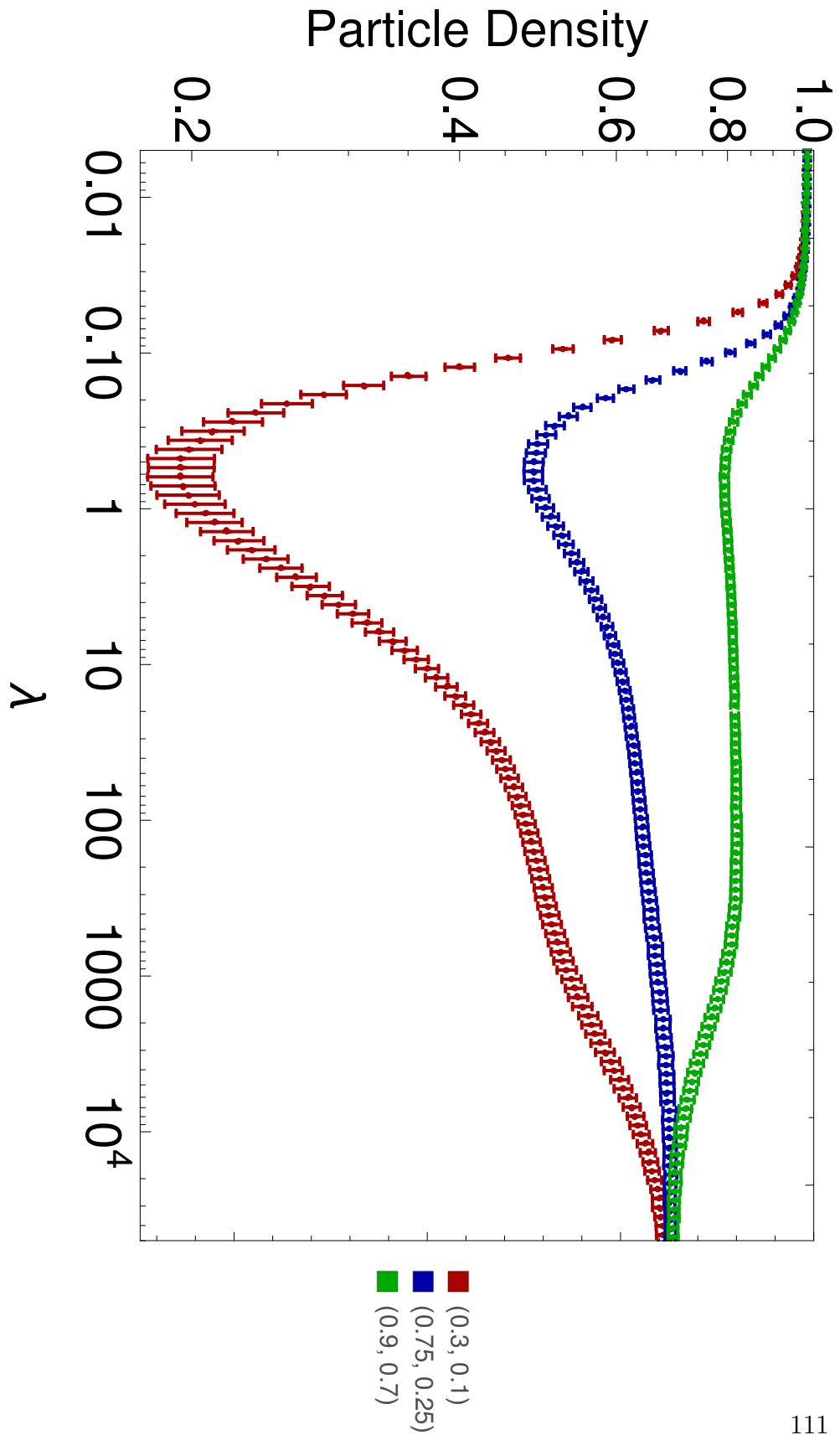


Figure 4.10 The variation of the overall mean density of the SPM system with λ for different boundary conditions, in 1D. Setup is the same as in Fig. 4.4.



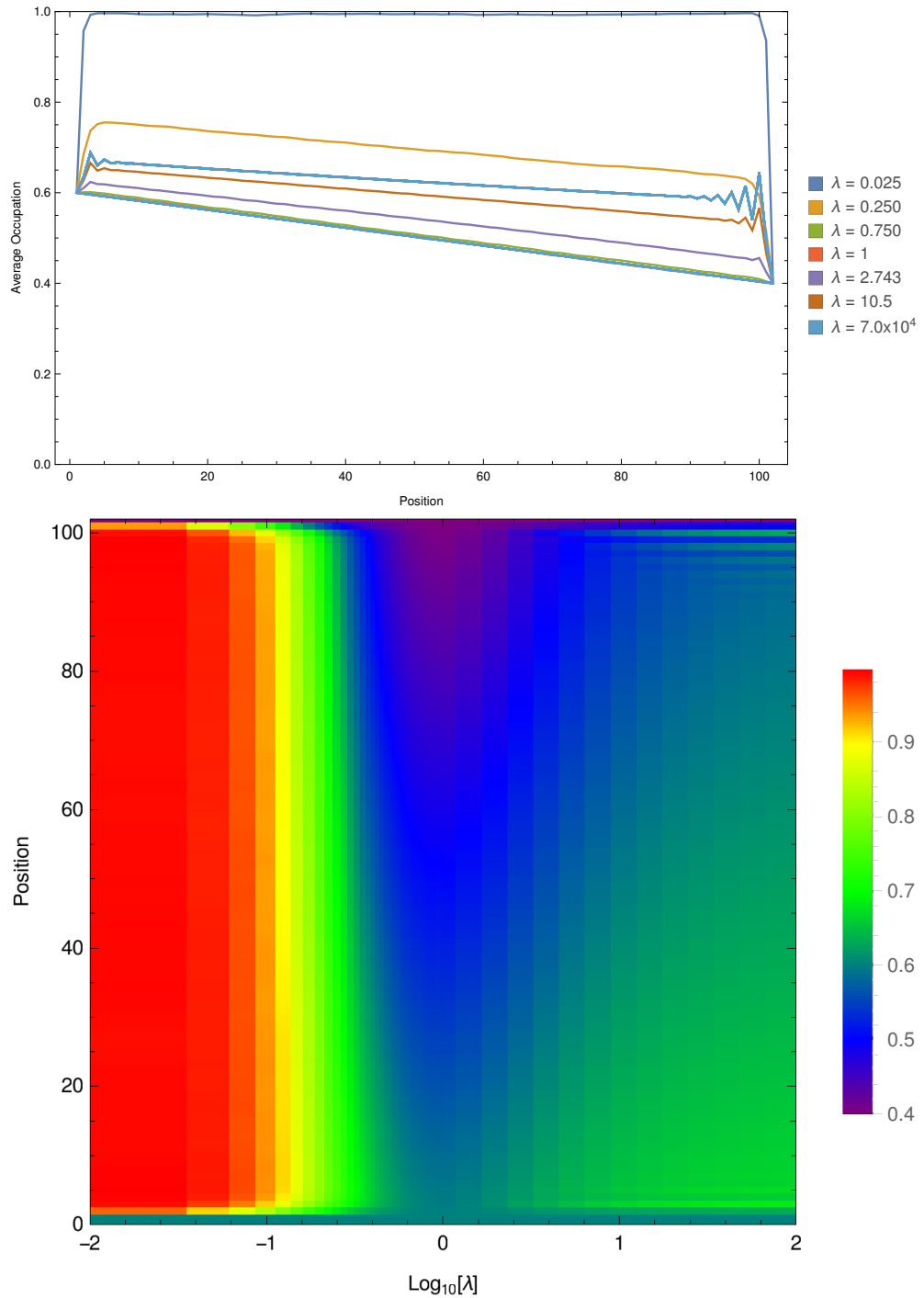
higher current moments it is not a spike or discontinuity. We also observe that for the smaller systems the fluctuation comes back under control as λ keeps getting smaller, whilst for larger ones the fluctuations remain large. We suggest that this is due to the fact that we have observed the fluctuations over some timescale; thus if the system is undergoing long, slow fluctuations over timescales longer than our observation frame, we will underestimate these fluctuations. This is in essence a “time to equilibration” error, in the sense that the system’s equilibration timescale is longer than our observation timescale, and this informs us that we should be dubious about our larger- L results once we get into the extremely small λ regime.

Time-Averaged Density Profiles

If we use the same methodology as in Sec. 4.3.2, but instead take long-term time averages, we can compute the time-invariant average occupation of particular sites for a system with given λ and boundary conditions. In Fig. 4.11 we show how this density profile changes with λ for fixed boundary densities $(\rho_0, \rho_L) = (0.6, 0.4)$. We see some general trends:

- For $\lambda = 1$ and other nearby values, the density profile is a smooth, flat descent from the high density to the low density.
- For very small λ , the system nearly fills, except for just around the boundaries (where particles are still quite free to move in and out of the system).
- For very large λ , the system adopts another flat gradient in the bulk, but this time interpolating between densities higher than the boundary densities we used in this case. In addition, there are also oscillations observed near to the boundaries. Due to the small standard errors estimated, we are quite sure that these are not calculational artefacts, and are in fact caused by a combination of the extremely repulsive nature of the particles and the order which is being imposed by the boundaries themselves. This effect is consistent with our TRM results displayed in Fig. 3.8.

Figure 4.11 Time-averaged density profiles for systems with fixed boundary densities $(\rho_0, \rho_L) = (0.6, 0.4)$, over a range of λ . Here the system size used is $L = 100$. The top plot shows the density profile with a selection of λ values coded by colour. The bottom plot shows a coloured density plot showing the continuous variation of the time-averaged profile with λ . Note that the standard errors on these densities are very small compared to 1 (the maximum density), so error bars are not displayed.



Block Size Distribution

The final type of measurement we have recorded in this “ λ -scan” series of calculations is the distribution of block sizes. By this we mean that we observe how many contiguous runs of 1, 2 and so on particles there are and add these to a time-weighted histogram, as per our method outlined in Sec. 4.2.2. If we do this, again using our run parameters from Fig. 4.9, we find that the mean block size and its standard error vary as shown in Fig. 4.12.

Here we once again see that we have convergence in the large- λ limit, to an average block size very close to 2 which is in line with our ideas about maximal transport with a density of $\frac{2}{3}$. As we go towards $\lambda = 1$, we find that the block size distribution reverts to that which we’d expect by just randomly arranging particles with given densities, which is essentially what is happening in SEP. As we go through the transition, the mean block size suddenly takes off, whilst the fluctuation in the block size peaks, before once again starting to reduce. Once we get to very small λ , we lose the signal in noise, in a similar way to how we see all our results become noise-dominated in the extremely small λ regime.

4.3.3 Varying λ and Boundary Density Difference Together

Another type of calculation we can perform is one in which we hold the average of the boundary densities constant, whilst varying their difference and λ ; we can do this by using boundary conditions $(\rho_0, \rho_L) = (\rho + \frac{1}{2}\delta\rho, \rho - \frac{1}{2}\delta\rho)$ and varying $\delta\rho$ whilst keeping ρ constant. In our calculations of this style, we set $\rho = \frac{1}{2}$, $L = 64$, performed 400000 equilibration steps and then 1000 alternating measurement and relaxation runs of 16000 and 1000 steps respectively. From this we calculated the same kinds of quantities as in Sec. 4.3.2; the principle results are displayed in Fig 4.13.

In each of these results, we see that we essentially partition the domain into two regimes: small λ with small $\delta\rho$, and another regime where λ is larger, or $\delta\rho$ is bigger. In other words, when λ becomes small the system gains density, block size, and flow slows; however, a large boundary difference can still force through current and keep density and block size lower, so there is a tradeoff between these competing forces.

Figure 4.12 The mean block size, calculated using KMC with the same run parameters as we did for Fig. 4.4. Note that the error estimates here are plotted, and are presumably underestimates for extremely small λ .

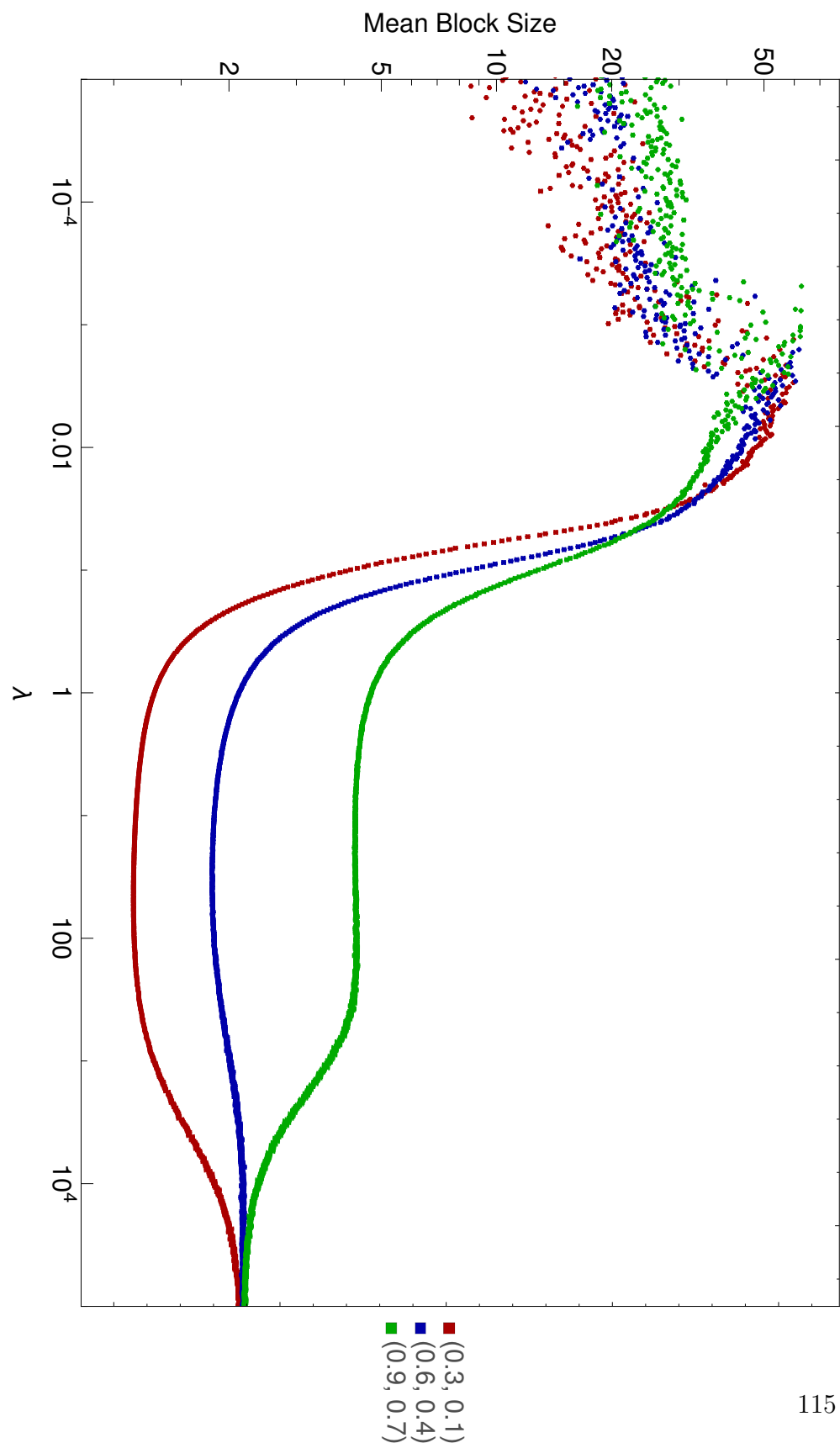
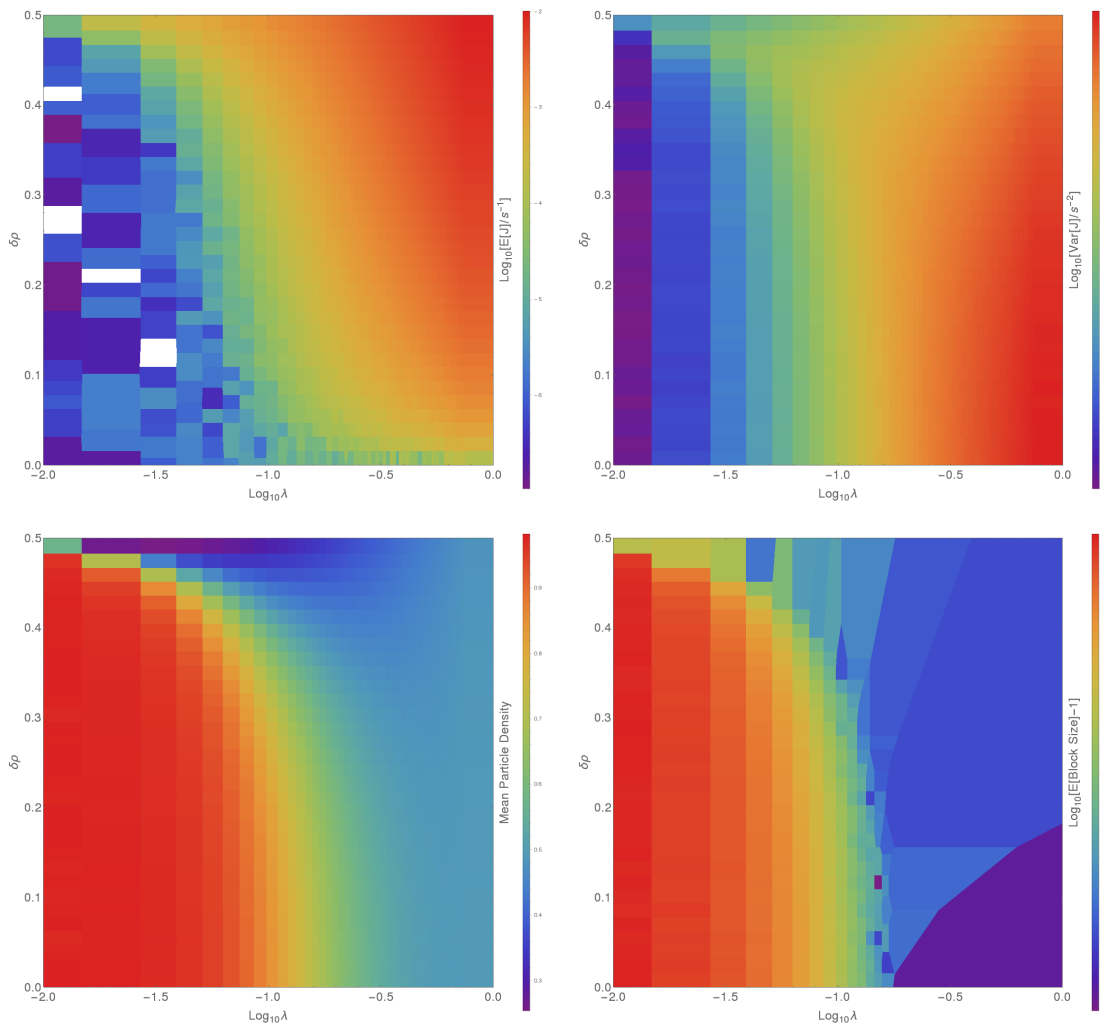


Figure 4.13 The main results obtained when we have boundary densities $(\rho_0, \rho_L) = (\rho + \frac{1}{2}\delta\rho, \rho - \frac{1}{2}\delta\rho)$ and vary λ and $\delta\rho$. Here $\rho = \frac{1}{2}$. Clockwise from top left, we have: The mean current, the current variance, the mean block size, and the mean overall system density. Note that in our mean block size computation, many calculations failed; this explains the sparsity of the data in the right of the image.



4.3.4 Varying the Boundary Densities with Constant λ

Instead of varying λ , we can instead choose to hold it constant whilst we vary the two boundary densities. We have done this with a series of different λ ; the mean current results are displayed in Fig. 4.14, and the mean densities displayed in Fig. 4.15. Here we used $L = 124$, with 160000000 equilibration steps and then 1000 sets of analysis runs of 1600000 KMC steps interspersed with relaxation runs of 1000 steps.

We see a similar picture to the one we saw in Sec. 4.3.3; the system naturally wishes to relax to a high-density, low-current regime at small λ regardless of boundary conditions, (probably primarily due to attempts to minimise free energy), but this is suppressed by large boundary density differences. It is also important to note that Fick's Law is violated in every case here, as one can see by the fact that the colour gradients are not constant along lines of constant $\rho_0 + \rho_L$.

4.3.5 Diffusion Coefficient

Wrapping up our calculations in 1D, we can compute the effective diffusion coefficient, which can be compared with our existing calculation in Sec. 3.3.3 (see Fig. 3.10 specifically for graphical comparison). To do this, we perform calculations with boundary densities $(\rho_0, \rho_L) = (\rho + \frac{1}{2}\delta\rho, \rho - \frac{1}{2}\delta\rho)$, where we vary ρ , λ and $\delta\rho$ simultaneously, and we deliberately keep $\delta\rho$ small, in the hope that the dependency of the current upon $\delta\rho$ is roughly linear in that regime, so that $J = \frac{\delta\rho}{L}D(\rho, \lambda) + \mathcal{O}(\delta\rho^2)$. Given that we have an error estimate for J due to repeat runs, we can use weighted least squares fitting to estimate the value of $D(\rho, \lambda)$, and also its error. We did this, using 16 values of $\delta\rho$ for each (ρ, λ) pair we computed (arranged in a 24×12 grid); each computation consisted of a 160000000 KMC step equilibration run, followed by 10 alternating 80000000 step measurement run and 16000000 step relaxation run pairs. The system size used in this case was $L = 124$. Our estimates for D and its standard error are displayed in Fig. 4.16. Additionally, we performed similar calculations with a wider range of λ and different system sizes, which are displayed in Fig. 4.17.

Please note that whilst this is probably the largest single calculation we have performed during the course of this research, it is also the earliest chronologically; thus, there are many issues with it:

Figure 4.14 Here we have varied ρ_0 and ρ_L separately for several different values of λ , and measured the resulting mean current. Note that here we have plotted the absolute value of the current, as it should be antisymmetric about $\rho_0 = \rho_L$, which would not take kindly to having its logarithm taken. White patches indicate measurements which are out of bounds, generally because they were too large, whose incorporation would have negatively affected the usefulness of the graph.

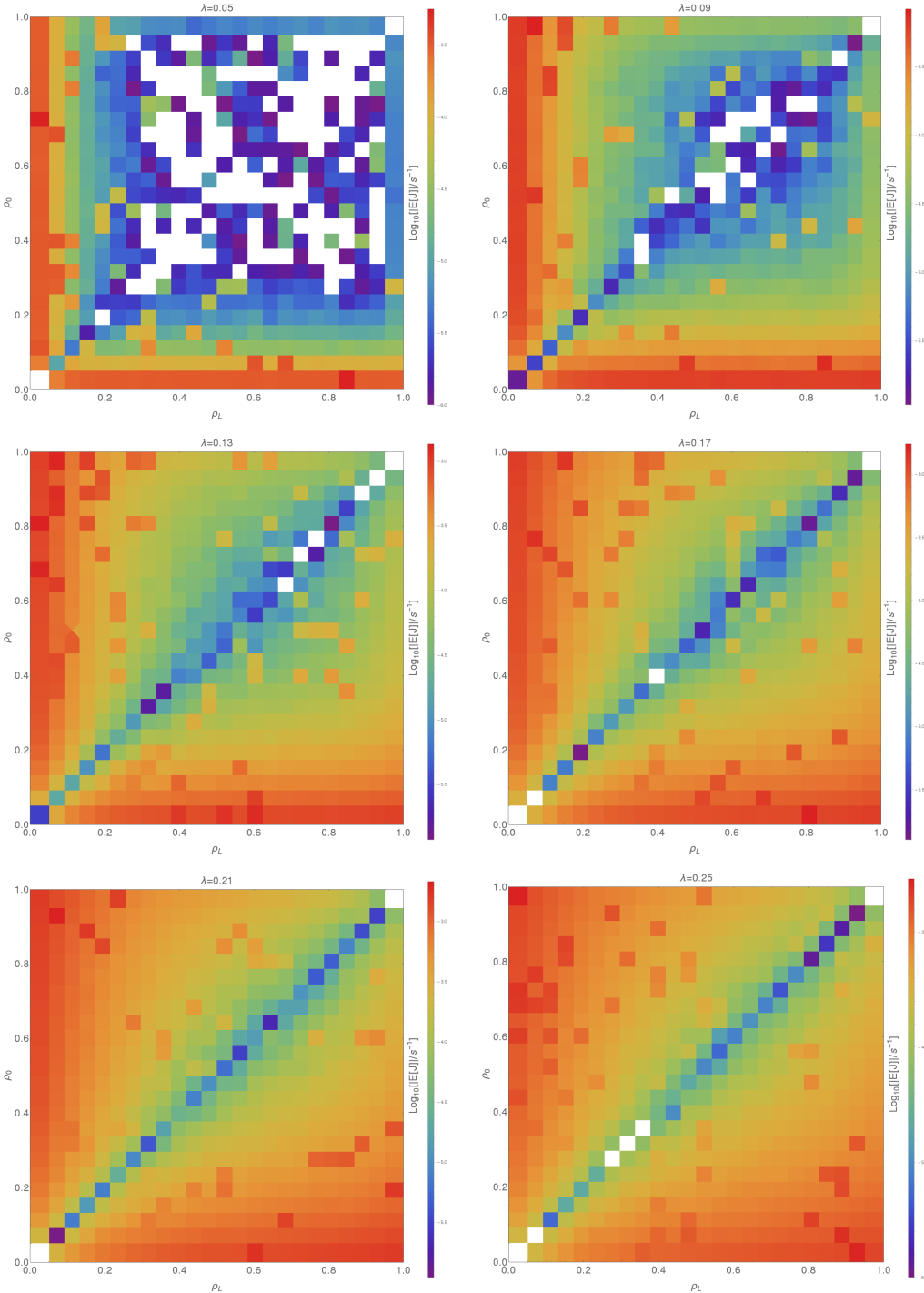


Figure 4.15 As Fig. 4.14, only this time we have plotted the mean densities instead of the currents.

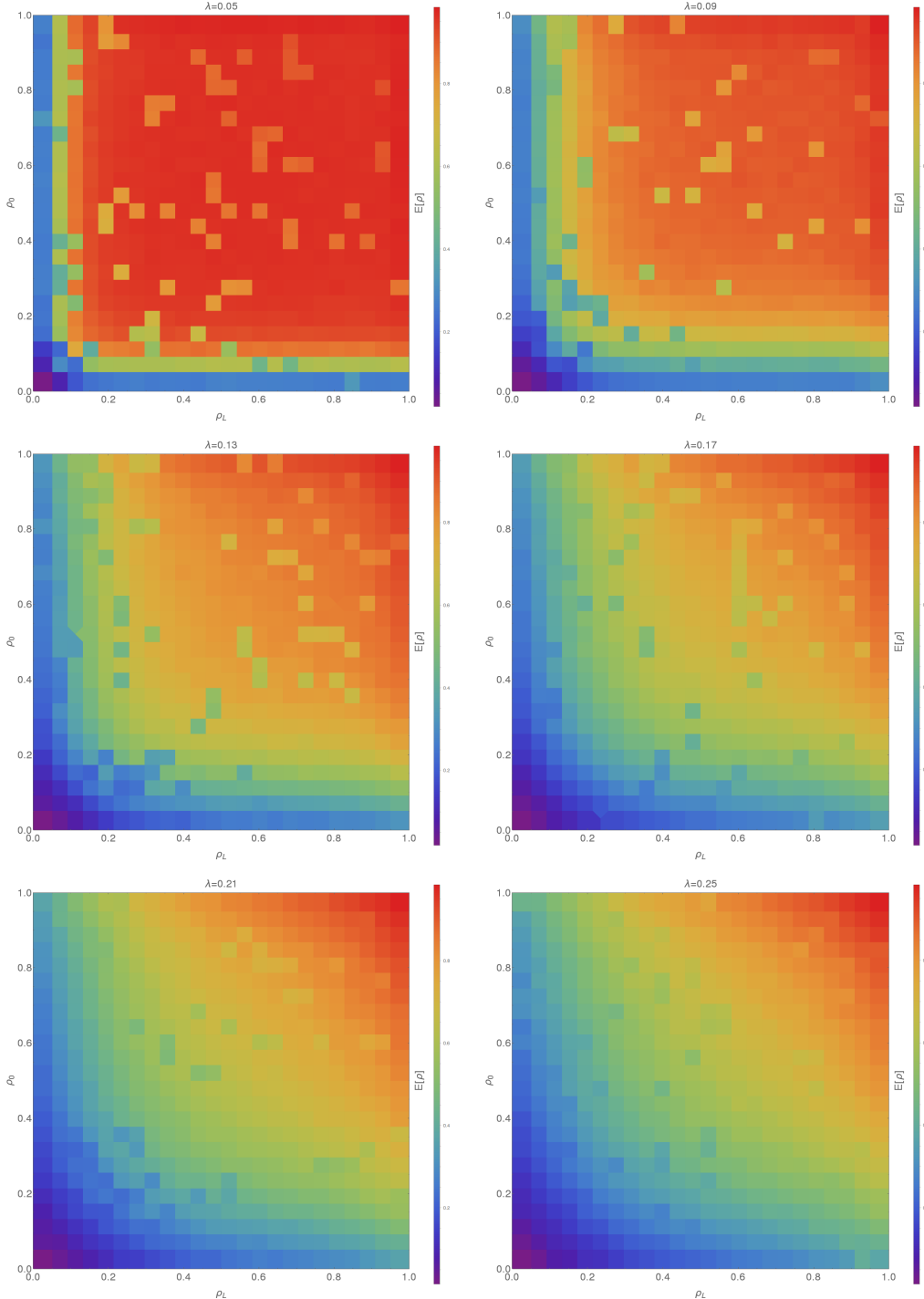


Figure 4.16 The variation of the KMC-calculated diffusion coefficient with ρ and λ . The top panel is the estimate of $D(\rho, \lambda)$, and the bottom panel is the associated standard error.

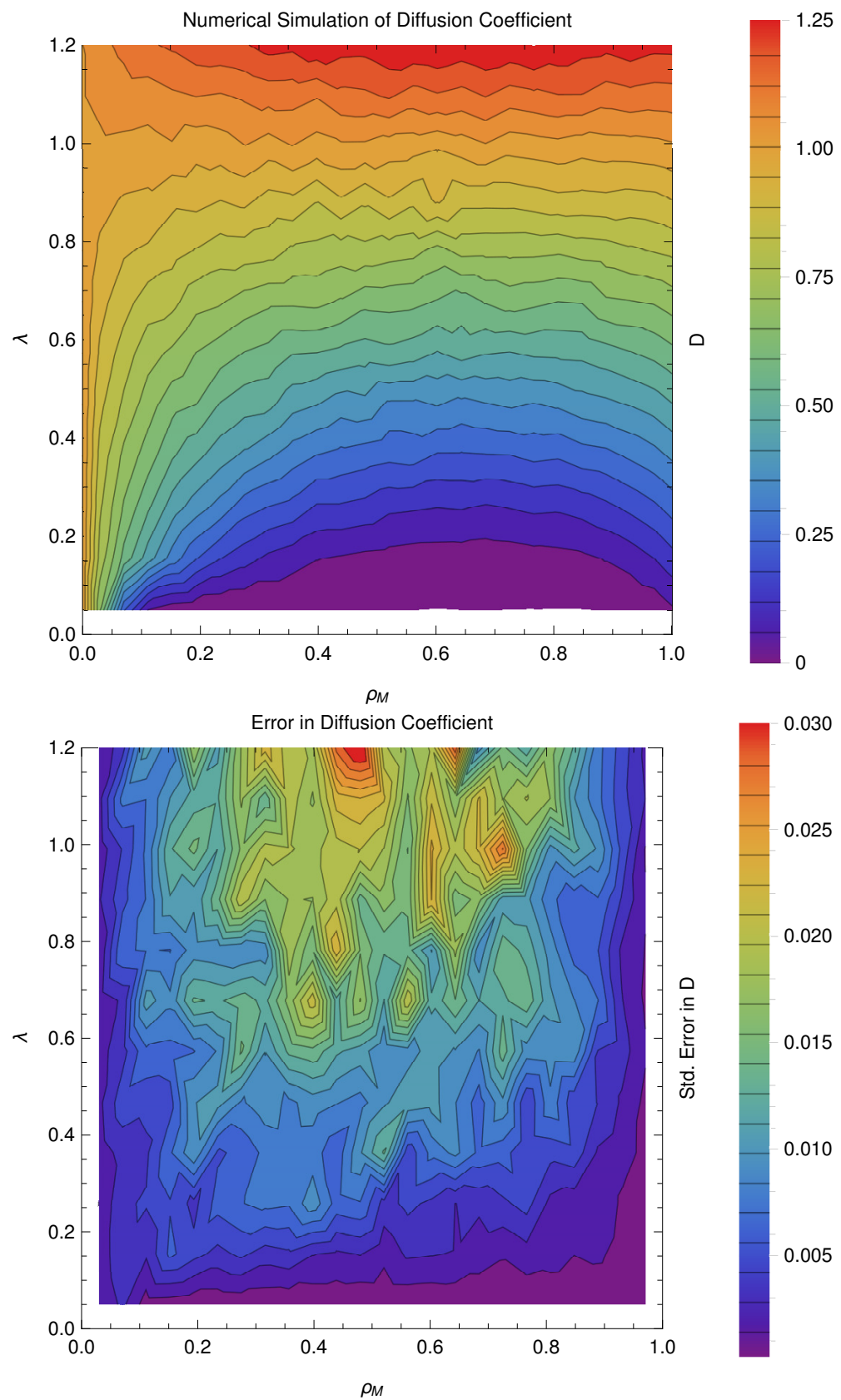
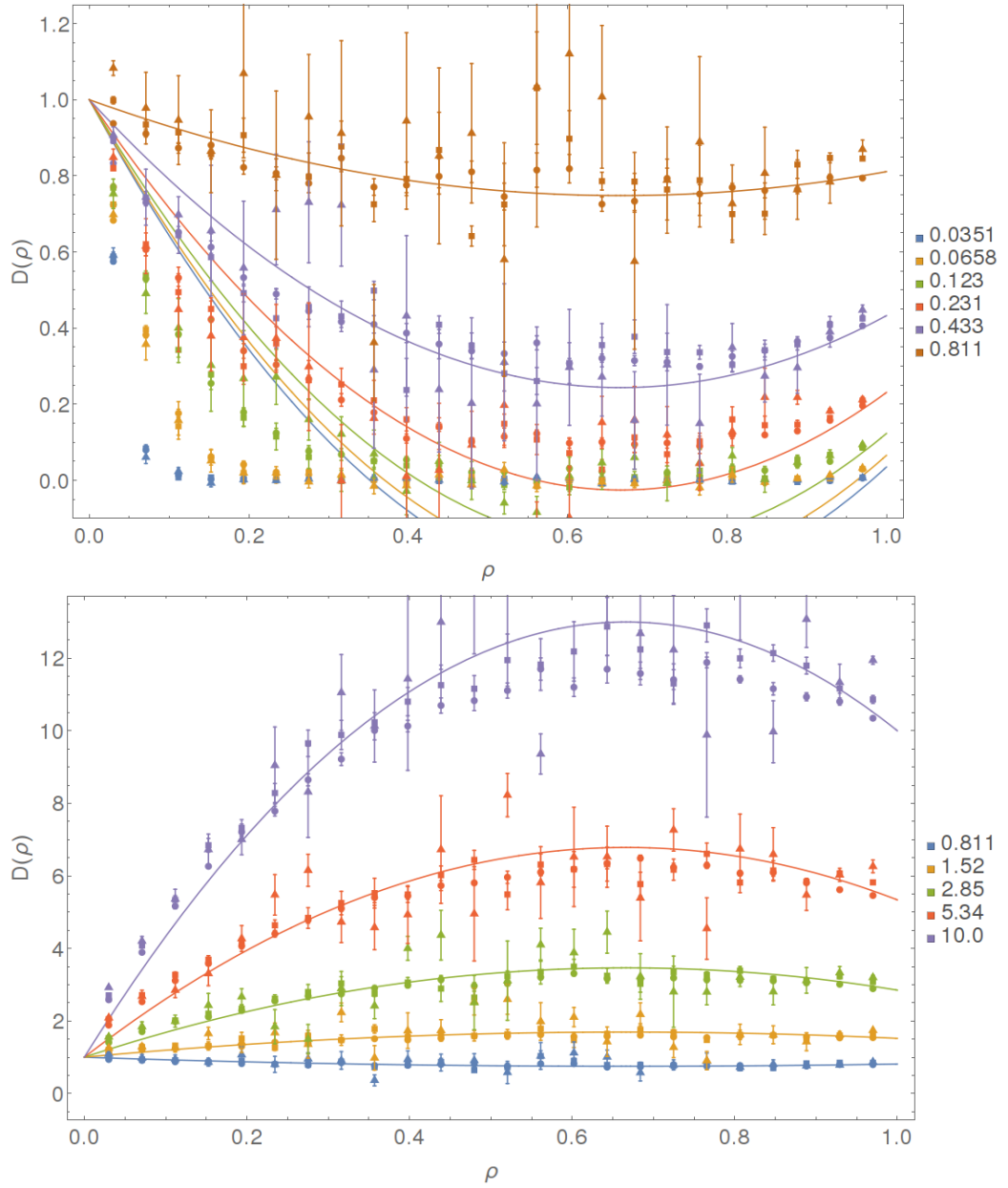


Figure 4.17 Data computed using the same methodology as in Fig. 4.16, but this time we have plotted the diffusion coefficient as a function of density with multiple coloured datasets indicating different values for λ . In addition, these results were made using different system sizes, with **circles**, **squares** and **triangles** corresponding to systems of size $L = 32, 64$ and 128 respectively. The MFT prediction is also displayed for each λ as a solid coloured curve. We have split the data between low and high λ -values for ease of visualisation.



- We probably used a system that was unnecessarily large. A size 64 system proved to be quite adequate later on, and equilibrates much faster.
- We should have performed a larger number of shorter analysis runs; that way we would probably obtain a more robust estimate for D , which wouldn't be so susceptible to being kicked around by individual rogue measurements.
- We only hit upon the idea of scanning in $\log \lambda$ instead of λ later on in the research; thus, the format here does not allow for easy direct comparison with our TRM results which do use $\log \lambda$.

That said, these results do compare nicely with our MFT calculations, displayed in Fig. 2.5. The qualitative features are very similar, although the MFT-predicted “transition” doesn’t occur quite where it suggests, which we have seen more clearly in our scans in Sec. 4.3.2. Also, the diffusion coefficient does not seem to vary in a consistent way with system size.

4.4 2D Calculation Results

As we saw in Sec. 2.4, it is possible to define a logical extension of the SPM to dimensions higher than 1D. Whilst it is not viable to perform TRM calculations in higher dimensions (as the scaling with system size is already very bad), it is relatively easy to adapt our 1D KMC codes to perform SPM calculations in 2D or 3D. Such a KMC input script may be found in `kmc/2d/2dSteadyFlow.py` in [19]. One thing that does need considering in this case is that a 2-dimensional square lattice-based domain would normally have 4 boundaries instead of 2, which would mean 2 extra boundary conditions which would need to be prescribed in addition to ρ_0 and ρ_L . However, we have avoided this difficult by making one of the coordinates cyclic; therefore, in our 2D calculations we are really considering flow down a tube, with circumference W . We still use the same double-layered boundary technique as in 1D, thus for a system of length L we have $W \times (L + 4)$ lattice sites in play.

4.4.1 Aspect Ratio Considerations

Given that we now have two system size variables to play with, a natural question to ask would be how the system’s behaviour changes as we adjust W and L , and

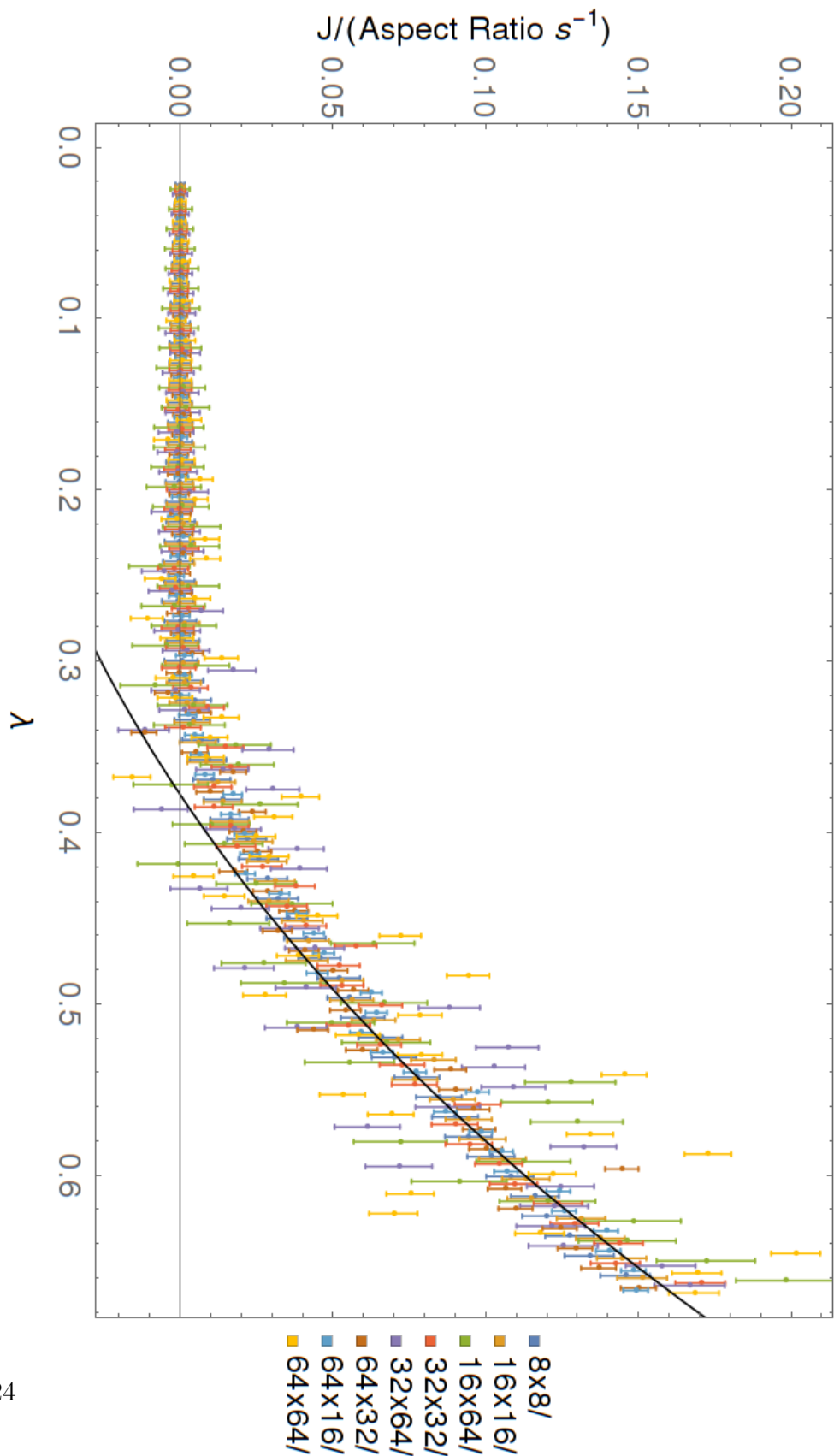
in particular their aspect ratio. We would expect that total current with given boundary conditions would usually scale inversely with L and in proportion to W (as more current can flow across a wider cyclic surface); thus, the total current should scale as $\frac{W}{L}$, the aspect ratio of the system. We can test this, and also check how system convergence scales with system size, by performing calculations of the current with several different (L, W) pairs. We have maintained the boundary conditions to be $(\rho_0, \rho_L) = (0.75, 0.25)$ throughout, and in each case used an initial equilibration run of 1600000 KMC steps followed by 4096 runs consisting of alternating 16000-step and 32000-step analysis and relaxation runs respectively; then, we have varied λ and measured the mean current. The results are displayed in Fig 4.18.

Firstly, note that our supposition about the aspect ratio does appear to be true; the data points for which the aspect ratio is 1 line up quite nicely, and the situations where it is $\frac{1}{2}$ or 2 yield currents which are halved or doubled accordingly. Notice also that the MFT prediction, whilst overestimating the actual λ for which the transition occurs, is actually much better reproduced here than in 1D, as here the currents do indeed decrease to zero much more clearly, in line with the idea that there should be a hard transition. It is also worth noting that the spread of the data, generally indicative of both convergence quality as well as the actual current fluctuation, is very large for the larger system sizes. Thus, we can conclude that it is probably pointless trying to measure with system sizes of 32×32 or higher, as we just cannot achieve the calculational stability required to say anything of consequence. On the other hand, whilst the system of size 8×8 gives nicely grouped data, it is also conceptually probably too small to be useful to us (after all, in 1D we can perform TRM calculations with length 8). Thus, in our next batch of calculations we decided to use systems of size 16×16 .

4.4.2 Varying λ with Constant Boundary Conditions

We intended to perform a systematic battery of calculations in 2D just as we have done in 1D. However, due to the bigger issues with equilibration and overall computational time which occur in 2D we found that performing decent calculations was much more difficult than we anticipated; thus, due to time constraints, we only managed to perform one high-quality calculation. This is a scan through values of λ with fixed boundary conditions, similar to our work in Sec. 4.3.2. Here we used $L \times W = 16 \times 16$, allowed 16000000 KMC steps for

Figure 4.18 The variation of the current in a 2D SPM system with λ , for a variety of different system sizes and aspect ratios. The dotted line indicates the relevant MFT prediction. This was computed using KMC.



equilibration time, and then did 4096 measurement cycles of alternating 16000-step and 320000-step analysis and relaxation runs, just like in Sec.4.4.1. We repeated these calculations with the same parameters with $L \times W = 32 \times 32$. Our results for the overall system density are displayed in Fig.4.19, and our measurements of current and its variance are shown in Fig.4.20.

Let us discuss the density results first, as without those the current results don't make as much sense. The density changes with λ are similar to our 1D results in the sense that the density attempts to converge to 1 for extremely small values of λ regardless of the actual boundary conditions used, and the density has an inflection or minimum in each case for some λ a little below 1.

However, there are some big differences:

- The density does **not** appear to be converging to some common value regardless of boundaries in the large- λ regime like it did in 1D. A possible explanation for this is that there is not a straightforward family of bulk maximal-flow configurations which are inherently more stable than their rivals like there seems to be in 1D; instead, due to the larger space of possible configurations available in 2D, it may be the case that there are many different ways of realising fast rapid flow, which have different densities. An easy way to test this would be to perform similar calculations to these, but with a greater variety of boundary conditions; then, one should be able to observe whether the spectrum of densities in the large- λ (repulsive) limit is continuous or discrete.
- For our low-density choice of boundary conditions $(\rho_0, \rho_L) = (0.3, 0.1)$, it would appear that the mean overall system density splits into two separate branches for the $L \times W = 16 \times 16$ system, forming a curve reminiscent of the hysteresis curves exhibited by ferromagnets [10]. However, this does not seem to happen in the larger $L \times W = 32 \times 32$ system. Thus, we may be probing a scenario in which the small system size allows multiple different stable dynamical modes to form, whilst the larger system does not support this.

So far as the current is concerned, we see broadly the same behaviour as in our (linear) plot in Fig 4.18; the current has roughly power-law dependence on λ for large λ , partially agreeing with the MFT prediction, before dissolving into noise below a threshold in λ . The mean current for our low density boundary

Figure 4.19 The variation of the overall density in a 2D SPM system with λ , with 3 sets of boundary conditions as indicated. Here diamonds indicate results taken with $L \times W = 16 \times 16$, whilst crosses indicate results with $L \times W = 32 \times 32$.

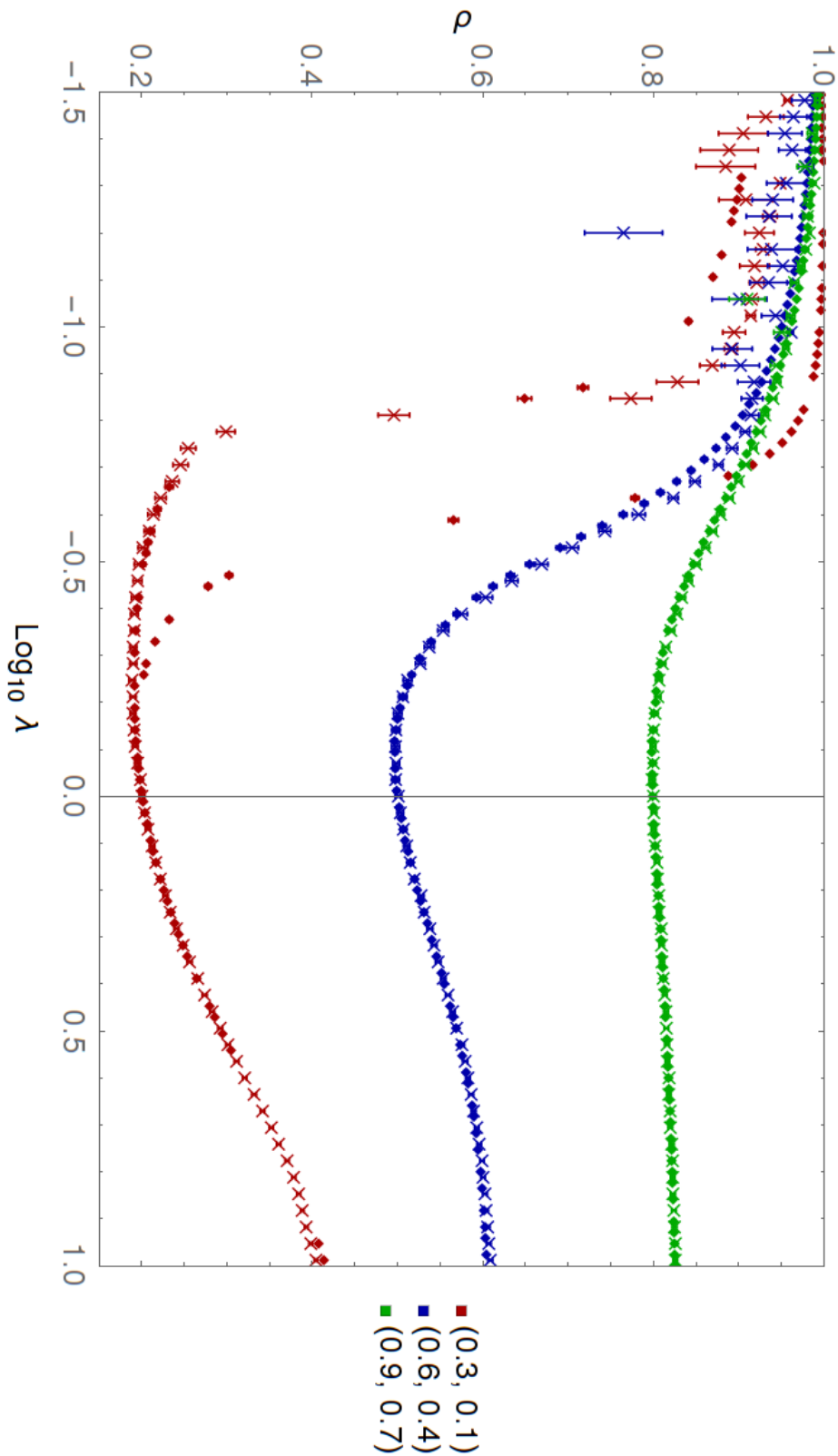
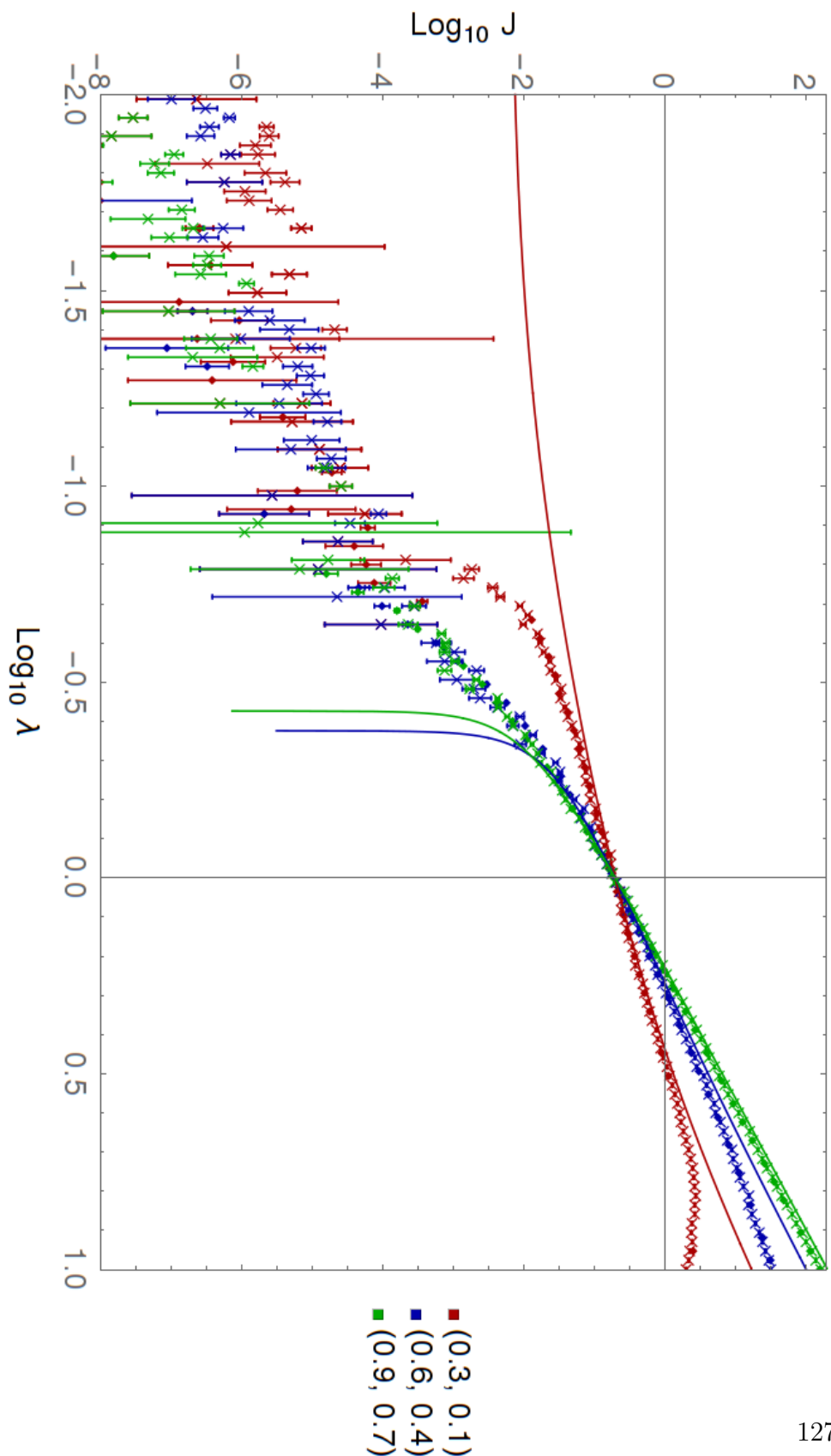


Figure 4.20 The variation of the mean current and its variance in a 2D SPM system with λ , with boundary conditions as indicated. Diamonds indicate results taken with $L \times W = 16 \times 16$, crosses $L \times W = 32 \times 32$.



choice exhibits branching just like the density does, suggesting that the effective diffusion coefficients of the competing configurations are different. The current variance is broadly power-law with λ , with kinks around the transitions and again some exhibition of the “hysteresis”-like branching in the $L \times W = 16 \times 16$ case.

Another way to look at this branching is to consider the fact that researchers have observed “stripes” in the KLS model [63]. In that particular context the model contains asymmetric bulk dynamics, and stripes of low and high density spontaneously form and spiral around the system, transmitting current as they do so. It could be the case that our 16×16 system tries to generate such stripes, but is too small to support more than one stripe; thus, instead different stripes are realised in different simulations. Of course, as this system is ergodic, we should in the long-term limit see both stripe types manifest in any given simulation; however, the switching time, if both stripe types are quite stable, might be so long that we would never actually observe this happening. As we see no such effect in the larger system, this hypothesis seems likely.

4.5 Conclusions

The primary conclusions from our work with Monte-Carlo methods is as follows:

- Our Monte-Carlo work with 1D systems yields results very similar to those we have already observed using our Transition-Rate Matrix method; thus, our fears that the small systems we investigated using TRM were too small to properly portray the properties of larger systems seem to have gone unrealised.
- These results appear to confirm our observation that a *power law switching* phenomenon does indeed occur in 1D. Likewise they support our hypothesis that 1D systems with large λ self-organise to yield similar system configurations regardless of boundary conditions, in an effort to maximise flow (or more directly, system stability).
- Our foray in 2D has been brief, but suggests that there is much more interesting material to study there, in particular the limiting behaviours with extreme λ and the hysteresis-curve effect we see in the density for low-density boundary configurations in small systems.

Chapter 5

Conclusions

During the course of this research, we have used a whole battery of methods in order to try to understand the behaviour of the Sticky Particle Model. Here we present our main conclusions, and suggest topics which future researchers may wish to investigate.

Our main conclusions about the Sticky Particle Model are as follows:

- The Sticky Particle Model, and its n -dimensional generalisation, is the unique stochastic exclusion model defined on a square n -dimensional lattice in which the particle dynamics are completely symmetric, depend only upon a particle's immediate environment and obey detailed balance (Sec. 2.4.1).
- The partition function and chemical potential for the SPM on a closed ring can be calculated analytically (Sec. 2.2.3).
- The n -dimensional SPM has simple continuum-limit mean-field approximation which can be easily calculated (Sec. 2.4.2). It isn't great at predicting behaviour in 1D, but in higher dimensions it is quite good.
- In 1D we can use our numerical Transition Rate Matrix method to exactly solve, to great accuracy, small SPM systems (Ch. 3).
- Using TRM methods, we find that in 1D we observe a *power-law switching* phenomenon, whereby the dependence of the boundary-induced current upon the stickiness parameter λ switches from varying linearly with λ to varying approximately cubically with λ (Sec. 3.3.3). Whilst this does

not appear to be a discontinuous phase transition in the normal sense, the system does undergo rapid change when λ is varied only slightly. We did not find sufficient evidence of the types of behaviour which usually accompany phase transitions (e.g. discontinuous order parameters, diverging fluctuation sizes, etc), we do not believe we can call this change a phase transition; however, it might be reasonable to refer to the continuous change in behaviour from one regime to another as a **crossover**.

- Our TRM observations in 1D are broadly confirmed by larger-scale Monte-Carlo simulations (Sec. 4.3).
- In 2D our Monte-Carlo calculations have revealed an interesting phenomenon whereby there appear to be multiple stable (or possibly metastable) states which can occur in small SPM systems with given boundary conditions at small λ (Sec. 4.4.2); these states may be identified by their different densities and current dependencies.

We have also developed many codes and other technologies in order to carry out our investigations [19, 20]. Of the methods we have developed, we are perhaps most proud of the TRM method, which isn't something we have seen the like of in the literature. We suspect that it could be put to good use on a variety of other low-dimensional systems, to give researchers insight into the behaviour of these systems on small scales. This small-scale behaviour can often be a good window into larger-scale phenomena, and using TRM analysis one might pick up on things to calculate that one wouldn't usually think to investigate.

In terms of future work to be done in this area, we would suggest that other systems might exhibit power-law switching, and so this should be checked. We would also suggest that the community might wish to look again at models which are symmetric and obey detailed balance; although their equilibrium properties in closed boundaries are often rather trivial, this work has shown that they are capable of doing interesting things when driven by boundary conditions. Finally, we think that the odd hysteresis-like phenomenon we saw in 2D is well worth further investigation, and regret not having the time to pursue it further.

Appendix A

Code Locations

A.1 1d Ising Correlation Functions

The Python script `correlationFunctions/exactDist.py` in [19] computes the probability of a site being occupied l lattice spacings away from an occupied site. It requires the system size L and the number of particles N as inputs. The output is saved in a file called `corrFnResults.m`, which is formatted so that it may be used by **Mathematica**.

A.2 n -Dimensional Continuum-Limit MFT

The **Mathematica** script `codes/mathematica/analytic/ndMftCurrent.m` contained in [20] computes the current which flows between two adjacent sites (offset in the e_1 direction) in the MFT of the n -dimensional SPM; due to symmetry, this tells us what happens in an arbitrary direction. In this case n is set to 3, but it still works if changed to any positive number.

Bibliography

- [1] “ α -Fe (ferrite) Crystal Structure: Datasheet from “PAULING FILE Multinaries Edition – 2012” in SpringerMaterials (https://materials.springer.com/isp/crystallographic/docs/sd_1817302).”, https://materials.springer.com/isp/crystallographic/docs/sd_1817302. Copyright 2016 Springer-Verlag Berlin Heidelberg & Material Phases Data System (MPDS), Switzerland & National Institute for Materials Science (NIMS), Japan.
- [2] Allen, M. J., V. C. Tung, and R. B. Kaner. “Honeycomb carbon: a review of graphene.” *Chemical reviews* 110, 1: (2009) 132–145.
- [3] Arrhenius, S. “Über die Dissociationswärme und den Einfluss der Temperatur auf den Dissociationsgrad der Elektrolyte.” *Zeitschrift für physikalische Chemie* 4, 1: (1889) 96–116.
- [4] Atkins, P., and J. De Paula. *Physical chemistry for the life sciences*. Oxford University Press, USA, 2011.
- [5] Baxter, R. J. *Exactly solved models in statistical mechanics*. Elsevier, 2016.
- [6] Biswas, B., S. Chatterjee, S. Mukherjee, and S. Pal. “A discussion on Euler method: A review.” *Electronic Journal Of Mathematical Analysis And Applications* 1, 2: (2013) 294–317.
- [7] Blythe, R. A., and M. R. Evans. “Nonequilibrium steady states of matrix-product form: a solver’s guide.” *Journal of Physics A: Mathematical and Theoretical* 40, 46: (2007) R333.
- [8] Bortz, A., M. Kalos, and J. Lebowitz. “A new algorithm for Monte Carlo simulation of Ising spin systems.” *Journal of Computational Physics* 17, 1: (1975) 10 – 18. <http://www.sciencedirect.com/science/article/pii/0021999175900601>.
- [9] Brush, S. G. “History of the Lenz-Ising model.” *Reviews of modern physics* 39, 4: (1967) 883.
- [10] Chikazumi, S., and C. Graham. *Physics of Ferromagnetism (International Series of Monographs on Physics; 94)*. Oxford University Press, 1997.

- [11] Crampe, N., E. Ragoucy, and M. Vanicat. “Integrable approach to simple exclusion processes with boundaries. Review and progress.” *Journal of Statistical Mechanics: Theory and Experiment* 2014, 11: (2014) P11,032. [https://doi.org/10.1088%2F1742-5468%2F2014%2F11%2Fp11032](https://doi.org/10.1088/2F1742-5468%2F2014%2F11%2Fp11032).
- [12] Deal, B. E., and A. S. Grove. “General Relationship for the Thermal Oxidation of Silicon.” *Journal of Applied Physics* 36, 12: (1965) 3770–3778. <https://doi.org/10.1063/1.1713945>.
- [13] Dewar, R. C. “Maximum entropy production and the fluctuation theorem.” *Journal of Physics A: Mathematical and General* 38, 21: (2005) L371.
- [14] Gardiner, C. W., et al. *Handbook of stochastic methods*, volume 3. Springer Berlin, 1985.
- [15] Garrido, P. L., J. L. Lebowitz, C. Maes, and H. Spohn. “Long-range correlations for conservative dynamics.” *Phys. Rev. A* 42: (1990) 1954–1968. <https://link.aps.org/doi/10.1103/PhysRevA.42.1954>.
- [16] Golinelli, O., and K. Mallick. “The asymmetric simple exclusion process: an integrable model for non-equilibrium statistical mechanics.” *Journal of Physics A: Mathematical and General* 39, 41: (2006) 12,679.
- [17] Grafke, T., R. Grauer, and T. Schäfer. “The instanton method and its numerical implementation in fluid mechanics.” *Journal of Physics A: Mathematical and Theoretical* 48, 33: (2015) 333,001.
- [18] Grynberg, M. D. “Revisiting Kawasaki dynamics in one dimension.” *Phys. Rev. E* 82: (2010) 051,121. <https://link.aps.org/doi/10.1103/PhysRevE.82.051121>.
- [19] Hellier, J. “Interacting Particles in 1D and 2D: Annotated codes.” <https://doi.org/10.7488/ds/2500>.
- [20] ———. “Interacting Particles in 1D and 2D: Primary code base.” <https://zenodo.org/badge/latestdoi/52518520>.
- [21] Hellier, J. D., and G. J. Ackland. “On the Diffusion of Sticky Particles in 1D.” *arXiv preprint arXiv:1803.09712*.
- [22] Hoffmann, M. J., S. Matera, and K. Reuter. “kmos: A lattice kinetic Monte Carlo framework.” *Computer Physics Communications* 185, 7: (2014) 2138–2150.
- [23] Honig, J. M. “Mean field theory of phase transitions.” *Journal of chemical education* 76, 6: (1999) 848.
- [24] Ising, E. “Beitrag zur Theorie des Ferromagnetismus.” *Zeitschrift für Physik* 31, 1: (1925) 253–258. <https://doi.org/10.1007/BF02980577>.

- [25] Ivanova, N. M. “Exact solutions of diffusion-convection equations.” *arXiv preprint arXiv:0710.4000* <https://arxiv.org/abs/0710.4000>.
- [26] Katz, S., J. L. Lebowitz, and H. Spohn. “Nonequilibrium steady states of stochastic lattice gas models of fast ionic conductors.” *Journal of Statistical Physics* 34, 3: (1984) 497–537. <http://dx.doi.org/10.1007/BF01018556>.
- [27] Kawasaki, K. “Diffusion Constants near the Critical Point for Time-Dependent Ising Models. I.” *Phys. Rev.* 145: (1966) 224–230. <https://link.aps.org/doi/10.1103/PhysRev.145.224>.
- [28] Keffer, D. “The working mans guide to obtaining self diffusion coefficients from molecular dynamics simulations.” .
- [29] Kolesnichenko, A., V. Senni, A. Pourranjabar, and A. Remke. *Applying Mean-Field Approximation to Continuous Time Markov Chains*, Berlin, Heidelberg: Springer Berlin Heidelberg, 2014, 242–280. https://doi.org/10.1007/978-3-662-45489-3_7.
- [30] Laisant, C.-A. “Intégration des fonctions inverses.” *Nouvelles annales de mathématiques : journal des candidats aux écoles polytechnique et normale* 5: (1905) 253–257. <http://eudml.org/doc/101975>.
- [31] Landau, L. D., E. M. Lifshitz, and L. Pitaevskii. *Statistical physics, part I*. pergammon, Oxford, 1980.
- [32] Leetmaa, M., and N. V. Skorodumova. “KMCLib: A general framework for lattice kinetic Monte Carlo (KMC) simulations.” *Computer Physics Communications* 185: (2014) 2340–2349.
- [33] Lehoucq, R., and D. Sorensen. “Deflation Techniques for an Implicitly Restarted Arnoldi Iteration.” *SIAM Journal on Matrix Analysis and Applications* 17, 4: (1996) 789–821. <https://doi.org/10.1137/S0895479895281484>.
- [34] Lehoucq, R. B. “On the convergence of an implicitly restarted Arnoldi method.” Technical report, Sandia National Labs., Albuquerque, NM (US); Sandia National Labs , 1999.
- [35] Lehoucq, R. B., D. C. Sorensen, and C. Yang. *ARPACK users’ guide: solution of large-scale eigenvalue problems with implicitly restarted Arnoldi methods*, volume 6. Siam, 1998.
- [36] Lenz, W. “Beitrag zum Verständnis der magnetischen Erscheinungen in festen Körpern.” *Z. Phys.* 21: (1920) 613–615.
- [37] Levine, R. “Molecular Reaction Dynamics, Cambridge University Press.”, 2005.

- [38] Li, B., Z. Chen, W. He, T. Zhou, Y. Wang, L. Peng, J. Li, and Q. Liu. “Effect of titanium grain orientation on the growth of compounds at diffusion bonded titanium/steel interfaces.” *Materials Characterization* 148.
- [39] Liggett, T. M. *Interacting particle systems*. Springer-Verlag, Berlin, 1985.
- [40] Martynov, G. A. *Classical Statistical Mechanics*, volume 89. Springer Science & Business Media, 2012.
- [41] Martyushev, L. M., and V. D. Seleznev. “Maximum entropy production principle in physics, chemistry and biology.” *Physics reports* 426, 1: (2006) 1–45.
- [42] Miller, T. A., B. Lamb, K. Prater, J. K. Lee, and R. N. Adams. “Tracer Diffusion Coefficients of Aromatic Organic Molecules.” *Analytical Chemistry* 36, 2: (1964) 418–420. <https://doi.org/10.1021/ac60208a003>.
- [43] Panju, M. “Iterative methods for computing eigenvalues and eigenvectors.” *arXiv preprint arXiv:1105.1185* .
- [44] Patterson, R. A. “Crystal Structure of Titanium and Chromium.” *Phys. Rev.* 26: (1925) 56–59. <https://link.aps.org/doi/10.1103/PhysRev.26.56>.
- [45] Plimpton, S., C. Battaile, M. Chandross, L. Holm, A. Thompson, V. Tikare, G. Wagner, E. Webb, X. Zhou, C. G. Cardona, et al. “Crossing the mesoscale no-mans land via parallel kinetic Monte Carlo.” *Sandia Report SAND2009-6226* .
- [46] Prados, A., J. J. Brey, and B. Sánchez-Rey. “A dynamical monte carlo algorithm for master equations with time-dependent transition rates.” *Journal of Statistical Physics* 89, 3: (1997) 709–734. <https://doi.org/10.1007/BF02765541>.
- [47] Pukdeboon, C. “A review of fundamentals of Lyapunov theory.” *The Journal of Applied Science* 10, 2: (2011) 55–61.
- [48] Reif, F. *Fundamentals of statistical and thermal physics*. Waveland Press, 2009.
- [49] Robert, C. P. *The Metropolis-Hastings Algorithm*, American Cancer Society, 2015, 1–15.
- [50] Rota, G.-C. “Integrable systems in statistical mechanics.” *Advances in Mathematics* 73: (1989) 147.
- [51] Sherratt, J. A. “On the transition from initial data to travelling waves in the Fisher-KPP equation.” *Dynamics and Stability of Systems* 13, 2: (1998) 167–174. <https://doi.org/10.1080/02681119808806258>.
- [52] Stoll, M. *Solving linear systems using the adjoint*. Ph.D. thesis, Oxford University, 2008.

- [53] Strecka, J., and M. Jascur. “A brief account of the Ising and Ising-like models: Mean-field, effective-field and exact results.” *arXiv preprint arXiv:1511.03031* .
- [54] Tegner, B., L. Zhu, C. Siemers, K. Saksł, and G. Ackland. “High temperature oxidation resistance in titanium-niobium alloys.” *Journal of alloys and compounds* 643: (2015) 100–105.
- [55] van Tongeren, S. J. “Introduction to the thermodynamic Bethe ansatz.” *Journal of Physics A: Mathematical and Theoretical* 49, 32: (2016) 323,005.
- [56] Touchette, H. “A basic introduction to large deviations: Theory, applications, simulations.” *arXiv preprint arXiv:1106.4146* .
- [57] Van Vleck, J. H. “A Survey of the Theory of Ferromagnetism.” *Reviews of Modern Physics* 17, 1: (1945) 27.
- [58] Voorhees, P. W. “The theory of Ostwald ripening.” *Journal of Statistical Physics* 38, 1-2: (1985) 231–252.
- [59] Voter, A. *Radiation Effects in Solids edited by KE Sickafus and EA Kotomin*. Springer, NATO Publishing Unit, 2005.
- [60] Wallace, D. “Some applications of instantons in statistical mechanics.” In *Solitons and Condensed Matter Physics*, Springer, 1978, 104–115.
- [61] Wersin, P., L. V. Loon, J. Soler, A. Yllera, J. Eikenberg, T. Gimmi, P. Hernn, and J.-Y. Boisson. “Long-term diffusion experiment at Mont Terri: first results from field and laboratory data.” *Applied Clay Science* 26, 1: (2004) 123 – 135. <http://www.sciencedirect.com/science/article/pii/S0169131703002679>. Clays in Natural and Engineered Barriers for Radioactive Waste Confinement.
- [62] Zhang, Y., and R. W. Pastor. “A Comparision of Methods for Computing Transition Rates from Molecular Dynamics Simulation.” *Molecular Simulation* 13, 1: (1994) 25–38. <https://doi.org/10.1080/08927029408022182>.
- [63] Zia, R. K. P. “Twenty Five Years After KLS: ACelebration ofNon-equilibrium Statistical Mechanics.” *Journal of Statistical Physics* 138, 1: (2010) 20–28. <http://dx.doi.org/10.1007/s10955-009-9884-0>.
- [64] Zingg, D. W., and T. T. Chisholm. “Runge–Kutta methods for linear ordinary differential equations.” *Applied Numerical Mathematics* 31, 2: (1999) 227–238.